Étude de la Cristallisation du Polyéthylène

par

Azar Shamloo

Thèse présentée au Département de chimie en vue
de l'obtention du grade de Philosophia doctor (Ph.D.)

FACULTÉ DES SCIENCES, UNIVERSITÉ DE SHERBROOKE

Sherbrooke, Québec, Canada, Juin 2018

Study of Polyethylene Crystallization

By

Azar Shamloo

Thesis presented in the chemistry department for obtaining the degree of
Doctor of Science (Ph.D.)

FACULTY OF SCIENCES
UNIVERSITÉ DE SHERBROOKE

Sherbrooke, Québec, Canada, June 2018

Le 13 Juin 2018
Le jury a accepté la Thèse de Madame Azar Shamloo dans sa version finale.

Jury Members

Professor Armand Soldera
Research Director
Department of Chemistry

Professor Denis Rodrigue
Research Codirector
Department of Chemical Engineering
Université Laval

Professor Veena Choudhary
External evaluator
Centre For Polymer Science and Engineering
Indian Institute of Technology, Delhi

Professor Patrick Ayotte
Internal evaluator
Department of Chemistry

Professor Mathieu Robert
Internal evaluator
Department of Civil Engineering

Professor Jean-Philippe Bellenger
Committee President
Department of Chemistry

RÉSUMÉ

Dans l'industrie, les produits finis en plastique sont fabriqués par diverses techniques de traitement telles que le moulage par compression, le moulage par injection, le moulage par soufflage, l'extrusion, etc. Ces opérations impliquent l'exposition de résines polymères à de nombreux conditions telles que la température, pression, contrainte, etc. Certaines conditions sont connues pour affecter la nature de la structure cristalline des polymères semi-cristallins qui est contrôlée par des mécanismes de cristallisation. Pour un matériau tel que le polyéthylène (PE), la structure de la chaîne polymère influence la morphologie et la cristallinité. Les nanocristaux de PE ont attiré une attention considérable en raison des applications potentielles dans la technologie et de leurs propriétés fascinantes qui sont différent clairement des leurs matériaux en vrac correspondants. Il existe plusieurs méthodes pour déterminer la cristallinité du polymère, mais la plupart d'entre elles sont destructrices et fournissent des informations ponctuelles. Elles nécessitent également souvent un temps de manipulation important, tandis que les expériences sur des objets à l'échelle nanométrique sont souvent restées avec une grande incertitude en raison de la difficulté de produire et de manipuler ces objets à des échelles de longueur inférieures à 10 nm. Pour ces raisons, les méthodes de calcul sont considérées comme des outils parfaits pour mieux comprendre ces observations expérimentales.

La finalité de cette étude vise à révéler l'effet des conditions environnementales sur la température de fusion des nanocristaux de chaînes alcanes en utilisant tant des simulations de dynamique moléculaire afin de représenter au mieux des composés réels ainsi que des techniques expérimentales pour étudier les conditions de traitement sur leur tension interfaciale. Il a été montré que la loi de Gibbs-Thomson peut être reproduite, car cette loi dévoile une relation linéaire entre la température de fusion et l'inverse de l'épaisseur du cristal. Pour révéler efficacement l'impact des conditions environnementales sur le comportement de fusion PE, un nanocristal composé de chaînes d'alcane est incorporé dans une phase amorphe. Finalement, l'étude du comportement de fusion et de cristallisation des polymères sous haute pression a un intérêt fondamental pour la compréhension de la structure du polymère. Suite à notre travail sur le

nanocristal chaînes d'alcane, nous avons calculé la valeur de la tension interfaciale à différentes pressions pour explorer l'effet de ce paramètre sur la température de fusion et la tension interfaciale de ce matériau. Plus précisément:

a) Nous avons démontré que la température de fusion augmente et la tension interfaciale diminue, en comparant les résultats obtenus avec des chaînes d'alcanes nanocristal incorporées dans une phase amorphe avec un nanocristal isolé. Cela peut se révéler grâce au comportement du déplacement quadratique moyenne d'une particule près de la surface du cristal dans les deux systèmes (chaînes d'alcanes nanocristal incorporées dans une phase amorphe avec un nanocristal isolé). Les interactions entre les monomères non liés dans nanocristal chaînes d'alcane et alcanes dans la phase amorphe diminuent la mobilité des chaînes dans le cristal conduisant à une température de fusion plus élevée et une tension interfaciale plus faible.

b) Il a été montré que l'augmentation de la pression entraîne une diminution de la tension interfaciale, ce qui peut s'expliquer par une diminution de l'énergie libre de Gibbs. De plus, en comparant les expériences et les données de simulation, nous obtenons une correspondance précise qu'en augmentant la pression, le point de fusion des échantillons augmentera aussi.

Dans la partie expérimentale, l'effet de la température du moule, de la pression du moule, du taux de refroidissement et du profil de température sur les propriétés thermiques et mécaniques des échantillons sont étudiés. Les résultats confirment que pour des échantillons symétriques (température de moulage uniforme), une température de fusion, les modules de flexion et de traction plus élevées découlent d'une augmentation de la pression et la température de moulage, tout en diminuant la vitesse de refroidissement.

D'autre part, pour les échantillons asymétriques où le gradient de température est appliqué lors du moulage, le module de traction et de flexion ne dépend pas seulement de la différence de température, mais aussi de la température moyenne entre les plaques supérieure et inférieure de la presse à mouler par compression. On observe que les modules de traction et flexion les plus élevés

sont obtenus pour la température la plus basse sur les deux plaques. Ce comportement peut être clairement révélé en utilisant le rapport de module de flexion qui représente la valeur mesurée lorsque la charge est appliquée sur les côtés supérieure et inférieure (E_b / E_u). Enfin, il a été montré que l'augmentation de la pression de moulage entraîne une tension interfaciale la plus basse qui peut s'expliquer par une diminution de l'énergie libre de Gibbs pendant la cristallisation. Ce résultat a également confirmé les données de simulation.

SUMMARY

In industry, end user plastics products are made by diverse polymer processing techniques such as compression molding, injection molding, blow molding, extrusion, etc. These processing operations involve exposing polymer resins to elevated temperatures, pressures, stresses, strains, etc. All these conditions are known to affect the nature of the crystalline structure of semi-crystalline polymers and is referred to as morphology which is controlled by crystallization mechanisms. For a material such as polyethylene (PE), the polymer chain structure influences on morphology and crystallinity. PE nanocrystals have attracted considerable attention due to potential applications in technology and their fascinating properties which clearly differ from those of their corresponding bulk materials. Nowadays, different methods are used to determine polymer crystallinity, but most of them are destructive and provide single point information. They also often require significant handling time, while experiments on nanoscale objects are often plague with high uncertainty because of the difficulty of producing and manipulating these objects at length scales below 10 nm. For these reasons, computational methods are seen as perfect tools to get more insight into these experimental observations.

This work is thus aimed at revealing the effect of environmental conditions on the melting temperature of alkane chains nanocrystals using molecular dynamics simulations to approach real compounds. It was shown that the Gibbs-Thomson law can be reproduced, as this law unveils a linear relationship between the melting temperature and the inverse of the crystal thickness. To efficiently reveal the impact of environmental conditions on the melting behaviour of PE, a nanocrystal composed of alkane chains is embedded in an amorphous phase. Ultimately, the investigation of the melting and crystallization behaviour of polymers under high pressure has basic interest for the understanding of the polymer structure. Following our work on polyethylene nanocrystal, we calculated the value of interfacial tension at different pressures to explore the effect of this parameter on melting temperature and interfacial tension of this material. More specifically:

a) We demonstrated that melting temperature increases and interfacial tension decreases, comparing the results from single alkane chains nanocrystal embedded in an amorphous phase with isolated crystal. This can be explained by MSD (Molecular Dynamic Simulation) behaviour of one particle near the crystal surface in both systems (single alkane chains nanocrystal embedded in an amorphous phase with isolated crystal). Interactions between unbonded monomers in crystal and alkane chains in the amorphous phase decrease the chains mobility in the crystal leading to higher melting temperature and lower interfacial tension.
b) It was shown that increase of pressure results in decrease of interfacial tension, which can be explained by depression in Gibbs free energy. Furthermore, comparing experiments and simulation data give us an accurate match that by increasing pressure, melting point of samples will increase too.

In experimental part, the effect of mold temperature, mold pressure, cooling rate and temperature profile on the thermal and mechanical properties of the samples are investigated. Results confirm that for symmetric samples (uniform molding temperature), higher melting temperature, flexural and tensile modulus stem from an increase in the molding pressure and molding temperature, while decreasing the cooling rate.

On the other hand, for asymmetric samples where temperature gradient is applied while molding, the tensile and flexural modulus not only depend on the temperature difference, but also on the average temperature between the upper (T_u) and bottom (T_b) plates of the compression molding press. It is observed that the highest tensile and flexural moduli are obtained for the lowest temperature on both plates. This behavior can be clearly revealed using the flexural modulus ratio which represents the value measured when the load is applied on the bottom or the upper sides (E_b/E_u). Finally, it was shown that increasing the molding pressure results in lower interfacial tension which can be explained by a depression of the Gibbs free energy during crystallization. This result confirmed simulation data as well.

ACKNOWLEDGMENTS

This thesis has been a great experience that would not have been possible without the support of many great individuals. My thanks and appreciation to all of them for all their effort, motivation and support during this study.

First and foremost, I would like to express my sincere gratitude to my advisor Prof. Armand Soldera for the continuous support of my Ph.D. study and related research, for his patience, motivation, and immense knowledge. His guidance helped me in all the time of research and writing of this thesis. I am glad to have had this opportunity to work in his lab, the Laboratory of Physical Chemistry of Matter (LPCM).

My sincere thanks also go to my codirector Prof. Denis Rodrigue who provided me an opportunity to join their team at Université Laval, and who gave access to the laboratory and research facilities. Without his precious support it would not be possible to conduct this research. In addition to his scientific support, his guidance and advice has helped me during the entire duration of research and writing for this thesis.

A very special gratitude goes out to Prof. Said Elkoun who allowed me to work and use research facilities in his laboratory in engineering department. His advice and support while writing the article was very precious for me.

Besides my advisors, I would like to thank the rest of my thesis committee: Prof. Veena Choudhary (external evaluator), Prof. Patrick Ayotte (head of the department of chemistry), Prof. Mathieu Robert and Prof. Jean-Philippe Bellenger (the chairman of the committee), agreeing to be my referees. I would also like to thank the rest of the faculty and staff in the Department of Chemistry at the Université de Sherbrooke. In particular, I would like to thank Dr. Jean-Marc Chapuzet, academic coordinator at the Department of Chemistry for his good humor and help.

I would especially like to thank my amazing family for the love, support, and constant encouragement I have gotten over the years. Especially my mother who have supported me along the way. I am grateful to my husband, Vahid, who have provided me through emotional support in my life.
I want to express my deep appreciation for the help and support of my colleagues: Dr. François Porzio, Dr. Nasim Anousheh, François Godey, Vincent St-Onge, Clément Wespiser, Alexandre Fleury and Étienne Cuierrier.

This work was supported by the Centre Québécois sur les Matériaux Fonctionnels (CQMF) and the Fonds Québécois de la Recherche sur la Nature et les Technologies (FQRNT), and Université de Sherbrooke.

This dissertation is dedicated to my father who always inspired me. He dedicated his life to help the others. He is my hero as long as I live.

ABBREVIATIONS

ABS	Acrylonitrile Butadiene Styrene
AMBER	Assisted Model Building with Energy Refinement
B-PE	Branched Polyethylene
CHARMM	Chemistry at HARvard Macromolecular Mechanics
CG	Coarse-Grained
CNC	Computer Numerical Control
CW	Constant Wavelength
DSC	Differential Scanning calorimetry
EVA	Ethylene-Vinyl Acetate Copolymer
G-T	Gibbs -Thomson Equation
HDPE	High Density Polyethylene
IBC	Isolated Boundary Condition
LBFGS	Limited-memory Broyden-Fletcher-Goldfarb-Shanno quasi-Newtonian minimizer
LLDPE	Linear Low-Density Polyethylene
LDPE	Low Density Polyethylene
MC	Monte Carlo Simulation
MD	Molecular Dynamics Simulation
MSD	Mean Square Deviation

OPLS	Optimized Potentials for Liquid Simulations
PBC	Periodic Boundary Condition
PC	Polycarbonate
PE	Polyethylene
POM	Polarized Optical Microscopy
PVA	Poly (Vinyl Alcohol)
QSPR	Quantitative Structure Property Relationships
RIS	Rotational Isomeric States
SAXS	Small Angle X-ray Scattering
T_m	Melting Temperature
T_g	Glass Transition Temperature
UA	United-Atom
VLDPE	Very Low-Density Polyethylene
XRD	X-ray Diffraction
WAXD	Wide Angle X- Ray Scattering

Table of Contents

RÉSUMÉ ii
SUMMARY v
ACKNOWLEDGMENTS vii
ABBREVIATIONS ix
Table of Contents xi
LIST OF FIGURES xv
LIST OF TABLES xvii
CHAPTER I. Literature Review and Objectives of Project 7
1.1. Introduction to Polyethylene 7
1.1.1 High Density Polyethylene 7
1.1.2. Low Density Polyethylene 7
1.1.3. Linear Low-Density Polyethylene 7
1.1.4. Very Low-Density Polyethylene 7
1.1.5. Spherulite Structure 8
1.1.6. Crystalline Structure 8
1.1.7. Intrinsic Properties 9
1.1.8. High Density Polyethylene Synthesis 10
1.1.9. Low Density Polyethylene Synthesis 10
1.2. Models for Semi-Crystalline Polymers 10
1.2.1. Fringed-Micelle Model 10
1.2.2. Chain-Folding Model 11
1.3. Flory's Crystallization Theory for Homopolymers 12
1.4. Lamellar Thickness in Polymers 15
1.5. Gibbs-Thomson Equation 15
1.6. Thermodynamics of Fusion 18
1.7. Objectives of Project 21
CHAPTER II. Review of Polymer Simulation Methods and Molecular Dynamics 23
2.1. Introduction 23

2.2. Simulation of Polymers 23
2.2.1. Polymers Properties 24
2.3. The Objective of Molecular Dynamics 26
2.4. Time Dependence 28
2.5. Non-bonded Interaction 28
2.6. Bonding Potentials 29
2.7. Validation of Force Fields 31
2.8. The MD Algorithm 32
2.9. The Velocity Verlet Algorithm 32
2.10. Molecular Dynamics Methods 33
2.11. Boundary Conditions 35
2.11.1. Periodic Boundary Condition 35
2.11.2. Isolated Boundary Condition (IBC) 37
2.12. Ewald Summation 37
2.13. Neighbor Lists 37
2.14. Molecular Dynamics in Different Ensembles 38
2.15. Energy Minimization 40
2.15.1. Steepest Descent 41
2.15.2. Conjugate Gradient 42
2.15.3. L-BFGS 42
2.16. Cell Construction 42
2.17. Making the Configuration (PE Nanocrystal embedded in Amorphous Phase) 44
2.18. Hydrostatic Uniform Compression 47
2.19. Melting Simulation 47
2.20. Errors and Uncertainty in MD Simulation 47
CHAPTER III. Review of Molding Methods and Effect of Processing Conditions on the Thermal and Mechanical Properties of Polymers 50
3.1. Introduction 50
3.2. Types of Plastics 50
3.3. Molds 51

3.3.1 Injection Molding 51
3.3.2 Compression Molding 52
3.4. Mechanical Properties of Polymers 53
3.4.1. Elasticity 53
3.4.2. Strength 53
3.4.3. Elongation to Break (Ultimate Elongation) 54
3.4.4. Young's Modulus (Modulus of Elasticity or Tensile Modulus) 54
3.4.5. Toughness 54
3.5. Melting Point and Glass Transition Temperature of Polymers 56
3.6. Polymer Crystallinity: Crystalline and Amorphous Polymers 57
3.7. Surface Tension of Polymers 58
3.8. Experimental Work 58
3.9. The Effect of Hydrostatic Pressure on Mechanical Properties of Polymers 61
3.10. Melting of Polymers under high Pressure 62
3.11. Cooling Rate via Crystallinity and Melting Temperature 63
3.12. Molding Temperature via Mechanical Properties, Crystallinity and Melting Point 63
CHAPTER IV. Influence of Compression Molding Conditions on the Thermal and Mechanical Properties of LDPE (Low Density Polyethylene) 65
4.1. Introduction 65
4.2. Influence of Mold Temperature, Pressure and Cooling rate on the Thermal Properties of Symmetric and Asymmetric LDPE Samples 65
4.3. Mechanical Properties of Symmetric and Asymmetric LDPE Samples 71
4.4. Conclusion 76
Chapter V: Melting of Alkane Nanocrystals: Towards a Representation of Polyethylene 78
5.1. Introduction 78
5.2. Molecular Dynamic Simulation of Alkane Chains Nanocrystal embedded in an Amorphous phase: Melting Temperature and Surface Tension via the Gibbs-Thomson Equation 79
5.3. Pressure Effect on the Melting Behavior of Alkane Chains Nanocrystals: Molecular Dynamic Simulation 87
5.4. Conclusion 89

Conclusion 91
APPENDIX I 94
Bibliography 98

LIST OF FIGURES

Figure 1. The general structure of high density, low density and linear low density polyethylene 8
Figure 2. Schematic representation of: a) spherulite structure [53] and b) crystalline structure [52] 9
Figure 3. Schematic of: a) fringed-micelle model for semi-crystalline polymers, b) chain-folded lamellar structure with adjacent re-entry and c) switchboard random [59] 12
Figure 4. Diagram of a crystalline polymer lamella. 16
Figure 5. Variation of T_m as a function of length expressed as $1/\bar{x}$ 17
Figure 6. Variation of temperatures with respect to the inverse of crystal thickness for the crystallization (blue) and melting line (red) 19
Figure 7. General behavior of thermodynamic variables at the equilibrium melting temperature T_m^0: (a) Gibbs free energy and (b) entropy, enthalpy and volume 20
Figure 8. Simulations act as a bridge between different scales: (a) microscopic and (b) macroscopic 27
Figure 9. Geometry of a simple chain molecule illustrating the definition of interatomic distance r_{23}, bend angle θ_{234}, and torsion angle ϕ_{1234} [83] 30
Figure 10. Schematic representation of a periodic boundary [115] 36
Figure 11. Five types of periodic boundary boxes: (a) the triclinic box, (b) the hexagonal prism, (c) the rhombic dodecahedron, (d) the elongated rhombic dodecahedron, and (e) the truncated octahedron [115]. 36
Figure 12. The method of Ewald summation for periodic potentials including the real, reciprocal and original spaces 38
Figure 13. The potential cutoff range (solid circle) and the list range (dashed circle), are indicated (a). The list must be reconstructed before the particles originally outside the list range (red) have penetrated the potential cutoff sphere [89] 39
Figure 14. Random-walk of a polymer chain. 43
Figure 15. Simple example of a scanning procedure. A filled circle presents the last segment added, empty circles are occupied space, and a square represents the free space. 44
Figure 16. Representation of a polyethylene nanocrystal embedded in alkane chains (amorphous phase) 46
Figure 17. Determination of the melting temperature by MD for the crystal 4a4b4c embedded in an amorphous phase (duration 500 ps). (a) Potential energies, (b) heat capacity at constant volume with respect to temperature, and (c) trans-rotameric state 49
Figure 18. Schematic representation of: a) thermoplastic structure and b) thermoset structure 50
Figure 19. Representation of the elongation at break and ductility 54
The toughness represents the energy absorbed by the material before it breaks. A typical stress-strain curve is shown Figure 21. 54

Figure 20. Typical stress-strain curve to calculate the mechanical properties 55
Figure 21. Stress-strain behavior of different materials: a) brittle polymer (glassy polymer/low temperature thermoset), b) ductile polymer (semi-crystalline polymer/plastic/elevated temperature thermoplastic), and c) highly elastic (elastomer)..... 55
Figure 22. Melting point and glass transition of polymers 57
Figure 23. A p-value related to the probability of an observed result 66
Figure 24. Melting point, heat of fusion and degree of crystallinity of the samples produced at 3 MPa and 135, 150 and 165 ºC 67
Figure 25. Melting point heat of fusion and degree of crystallinity for the samples produced at 150 °C and 11, 17, 22 and 28 MPa 68
Figure 26. Diffractograms of LDPE for different molding conditions: (a) 3 MPa and different cooling rates, (b) 3 MPa and 135, 150 and 165 ºC, and (c) 150 °C and 11, 17, 22 and 28 MPa.. 71
Figure 27. Surface tension of the samples produced under different molding pressure, as measured in water and n-hexane..... 76
Figure 28. Simulated T_m from Eqn. (5.2) for *l*: 1.01, 1.26, 1.52, 2.03 and 3.04 nm (c = 2.5534 Å, explained in 2.17.) to 1/x. 80
Figure 29. Gibbs-Thomson representation of the experimental (circle) and simulated (square) T_m as a function of 1/*l* for isolated alkane chains nanocrystal and compared with the simulated (triangle) T_m for alkane chains nanocrystal in an amorphous phase..... 81
Figure 30. Mean square deviation of one particle on surface of alkane chains crystal at T=440 K $T>T_m$ by 4a4b5c, isolated alkane chains crystal (square), alkane chains crystal within amorphous phase (circle) and one particle in amorphous phase(triangle). 83
Figure 31. Modified Gibbs-Thomson equation representation reporting experimental (circle) and simulated (square) T_m/T^o_m for isolated alkane chains nanocrystal and experimental (inverted triangle) simulated (triangle) T_m for alkane chains nanocrystal in amorphous phase versus 1/*l*.. 84
Figure 32. Gibbs-Thomson representation of the simulated T_m versus 1/*l* at 0 (square), 1000 (circle), 1500 (triangle), and 2000 (inverted triangle) atm. 88
Figure 33. Effect of pressure on melting temperature of Polyethylene crystal: Comparison between experimental (circle) [7] and simulation (square) data by 4a4b3c alkane chains crystal within amorphous phase 89

LIST OF TABLES

Table 1. Main polyethylene properties 9
Table 2. Configuration and nanocrystals chain numbers 46
Table 3. Sample codes and molding conditions to produce the samples 58
Table 4. Sample code, molding conditions, melting point, heat of fusion and degree of crystallinity of the samples produced at 3 MPa and different temperatures 65
Table 5. Sample code, molding conditions, melting point, heat of fusion and degree of crystallinity for the samples produced at 150 °C and different pressures 67
Table 6. Molding conditions, melting point, heat of fusion and degree of crystallinity for the samples produced at 3 MPa and different cooling rates 68
Table 7. Molding conditions, melting point, heat of fusion and degree of crystallinity for the samples produced at 3 MPa and different temperature profiles 69
Table 8. Molding conditions, tensile strength, elongation at break, flexural and Young's moduli for the samples produced at 3 MPa and different temperatures 69
Table 9. Molding conditions, tensile strength, elongation at break, flexural and Young's moduli for the samples produced at 150 °C and different pressures 71
Table 10. Molding conditions, tensile strength, elongation at break, flexural and Young's moduli for the samples produced at 3 MPa and different cooling rates. 72
Table 11. Molding conditions, tensile strength, elongation at break, flexural and Young's moduli for the samples produced at 3 MPa and different temperature profiles 74
Table 12. Slope (α) and the ordinate at the origin (β(l) of Eqn.(2) for different *l* values. 79
Table 13. Crystal dimensions, enthalpy, entropy, surface tension, difference of energy, melting temperature and volume of alkane chains nanocrystal. 85
Table 14. Parameters for non-bonding energetic term 93
Table 15. Partial charge for nonbonding energetic term 94
Table 16. Parameters for bonding energetic term 94
Table 17. Parameters for valence energetic term 94
Table 18. Parameters for dihedral angle energetic term 95
Table 19. Parameters for cross terms (bond-bond, bond-angle) 95
Table 20. Parameters for cross terms (angle-angle) 95
Table 21. Parameters for cross terms (End_bond-torsion, middle_bond-torsion); ($kcalmol^{-1}Å^{-1}$)96
Table 22. Parameters for cross terms (angle-angle, Angle-angle-torsion); ($kcalmol^{-1}deg^{-1}$) 96

INTRODUCTION

A) Investigation of Melting Point and Interfacial Tension using Gibbs-Thomson Equation in Polyethylene Nanocrystal System (Simulation Study)

The concurrent presence of crystal and amorphous components among bulk semi-crystalline polymers definitively explain the difference between the melting and crystallization temperatures, which is not witnessed in low molar mass systems. The crystallization phenomenon recently became a source of debate, revealing that both melting, and crystallization are not clearly understood. The slope difference in the Gibbs-Thomson (GT) equation observed between both phenomena increases this debate. Thanks to molecular simulations providing a description of interactions between atoms, interesting information can be obtained for a better description of these phenomena. Recently, our group showed that the melting of nanocrystals constituted of alkane chains obeys the GT equation as very good agreement was obtained with experimental data [1]. Here, we propose to approach the real polymer, and thus to unveil the GT equation, by embedding the nanocrystals of alkane chains in an amorphous phase using MD simulation.

It is known that polymer chain connectivity and interface have an important effect on the crystals structure leading to different properties. The presence of amorphous regions and their connectivity through chains and adjacent lamellae influence the high degree of plastic deformation in polymers. When the chains are very short, insufficient “tie chains” between the lamellae produces brittleness in the materials [2]. In addition, it was observed that the properties of nanomaterials and their corresponding bulk materials are different [3, 4]. The predominance of interfacial phenomena leads to variation of the macroscale law to the nanoscale field [5]. The physico-chemical processes occurring within length scales of surfaces and interfaces of a few Angstroms are responsible for wetting, adhesion, friction, crystal growth and many other materials phenomena. The bulk processes play very important role in material function like for the rheological properties and adhesion of a pressure-sensitive adhesive. However, its complete behavior is often limited by the processes occurring at the interfaces. This is why material scientists try to explain interfacial phenomena on some common grounds based on two fundamental interface properties: energetics of interactions and dynamics [6].

One of the most significant physico-chemical parameters in several polymer engineering processes, such as fiber, film and foam processing, is interfacial tension (γ) [7]. In general, interfacial tension decreases with increasing pressure which can be explained by the decreasing Gibbs free energy during crystallization at high pressure-induced crystallization in comparison with ambient conditions [7]. The self-consistent field theory (SCFT) [8] and experimental data both confirm this behavior interfacial tension can be obtained from the change of Gibbs free energy (G) with respect to the surface area (A) at constant temperature (T) and pressure (P) as:

$$\gamma = \left(\frac{\partial \mathrm{G}}{\partial \mathrm{A}}\right)_{T,P} \tag{1}$$

SCFT is an equilibrium statistical mechanical approach to determine morphology in polymer systems. The free energy function is minimized to find the lowest energy morphology by this method. The procedure for deriving such function is explained in a number of review papers [9-12]. Because of limited amount of information available for nanocrystal polymers such as polyethylene produced at high pressure and temperature, more in depth studies on the effect of processing conditions and polymer chain structure are definitely important to improve our knowledge about the parameters controlling the ultimate materials properties [13].

The other factors controlling the nanocrystal properties are nanoparticles size and dimension [14,15]. It was observed that melting temperature and enthalpy both depend on the polymer nanocrystal size [16,17]. The size effect can be seen in the GT equation, and the interfacial effects need to be considered. The melting temperature of n-alkanes in bulk was reported in NPT (constant pressure and temperature) ensemble [18]. Furthermore, the melting transition of polymer crystals like isotactic polypropylene and polyethylene were investigated using atomistic simulation [19]. The melting transition points of functionalized polyolefins was studied as approximated by nanoparticles and their behavior was demonstrated [20]. The effect of nanoparticle size on the melting point of polymers has been shown. This size effect will be discussed in our system as well.

Nowadays, different methods are used to determine polymer crystallinity and melting, but most of them are destructive. They often require significant experimental (handling, preparation and measurement) time. Experiments on nanoscale objects are often limited by uncertainty because of the difficulty of producing and manipulating these objects at length scales below 10 nm. Moreover,

it has been difficult to synthesize polymer crystals of such small size especially for inorganic particles. Computational tools are effective ways to clarify experimental observation such as melting and crystallization process [21]. Recently, several groups have tried to describe and understand these processes by using computer simulations based on various models [22-27].
Here, simulation results and experiments can be at the same time compared. If a true model close to semi-crystalline polymer can be found, the effect of processing conditions such as pressure on the thermal and mechanical properties of polymers can be evaluated.

B) Impact of Processing Conditions on Thermal and Mechanical Properties of Molded Polyethylene Samples (Experimental Study)

In industry, end user plastics products are manufactured by different polymer processing techniques such as injection molding, blow molding, blow film extrusion, compression molding, etc. Since the resins must be heated above their melting point to flow, most processing methods are operated at elevated temperatures and pressures [28,29,30]. These conditions will change the nature of the macromolecules and the final polymer structure referred to as the morphology, which is also controlling the crystallization mechanisms and kinetics of semi-crystalline polymers. For polymers such as polyethylene, the constitution of the macromolecular chain will affect the morphology and crystallinity. Synthesis of this polymer automatically leads to branching. So branching type, frequency and distribution, as well as molecular weight of the chains are all factors characterizing a particular polymer properties. The knowledge of the final structure in a molded part is of high importance as the morphology and crystallinity play a significant role on the ultimate mechanical and physical properties of the final product such as permeability, toughness, elasticity, strength, transparency, etc. [31].

Crystallization temperature and rate, as well as molecular weight and pressure are also key factors influencing the crystals lamellar thickness controlling the melting temperature. Higher temperature at constant pressure, higher pressure at constant super-cooling state, and higher molecular weight are known to produce thicker lamellae [32,33].

When polyethylene crystallizes at low temperature, the driving force for crystallization is larger leading to rapid crystals formation in the melt. These crystals are thinner and melt at lower temperatures (T_m). Conversely, when crystallization occurs at elevated temperatures, this gives the chains sufficient time to rearrange and form thicker and more stable crystals having higher melting temperatures [34].

The most stable form of polyethylene is the orthorhombic crystal form (Pnam space group), with two polymer chains per unit cell at atmospheric pressure [35]. At higher pressure, the polyethylene structure changes to a disordered hexagonal or pseudo-hexagonal phase [36,37]. But chain structure also has a strong effect on the thermal properties of polyethylene. For example, the melting point of high density polyethylene (HDPE) has higher pressure dependence when compared with low density polyethylene (LDPE) [38]. Presence of long chain branching in LDPE physically hinders chain mobility and reduces the length of crystallizable chain segments or sequences. The melting temperature-pressure curves for crystalline polymers have also been studied for branched polyethylene, polypropylene and poly(1-butene) [39,40,41].

From the Clapeyron equation:

$$\frac{\mathrm{dP}}{\mathrm{dT}} = \frac{\Delta \mathrm{S}}{\Delta \mathrm{V}} = \frac{\Delta \mathrm{H}}{T_m \Delta \mathrm{V}} \qquad (2)$$

By considering the values of ΔH and ΔV, P(T) can be obtained.

The pressure dependence of the melting point in a variety of polymers including homo and copolymers (HDPE, LDPE, PP and ethylene vinyl acetate copolymers (EVA) was investigated under a nitrogen atmosphere up to 330 MPa [37,42,43].

A number of publications emphasized that mechanical properties of polymers are strongly dependent on the stress applied upon melt processing [44,45,46]. As expected, higher pressure is known to increase the elastic modulus, the tensile strength and the elastic limit. For example, higher Young's modulus with increasing molding pressure is known to be the result of three factors: a change in the interatomic distance, a decrease in the specific volume (lowering the free volume), and the finiteness of the deformation [47]. Experimental investigations on polymer

crystallization at high pressure showed that linear polyethylene has a higher density approaching the perfect crystal density calculated from the crystal lattice theory [48].
Recently, functionally graded materials (FGM) were developed where the structure and/or composition are gradually changed with position inside the molded component. The gradation inside the material can be the result of a position-dependent chemical composition, microstructure or atomic order [49]. The easiest way to produce FGM is by imposing a temperature gradient inside the mold to generate symmetric or asymmetric samples [50,51], leading to improved mechanical properties or stability compared with uniform (homogeneous) materials made under constant/uniform temperature and pressure.
In this work, the interfacial tension behavior of LDPE (low density polyethylene) at low pressure was investigated in order to compare with simulation data.

This thesis is organized as follows. Chapter I presents the theoretical framework by reporting on the theories and concepts relevant to the research topic. In particular, three types of polyethylene are compared with each other. Moreover, several models for semi-crystalline polymers are introduced. Then the fundamental concepts of the melting phenomenon and Gibbs-Thomson equation in crystalline polymers are explained. Finally, the objectives of this study are presented.

In chapter II, the importance of polymers simulation and several methods to obtain their thermodynamic and mechanical properties, as well as their crystallinity are presented. Molecular dynamics (MD) simulation is introduced and the key concepts are presented for a proper understanding of these calculations with more details. In addition, the technique of MD to set alkane chains nanocrystal in an amorphous phase is specified. Then, the steps to perform a complete simulation for our system are explained.

Chapter III introduces two essential methods in the polymer molding industry. Then, a number of mechanical and thermal properties of polymers are presented. The methods to produce compression molded polyethylene samples are given. Finally, the effect of pressure, temperature and cooling rate on the crystallinity, mechanical and thermal behavior of polymers are reviewed.

In chapter IV, a discussion about the effect of processing conditions on the thermal and mechanical properties of LDPE is presented. Several samples produced under different mold temperature, pressure and cooling rate were investigated to determine how the compression molding conditions influence the enthalpy, melting temperature, degree of crystallinity, and mechanical properties (elongation at break, tensile and flexural moduli). Finally, it was shown that increasing the molding pressure results in lower interfacial tension.

Chapter V focusses on the main simulation results. A comparison on the heat of melting per CH2 (units) in alkane chains nanocrystal embedded in an amorphous phase is made by computing the melting temperature of crystals with different chain length. Moreover, the effect of polymer chain connectivity and interface on polyethylene properties like interfacial tension, melting point and enthalpy is reported. In addition, the effect of pressure increase as an environment effect on interfacial tension is studied via the Gibbs-Thomson equation. This result was confirmed by experiment.

Finally, general conclusion from the results obtained are presented and recommendation for future work are proposed.

CHAPTER I. Literature Review and Objectives of Project

1.1. Introduction to Polyethylene

Chemically pure polyethylene resins are composed of alkanes chains of formula $C_{2n}H_{4n+2}$, where n is the degree of polymerization. All types of polyethylene have the same backbone of covalently linked carbon atoms. The differences come from branching modifying the nature of each grade. These side chains are different from simple alkyl groups to acid and ester functionalities. Generally, higher branches concentration leads to lower solid density [52].

1.1.1. High Density Polyethylene

High density polyethylene (HDPE) corresponds the most to pure polyethylene. It includes primarily unbranched chains with very few defects. The general form of high density polyethylene is shown in Figure 1.a.

1.1.2. Low Density Polyethylene

Low density polyethylene (LDPE) consists of polymers with substantial concentration of branches limiting the crystallization process and leading to relatively low densities. The branches contain ethyl and butyl groups together. The structure of low density polyethylene is presented in Figure 1.b.

1.1.3. Linear Low-Density Polyethylene

Linear low-density polyethylene (LLDPE) resins contain molecules with linear polyethylene backbones to which are substituted short alkyl groups at random intervals. These molecules are produced by the copolymerization of ethylene with 1-alkanes (usually C_4 to C_6). The general structure of linear low-density polyethylene resins is schematically shown in Figure 1.c.

1.1.4. Very Low-Density Polyethylene

Very low-density polyethylene (VLDPE), also recognized as ultralow density polyethylene, is a specialized form of linear low density having much higher concentration of short-chain branches [52].

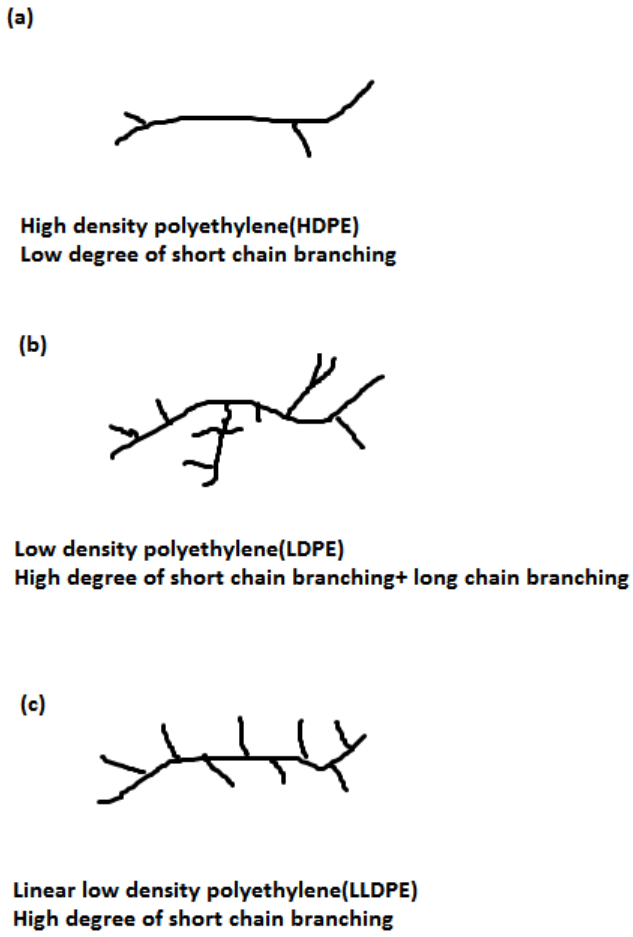

Figure 1. The general structure of high density, low density and linear low density polyethylene

1.1.5. Spherulite Structure

Semi-crystalline polyethylene is formed by crystallites and disordered regions between them. When the amount of crystalline regions is high, the growth of crystallite leads to “spherulites”. They are called spherulites because their growth is close to be spherical, but they are lamella growing radially outward from nucleation sites [53]. A schematic representation of a spherulite is given in Figure 2.a.

1.1.6. Crystalline Structure

When polyethylene crystallizes, the crystals are of finite sizes and of limited extent. The small crystals forming the crystalline regions of solid polyethylene are called crystallites. The most common crystal growth method for polyethylene, which is a crystallites in both x and y dimensions

much larger than its L dimension, are termed “lamellae”. An idealized representation of a lamella is shown in Figure 2.b. A polyethylene lamella typically is 50 to 200 nm thick. Their lateral dimensions can change in orders of magnitude from a few hundred Angstroms up to several millimeters for crystals grown from solution [52].

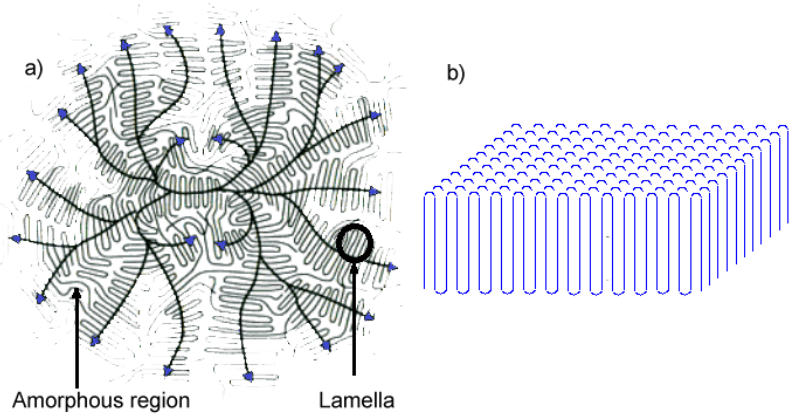

Figure 2. Schematic representation of: a) spherulite structure [53] and b) crystalline structure [52]

1.1.7. Intrinsic Properties

The different polyethylene grades display a wide range of properties depending on their molecular and morphological characteristics. Each type of polyethylene has its own characteristics and spectrum of properties. But properties overlaps between the different grades exist [52].

Polyethylene is used in a wide range of applications. The semi-crystalline structure is important for most applications because the morphology can be controlled by molecular properties and processing conditions. Toughness, hardness, clarity and other physical characterization of semi-crystalline polyethylene can be controlled by changing its molecular weight, comonomer type and content [52].

The annual polyethylene production exceeds 80 billion pounds, of which approximately 35% is utilized in United States [52]. High density, low density and linear low-density polyethylene are the main resins used, although ethylene-vinyl acetate copolymer (EVA), very low density polyethylene and ionomers are used in much lower quantity.

Table 1. Main polyethylene properties [52]

Property	HDPE	LDPE	LLDPE
Density (g/cm^3)	0.94-0.97	0.91-0.94	0.90-0.94
Degree of crystallinity (% from density)	62-82	42-62	34-62
Degree of crystallinity (% from calorimetry)	55-77	30-54	22-55
Flexural modulus (psi)	145,000-225,000	35,000-48,000	40,000-160,000
Tensile modulus (psi)	155,000-200,000	25,000-50,000	38,0000-130,000
Tensile yield stress (psi)	2,600-4,500	1,300-2,800	1,100-2,800
Tensile strength at break (psi)	3,200-4,500	1,200-4,500	1,900-6,500
Tensile elongation at break (%)	10-1,500	100-650	100-950
Melting temperature (^{0}C)	125-132	98-115	100-125

1.1.8. High Density Polyethylene Synthesis

Ziegler was the first to study and report on the reaction of certain organometallic compounds to produce polymers [54]. Chromium complexes were considered as catalysts for the polymerization of ethylene to form a mixture of oligomers including some high molecular weight polymer. The new polyethylene structure, with negligible branching, showed many superior properties to those of highly branched molecules [54].

1.1.9. Low Density Polyethylene Synthesis

The application of tandem catalyst was found as an easy synthesis route for the production of linear low-density polyethylene. Homogeneous tandem catalytic systems are used for the synthesis of ethylene/1-hexene copolymers from ethylene stock as the sole monomer [52].

1.2. Models for Semi-Crystalline Polymers

There are two models to describe semi-crystalline polymers.

1.2.1. Fringed-Micelle Model

Gerngross and Abitz proposed the fringed-micelle model to explain the structure of gelatin [55,56]. It was one of the earliest morphological models of semi-crystalline polymers. This model is composed of two phases: crystalline and amorphous regions. The crystalline regions contain stacks

of different short length chains aligned parallel to each other, while the amorphous regions are comprised of disordered conformations [Figure 3.a]. The parts of the chains moving from the crystalline zone to the amorphous region are called "fringes".

1.2.2. Chain-Folding Model

Keller reported that polyethylene single crystal grows from dilute solution under an electron microscope [57,58]. He found that these lamellae had a thickness around 100 Å and proposed a “chain-folding" model with the concept of chain folding in the crystallites. The chains in semi-crystalline polymers moved from a crystallite, re-entered the crystallite at neighboring positions in the shape of hairpin-like bends [59]. Chain axes are directed approximately perpendicular to the basal faces [60].

The lamella aggregation is often in the form of a spherulite when crystallized from the melt. As described in section 1.1.5., the spherulites are shaped like spherical aggregates of lamella coming from a center and radiating towards the bulk. Then, Storks showed the existence of a lamellar structure in gutta-percha (a natural polymer) while doing electron diffraction [61].

There are two different structures for the chain-folding model. In a model of tight folding or "adjacent re-entry" [59], the chains fold at the surface of the lamella to form a loop and occupy the neighboring sites (Figure 3.b). On the other hand, the "switchboard random" model proposes that the chains can fold at the surface of the lamella by forming a loosely packed loop and return to the farthest location (Figure 3.c).

These entanglements stay in the residual amorphous phase during crystallization from the melt. Lamellar crystals develop by folding the chains parallel to the crystallographic axis. So, the crystals form long ribbons (like in PE or PVDF (polyvinylidene difluoride)) or needles (like in polyamides). In general, the lamellae length is of the order of several microns. Polarized optical microscopy (POM) is used to quantify the periodicity of these lamellar stacks [62], as well as small angle X-ray scattering (SAXS) [63].

Under quiescent condition, these types of morphologies are developed during polymer crystallization. The “shish-kebab” structure can be obtained when crystallization occurs under flow [59].

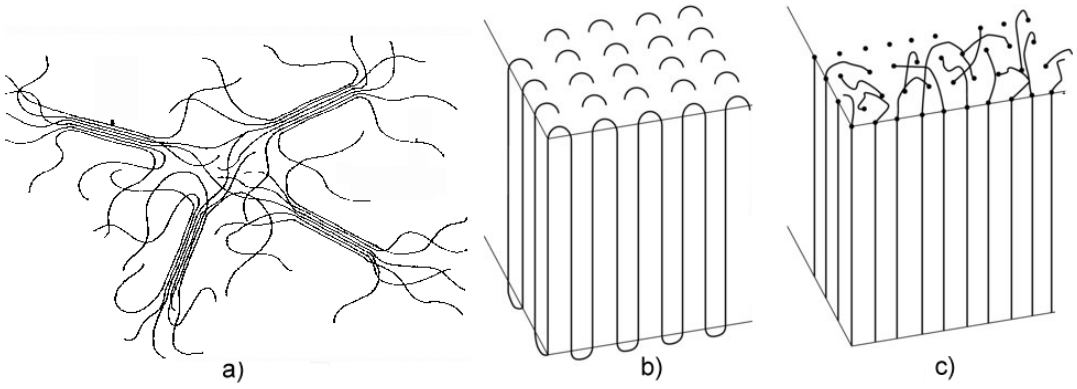

Figure 3. Schematic of: a) fringed-micelle model for semi-crystalline polymers, b) chain-folded lamellar structure with adjacent re-entry and c) switchboard random [59].

1.3. Flory's Crystallization Theory for Homopolymers

Flory's theory [64] for homopolymers crystallization is based on a linear polymer comprised of x identical structural units [65]. The relationship between the equilibrium crystallite length (ζ_e) and other parameters can be written as:

$$-\ln(\nu_2 D) = \frac{\zeta_e}{x-\zeta_e+1} + \ln\left[\frac{x-\zeta_e+1}{x}\right] \cong \frac{1}{x} + \left(\frac{1}{2}\right)\left(\frac{\zeta_e}{x}\right)^2 + \left(\frac{2}{3}\right)\left(\frac{\zeta_e}{x}\right)^3 + \ldots \quad (1.1)$$

where ν_2 is the volume fraction of polymer, and

$$D = \exp\left(\frac{-2\sigma_e}{RT}\right) \quad (1.2)$$

where σ_e is the fold surface free energy per unit area.

It follows from Equation (1.1) that ζ_e increases with either decreasing ν_2 or D. The increase in crystallite length because of increasing the polymer dilution in solution (decreasing ν_2) can be described by higher chain mobility leading to easier diffusion of these chains to the growing

crystallite surface. For large chain lengths, the crystalline length (ζ) is related to the melting temperature (T_m) as predicted by [64]:

$$\frac{1}{T_m} - \frac{1}{T_m^0} = -\left(\frac{R}{h_u}\right) - \left(\frac{lnD}{\zeta}\right) \quad (1.3)$$

where T_m^0 is the melting point of the pure polymer of infinite length chain, and h_u is the heat of fusion per structural unit.

Equation (1.3) shows that the melting point depression below T_m^0 varies inversely with the crystalline length. At a given temperature, crystallites length (ζ) with a melting temperature (T_m) are formed until all the chain sequences have been exhausted.

An elegant theory for polymer crystallization has been proposed by Lauritzen and Hoffman [66-70]. This theory is referred to as the kinetic theory of polymer crystallization. The crystallization range for a polymer can be decomposed in three regions or regimes controlled by the rates of two processes: secondary nucleation and lateral spreading or growth. The rate of these processes is represented as i and g, respectively. So, the three regimes can be defined by:

$g >> i$ Regime I

$g \cong i$ Regime II

$g << i$ Regime III

In Regime I, a single nucleus is formed on a surface and crystal growth continues by the lateral spreading of a single crystalline layer. In Regime II, several nuclei are simultaneously produced and spread along the surface to make new crystalline layers. In Regime III, the secondary nucleation rate is so fast that it reduces any lateral spreading along the crystal surface leading to an uneven fold surface up to the limiting case of Flory's switchboard model.

The free energy of fusion (ΔG_f) for a polymer crystal for the above given conditions is:

$$\Delta G_f = xyl\Delta G^{\infty}_f - 2xy\sigma_e - 2l(x+y)\,\sigma \quad (1.4)$$

where ΔG_f is the free energy of fusion per unit volume for an infinitively large crystal, and

σ_e = the fold surface free energy per unit area,

σ = the lateral surface free energy per unit area and,

x, y and l = the length, width and thickness of the crystal, respectively.

For infinitely large and perfect crystal, σ and σ_e can be neglected.

$$\Delta G_f = xyl\Delta G_f^{\infty} = xyl\ (\frac{\Delta H_f^{\infty}(T)}{T\Delta S_f^{\infty}(T)}) \quad (1.5)$$

At the equilibrium melting temperature (T_m^e), $\Delta G_f^{\infty} = 0$. So, the melting temperature of such a crystal can be simplified as:

$$T_m^e = (\frac{\Delta H_f^{\infty}}{\Delta S_f^{\infty}}) \quad (1.6)$$

The melting temperature (T_m) of a smaller crystal can be calculated by substitution of Equation (1.6) in Equation (1.4). For such a crystal, the following approximations can also be made: $\sigma << \sigma_e$ and x, y >> l. Then, T_m is given by:

$$T_m = T_m^e\ (1 - (\frac{2\sigma_e}{l\Delta H_f^{\infty}})) \quad (1.7)$$

This expression is called the Gibbs-Thomson-Tammann equation [71,72]. It is a variation of the Gibbs-Thomson equation for a crystal of large lateral dimensions and finite thickness.

Based on the Lauritzen-Hoffman theory, the initial lamellar thickness (l_g^*) of a polymer crystal is related to the extent of undercooling (ΔT) as:

$$l_g^* = (\frac{2\sigma_e T_m}{\Delta H_f^{\infty} \Delta T}) + \delta l \quad (1.8)$$

In this equation δl is the variation of thickness.

1.4. Lamellar Thickness in Polymers

The crystals thickness can be controlled by the crystallization conditions and controlled by the degree of undercolling (ΔT) to give:

$$l_c = (\frac{K_l}{\Delta T}) \quad (1.9)$$

where K_l is a material constant defined as [73]:

$$K_l = (\frac{2\sigma_e T_d}{\Delta H_d}) \quad (1.10)$$

where ΔH_d and σ_e are the melting enthalpy and surface free energy for each crystallization conditions, respectively. The melting temperature can be depressed below the equilibrium melting temperature because of highly thin lamellar crystals since the surface free energy destabilize the crystallites.

The effect of lamellar thickness on melting temperatures should be investigated in order to acquire information related to the distribution of lamellar thickness in a crystallized specimen.

1.5. Gibbs-Thomson Equation

According to the given heat of fusion (ΔH_m) surface energy (σ_e) and crystal thickness (l), the variation of T_m with respect to inverse of l is expressed by the Gibbs-Thomson equation which represents a simple effort of fundamental thermodynamic concepts applied to lamellar crystal morphology. For a thin lamella with a thickness much smaller than the lateral dimension (Figure 4), T^0_m is an estimation obtained from the variation of T_m with respect to the crystal lamellar size through Gibbs-Thomson equation.

For a finite size crystal, the free energy change of that crystal is obtained from:

$$\Delta G_{crystal}(T) = 2xy\sigma_e + 2l[x+y]\,\sigma - xyl\Delta G_m(T) \quad (1.11)$$

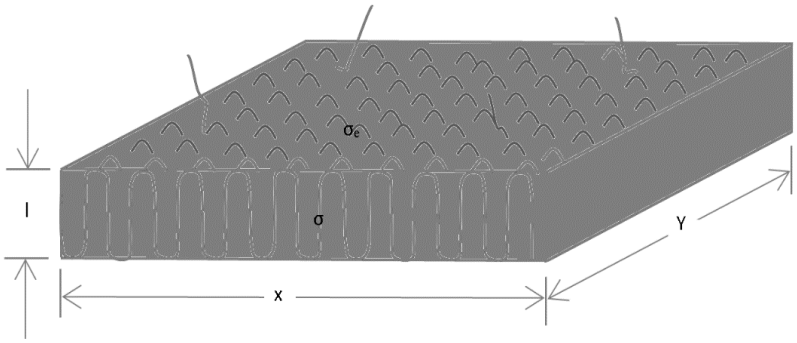

Figure 4. Diagram of a crystalline polymer lamella.

where $\Delta G_{crystal}$ is the free energy of crystallization per unit volume. The melting point is directly dependent on the crystal lamellar size. By combining Equations (1.11) and (1.12a), Equation (1.12b) can be obtained. We will explain how to obtain equation 1.12a in the next section.

$$\Delta G_m = \Delta H_m \left[1- \frac{T_m}{T_m^0}\right] \quad (1.12a)$$

$$T_m = T_m^0 - \left(\frac{2\sigma T_m^0}{l\Delta h_m}\right) - \left(\frac{2\sigma}{\Delta h_m}\right)\left(\frac{1}{x}+\frac{1}{y}\right) T_m^0 \quad (1.12b)$$

Equation (1.12b) can also be written as:

$$T_m(l) = T_m^0 \left[1- \left(\frac{2}{\Delta h_m}\left(\frac{\sigma}{\bar{x}}+\frac{\sigma_e}{l}\right)\right)\right] \quad (1.13)$$

In Equation (1.13), $\frac{1}{\bar{x}} = \frac{1}{y} + \frac{1}{x}$ where $\bar{x}$ is the harmonic mean of the lateral dimensions (x and y), while T^0_m and Δh_m are the melting temperature for infinitely large crystal and melting enthalpy per unit volume of the bulk, respectively. The fold surface free energy and the surface free energy of lateral edges are σ_e and σ. So, Equation (1.13) can be written as:

$$T_m(l) = \phi \left(\frac{1}{\bar{x}}\right) + \kappa(l) \quad (1.14)$$

Where,

$$\phi = -T^0_m[\frac{2\sigma}{\Delta h_m}] \quad (1.15)$$

$$\kappa(l) = T^0_m\,[1 - \frac{2\sigma_e}{\Delta h_m}\frac{1}{l}] \quad (1.16)$$

In Equation (1.14), κ(l) represents the melting temperature of sheets with infinite lateral dimensions ($\overline{x} \rightarrow \infty$), and this equation is equivalent to the Gibbs-Thomson equation. Now, to calculate the melting point dependence on the crystal thickness, a two steps procedure must be followed. Firstly, l is kept constant to let x and y change. As an example, for a constant thickness (l), Figure 5 shows the variation of the melting temperature ($T_m(l)$) with respect to the inverse of $\overline{x}$ (variation of x and y). ϕ and κ(l) can be obtained from the slope and the ordinate, respectively.

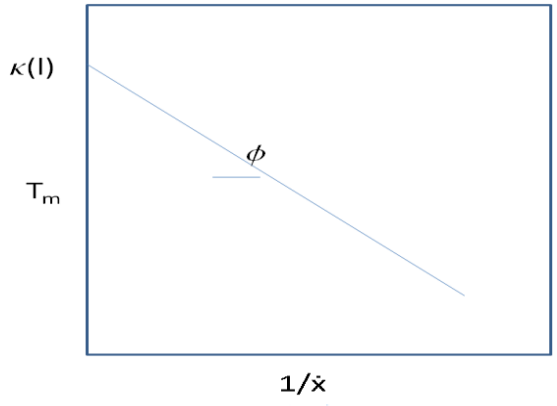

Figure 5. Variation of T_m as a function of length expressed as $1/\bar{x}$

Then, a plot of κ(l) with respect to the inverse of lamellar thickness is made as described in Equation (1.16). A linear regression gives the values of $\sigma_e/\Delta H_m$ and T^0_m from the slope and the ordinate. Following the same method for the crystallization line(crystallization upon heating above T_g), a similar behavior is obtained for the maximum crystallization temperature (T^{∞}_c) in Figure 6 [74]. As suggested by the Gibbs-Thomson equation, there is a relation between the crystallization temperature, the crystal thickness and the location of the melting peak by plotting T_c and T_m as a function of l_c^{-1}. The slope of melting line is:

$$T = T_m^{\infty} - \frac{2\sigma_e T_m^{\infty}}{\Delta h_m l_c} \quad (1.17)$$

In these plots, the crystallization line has a higher slope than the melting line and intersects the latter at a finite value of l_c^{-1} leading to a surprising result where the crystallization temperature should be higher than the melting temperature [75]. Strobl explained the difference in the slope by introducing the multi-step process of the crystallization process. It is observed that the initial step is the creation of a mesomorphic layer. It thickens up to a critical value and followed by solidification through a structural transition which makes a granular crystalline layer. In the last step, it transforms into homogeneous lamellar crystallites [75].

In the next chapter, a discussion about the simulation of a polyethylene nanocrystal with infinite dimensions is presented to determine its melting point inside an amorphous phase, trying to closely simulate a real semi-crystalline system. But semi-crystalline polymer crystallization and melting are slow processes in compared with a molecular time scale. Moreover, to simulate these processes, chain lengths must be large enough to give experimentally realistic situations. So, the simulation of these processes is a very challenging task. MC (Monte Carlo) simulations on a lattice were used to model the formation of lamellar thickness in the crystal [76–79]. In this model, it is assumed that a growth front preexists between the crystalline and amorphous regions. Short chains in the melt and clusters in vacuum or thin films can be simulated by direct MD (molecular dynamics) simulation [80]. Coarse-grained (CG) and united-atom (UA) models can be combined with MD methods to make reasonable resolution on an atomic length scale to simulate semi-crystalline polymers [81,82]. As an example, Meyer and Müller-Plathe developed a CG polymer model to simulate the crystallization processes of poly (vinyl alcohol) (PVA) [83].

1.6. Thermodynamics of Fusion

Below the equilibrium melting point (T_m^0), a crystal has a lower free energy than the liquid. The melting point of the pure polymer with infinite chain length can be adressed by the equilibrium melting temperature. It is one of the most essential thermodynamic properties in crystalline polymer chains. At T_m^0, both phases (crystal and liquid) exist and have the same value of molar Gibbs free energy so $\Delta G_m = 0$. The variation of molar Gibbs free energy for the liquid and crystal with respect to the temperature is shown in Figure 7a, while the Gibbs free energy as a function of

pressure above T_m^0 differs from that of below T_m^0 because the melt and crystalline polymers have different molar volume. This behavior can be confirmed by the first order transition explained by Ehrenfest [84].

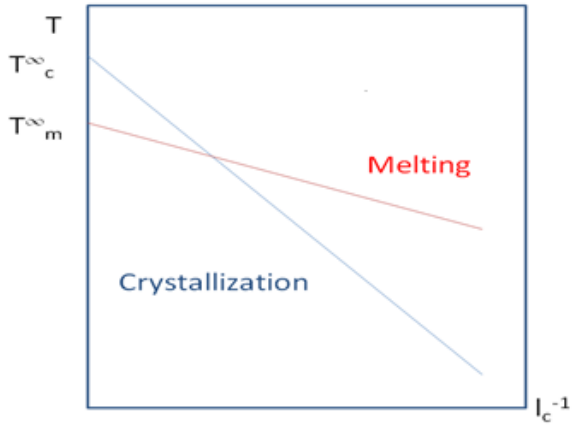

Figure 6. Variation of transition temperatures with respect to the inverse of crystal thickness for the crystallization (blue) and melting line (red)

For a pure, one component system, one can write:

$$dG = VdP - SdT \tag{1.18}$$

where V and S are the volume and entropy of the phase, respectively. Considering the partial derivatives of G with respect to temperature and pressure in Equation (1.18) gives:

$$(\delta G/\delta T)_p = -S \tag{1.19}$$

$$(\delta G/\delta P)_T = V \tag{1.20}$$

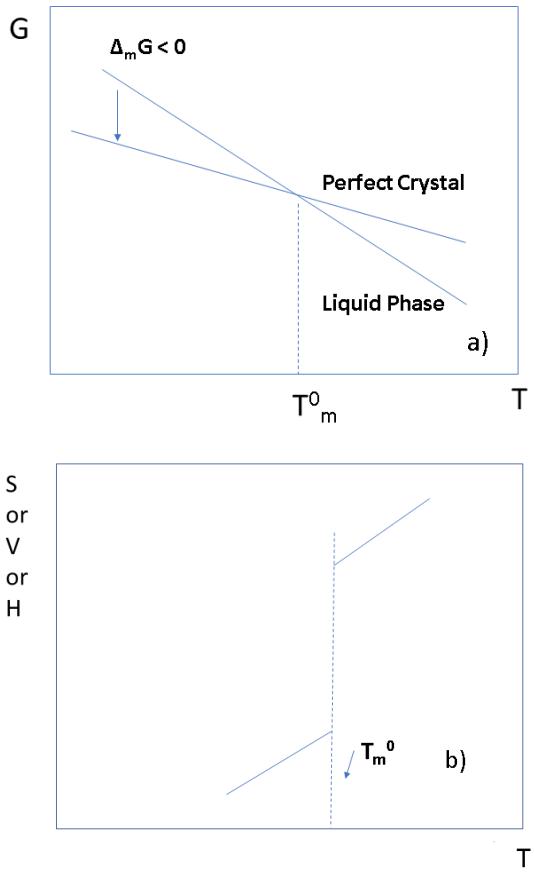

Figure 7. General behavior of thermodynamic state functions as a function of temperature: (a) Gibbs free energy and (b) entropy, enthalpy and volume

At the equilibrium melting temperature (T_m^0), the variation of Gibbs free energy for crystallization is:

$$\Delta G_m = \Delta H_m - T_m^0 \Delta S_m = \Delta H_m \left(1 - T \left(\frac{\Delta S_m}{\Delta H_m}\right)\right) \quad (1.21)$$

Considering $\Delta G_m = 0$ leads to:

$$T_m^0 = \frac{\Delta H_m}{\Delta S_m} = \frac{H_l - H_{cr}}{S_l - S_{cr}} \quad (1.22)$$

where H_l, H_{cr}, S_l and S_{cr} are the enthalpy and entropy of the liquid (l) and crystal (cr) phase, respectively. Combining Equations (1.21) and (1.22) gives:

$$\Delta G_m = \Delta H_m \left[1 - \frac{T_m}{T_m^0}\right] \quad (1.23)$$

ΔH_m depends on the interactions between all the molecular chains and is almost constant with respect to crystalline structure. However, ΔS_m depends on the chain conformation in the crystalline states. Practically, the entropy effect cannot be neglected and both ΔS_m and ΔH_m must be accounted for.

1.7. Objectives of Project

In the experimental part of this project, LDPE is compression molded under different conditions. Surface tension of the samples made at several pressures is measured by a tensiometer. Furthermore, the effect of processing conditions (mold temperature, mold pressure, cooling rate, and temperature profile (mean temperature gradient inside the compression mold between the two plates) on the tensile and flexural moduli, melting point and crystallinity degree of the samples is also studied.

As discussed before in the simulation part of this project, alkane chains nanocrystal are set within the amorphous phase in a cell with periodic boundary conditions to approach a real polymer. The aim is to unveil the GT equation. Then, the effect of polymer chain connectivity and interface on the polyethylene properties like melting temperature, interfacial tension and enthalpy is investigated.

The value of melting temperature for infinite dimensions is reported and compare the ensuing results with experimental data on a polyethylene crystal. Experimental and simulated series of data are discussed using the Gibbs-Thomson equation. By calculating the crystals melting temperature with different thicknesses, the heat of melting per CH_2 (units) in the alkane chains nanocrystal is reported. The effect of interactions with neighboring chains can thus be observed

by comparing the mean square deviation (MSD) of one particle on the crystal surface stemming from the isolated crystal and a crystal in the amorphous phase. The presence of amorphous regions and their interaction between the chains to unbonded monomers of the crystal decreases the chains mobility and entropy following leading to a melting temperature increase and a decrease of interfacial tension in comparison with isolated alkane chains crystal.

In the second part of the simulation work, the effect of pressure increase as an environmental effect on surface tension is investigated via the Gibbs-Thomson equation. The pressure dependence of the melting point is determined up to 3000 atm. Also, the surface tension is determined to relate the effect of pressure on the mechanical properties. It is found that increasing pressure led to lower total entropy of fusion which follows the increase of melting temperature and lower Gibbs free energy leading to lower surface tension. This result is confirmed by experiment.

CHAPTER II. Review of Polymer Simulation Methods and Molecular Dynamics

2.1. Introduction

In this Chapter, the importance of polymers simulation was emphasized, and a number of methods used to simulate and obtain their thermodynamic and mechanical properties is presented. The principles of Molecular Dynamics (MD) simulation, which is the main method used in this study, were introduced. The basic MD simulation equations are presented in the following sections. Therefore, fundamental procedures used in MD simulation will be explained in more details. Then, explanations on how a system containing polyethylene nanocrystals embedded in an amorphous phase have been prepared will be presented.

2.2. Simulation of Polymers

Polymers are an extremely wide area of interest. Not only they offer many industrial applications, but their investigation remains a great source. They are in the simplest case, long-chain molecules with some repeating functional groups. Polymers have the same fundamental forces of bonding and intermolecular interactions as for small molecules. But, several polymer properties are influenced by size effects (due to their long chain length). Therefore, simply applying small-molecule modeling techniques is not sufficient to study polymers [85].

Polymers are complex systems for several reasons. Most of them are amorphous or amorphous with some crystalline domains. Moreover, since most methods do not anneal the material slowly enough to get an optimum conformation (equilibrium), polymer system is usually in a non-equilibrium state. The polymer properties vary with the processing conditions (i.e. cooling rate, temperature, pressure, etc.) as well as the molecular structure. The main intermolecular interactions in polymers are van der Waals forces, hydrogen bonding, π stacking, and electrostatic interactions. For synthetic polymers, long-range effects seem to be more important than for other long chain molecules like proteins.

Because of the extremely slow relaxation in polymer systems there is no possibility of performing a simulation for the dynamics of, as an example, a melt with chemical details [85]. The models have to be as idealized as possible. Besides, due to the large size of microcrystalline domains and

the complexity of simulating non-equilibrium systems, it is difficult to model polymer systems. One method to work with these systems is the use of mesoscale techniques such as coarse-grained molecular dynamic, dissipative particle dynamics, Brownian dynamics and lattice Boltzmann simulation [86]. Mesoscale technique has been a useful approach to predict the conformation of microscopic crystalline and amorphous parts. The first atomistic MD simulations of chain molecules were performed for small alkanes, such as C4 and C8, and mainly focused on static properties. It is now easily accessible to track simulations on the order of 90 ns for very large systems. In parallel, the technique of nonequilibrium molecular dynamics (NEMD) has been used, mainly because of its advantage in calculating viscosity by imposing a shear flow on the system [87].

Furthermore, several techniques are practical for simulating the amorphous phases. QSPR (quantitative structure property relationships) techniques give several properties such as mechanical properties dependent on glass transition temperature (T_g) by the knowledge of the repeating unit size, but they are not reliable near this temperature [87]. Molecular mechanics can also be performed. In this method, the energy for a section of the bulk material is calculated within a periodic boundary condition and then the size of the box is varied to optimize the system again to obtain a second energy [88].

2.2.1. Polymers Properties

In chapter IV, the effect of mold temperature, pressure and cooling rate on the degree of crystallinity, thermal and mechanical properties of LDPE samples will be reported based on experimental measurements. Thus, several methods and models are reviewed here to obtain the properties of semi-crystalline polymers by simulation.

Selection of the simulating method for a polymer must be based on the properties to be predicted. These properties can be divided in two categories: material properties depending on the nature of the polymer chain itself, or specimen properties which are function of the size, shape, and phase of the final molded objects. Hence, material properties are managed by the choice of monomers, whereas specimen properties are controlled by the processing conditions [85].

Material properties include fundamental properties and derived properties. Van der Waals volume, cohesive energy, and heat capacity are examples of fundamental properties having a direct effect

of the molecular structure. Derived properties are not readily involved in molecular structure. Glass transition temperature, density, solubility, and bulk modulus are examples of derived properties [85].

The way in which fundamental properties are measured from simulation is often clear and by making the configuration, they can be easily calculated. However, derived properties are often empirically specified combination of fundamental properties. But sometimes these empirical methods are reliable for one class of compounds, and not for another, leading to inconsistent results.

Density, porosity, and so forth can be determined by the polymer geometry. So, one of the strength of computational modeling is to specify whether the material properties can justify a synthesis effort [85].

2.2.1.1. Polymers Crystallinity

Polymers can be crystalline, but not all of them can easily crystallize. Computational studies can predict whether a polymer is likely to crystallize or not. There may be many conformers with the same energies. So, the most stable structure from possible conformers of oligomers must be found. To get this information, the differences between low-energy conformers can be computed.

To get a crystalline state, polymers must have enough freedom of motion. Polymer crystals nearly always include many strands with a parallel shape. Whether the strands are parallel does not ensure that they will have the sufficient freedom of movement to have the low-energy conformer. Investigations can verify this by examining the polymer cross-sectional profile. It is a method in material science to find the position and in further, movements of particles. When it is approximately circular, it means that the chains have enough freedom of movements and vary conformation as necessary.

2.2.1.2. Thermodynamic Properties

Not only some information can be obtained from the polymer structure, but also useful data are gained through thermodynamic relationships. As an example, heat capacity is calculated from the molecular structure and a function of temperature, Cp (T). By examining the vibrational motion of the atoms and rotational degrees of freedom, the heat capacity can be calculated. Since a

discontinuous change in heat capacity occurs at the melting temperature, different algorithms may be used for the solid and liquid-phase heat capacities.

2.2.1.3. Mechanical properties

In engineering applications, mechanical properties are essential. These properties are termed as stress-strain relationships by computing the amount of energy (stress) required to give a certain amount of material deformation (strain). They depend on crystallinity, orientation, and crosslinking. They are also dependent on the material processing, so this is why they are complex to predict, and molecular modeling techniques are more useful to investigate a large range of conditions.

2.3. The Objective of Molecular Dynamics

Practically, computer simulations are performed to better understand the properties of molecules ensembles with their structure and the microscopic interactions in them. This works as a complement to conventional experiments, help us to learn something new which cannot be retrieved by other techniques. The two main methods of atomistic simulation technique are molecular dynamics (MD) and Monte Carlo (MC). In addition, some hybrid techniques mixing features from both techniques have been proposed [89]. In this section a focus on MD is made since this is the technique used in our simulations. It is one of the main methods to simulate polymer systems as MD gives a route to dynamic properties such as transport coefficients, time-dependent responses to perturbations and rheological properties. This is the main advantage of MD over MC [89].

Computer simulations behave as a bridge (Figure 8) between microscopic length and time scales with the macroscopic world (laboratory and industry). By providing information on the interactions between molecules, more precise predictions of the bulk properties can be obtained. In other words, simulations work as a link between theory and experiment. But a theory must be tested (validated) by applying a wide range of simulation conditions and comparison with experimental data.

Using MD, the time-dependent behavior of a molecular system such as Brownian motion is catched. But means to calculate the system energy, which most often can be measured by

molecular mechanics calculation, is needed. For any given geometry, forces acting on the atoms can be computed by this energy. The steps in a MD simulation of an equilibrium system are [90]:

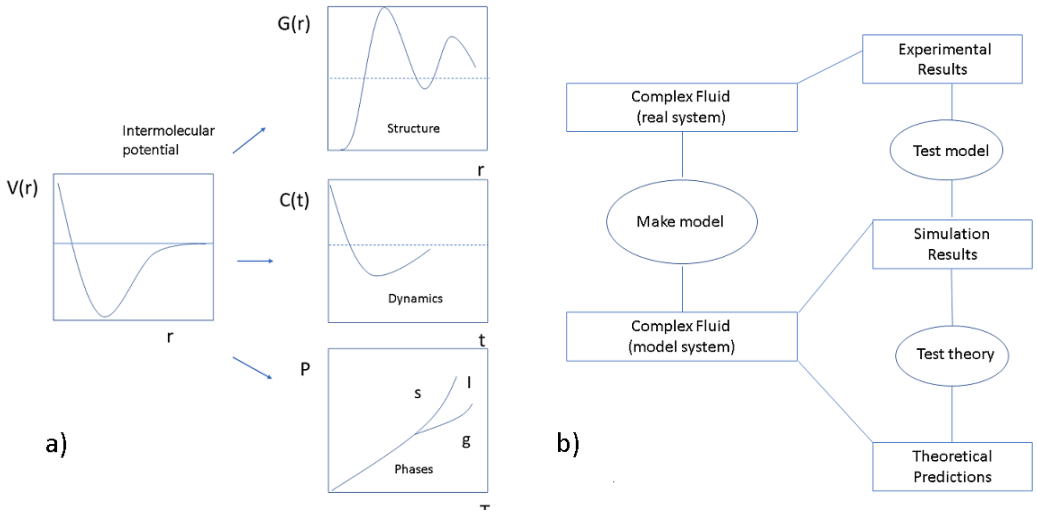

Figure 8. Simulations act as a bridge between different scales: (a) microscopic and (b) macroscopic

1. Selection of initial positions for the atoms,
2. Selection of an initial set of atom velocities. They should follow the Maxwell-Boltzmann distribution and be normalized so that the net momentum for the entire system is zero,
3. Compute the momentum from velocity and mass for each atom,
4. Compute the forces acting on each atom from the energy values,
5. Compute new positions for the atoms a short time later (time step) using the information obtained from the previous steps. This is a numerical integration of Newton's equations,
6. Compute new velocities and accelerations for each atom,
7. Repeat this iteration (steps 1-6) until the system reaches equilibrium. Equilibrium is not the lowest energy configuration, but a configuration having a “reasonable” amount of energy for the system,
8. Save the atomic coordinate every few iterations, when the system reached equilibrium. This information is usually saved every 5 to 25 iterations. A trajectory is a sequence of coordinates over time,

9. Continue saving data until sufficient data are obtained to get results with the desired accuracy,
10. Analyze the trajectories to get information about the system. Some physical properties like radial distribution function, diffusion coefficient, and vibrational motions can be calculated.

MD simulation includes the numerical solution of the classical equations of motion. For this purpose, the forces must be calculated which are usually derived from a potential energy $u(r^N)$, where $r^N = (r_1, r_2, \ldots, r_N)$ showing the complete set of 3N atomic coordinates [89].

2.4. Time Dependence

Time-dependent statistical mechanics is important for two reasons. At first to link with experiment, an understanding of equilibrium time correlation functions, their relationship with dynamical properties, and especially their connection with transport coefficients, are highly essentials. Secondly, there is a rapid development of the use of non-equilibrium molecular dynamics, with a better understanding of the formal aspects, mainly the relation between the dynamical algorithm, dissipation, chaos, and fractal geometry.

A set of initial coordinates and velocities, with an interaction potential (energy function) are needed to start a dynamic simulation. For a short time step, the interaction may be considered constant. A set of updated positions and velocities to be predicted is proposed, at which point the new interaction are computed. At an important number of small time steps, the time behavior of the system can be calculated with good accuracy. Because of large phase space and short time steps, the simulation will only find the region close to the starting point, and several different simulations with different starting conditions are needed for estimating the stability of the results.

2.5. Non-bonded Interaction

The part of potential energy $u_{\text{non-bonded}}$, representing non-bonded interactions between atoms, is split into 1-body, 2-body and 3-body, etc. terms as:

(2.1)

$$U_{non-bonded} = \sum_i u(r - i) + \sum_i \sum_{j>i} \nu(r_i, r_j) + \cdots$$

The u(r) terms represent an applied potential field. Also, three body and higher order interactions are generally neglected to focus on the pair potential $\nu(r_i,r_j) = \nu(r_{ij})$. Some literature determines these potentials experimentally or theoretically [91-94]. The Lennard-Jones potential is the most commonly used form:

$$\nu^{LJ}(r) = 4\varepsilon[\left(\frac{\sigma}{r}\right)^{12} - \left(\frac{\sigma}{r}\right)^{6}] \quad (2.2)$$

where σ is the diameter, and ε is the potential well depth. This potential was used in the earliest analysis of the properties of liquid argon [95-96].

To express polar interactions, Coulomb potentials must be added via:

$$\nu^{coulomb}(r) = \frac{Q_1 Q_2}{4\pi\varepsilon_0 r} \quad (2.3)$$

where Q_1 and Q_2 are partial charges and ε_0 is the permittivity of free vacuum space.

2.6. Bonding Potentials

The interatomic interactions can be obtained [97] as:

$$U_{intermolecular} = \frac{1}{2}\sum_{bonds} k_{ij}^{r}\left(r_{ij} - r_{eq}\right)^2 + \frac{1}{2}\sum_{\substack{bends \\ angles}} k_{ijk}^{\theta}\left(\theta_{ijk} - \theta_{eq}\right)^2 + \frac{1}{2}\sum_{\substack{torsions \\ angles}}\sum_{m} k_{ijkl}^{\phi,m}\left(1 + cos\left(m\phi_{ijkl} - \gamma_m\right)\right) \quad (2.4)$$

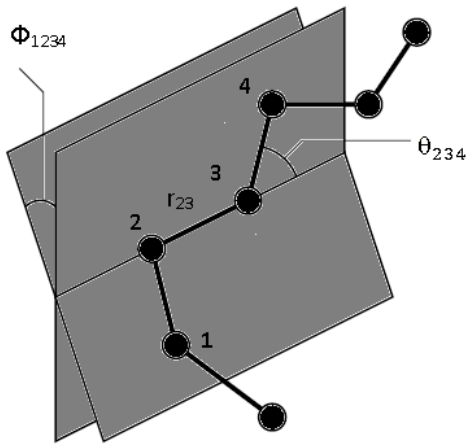

Figure 9. Geometry of a simple chain molecule illustrating the definition of interatomic distance r_{23}, bend angle θ_{234}, and torsion angle ϕ_{1234} [83]

The geometry of a simple chain molecule is presented in Figure 9. The bonds involve the separation $r_{ij} = r_i - r_j$ between adjacent atom pairs in Equation (2.4). The "bend angles" θ_{ijk} are between bond vectors such as $r_i - r_j$ and $r_j - r_k$ and involve three atom coordinates:

$$\cos \theta_{ijk} = \hat{r}_{ij} \,.\, \hat{r}_{jk} = (r_{ij} \,.\, r_{ij})^{-1/2} \, (r_{jk} \,.\, r_{jk})^{-1/2} \, (r_{ij}.r_{jk}) \qquad (2.5)$$

where $\hat{r} = \mathbf{r}/r$. The bending term is taken to be quadratic in the angular displacement from the equilibrium value, as in Eq.(2.4), although periodic functions are also used. The torsion angles ϕ_{ijkl} are defined in terms of three connected bonds, hence requiring four atomic coordinates:

$$\cos \phi_{ijkl} = - \hat{n}_{ijk} \,.\, \hat{n}_{jkl}, \text{ where } n_{ijk} = r_{ij} * r_{jk} \,,\, n_{jkl} = r_{jk} * r_{kl} \qquad (2.6)$$

where $\hat{n} = \mathbf{n}/n$ is the unit normal to the plane defined by each pair of bonds. Usually the torsional potential involves an expansion in periodic functions of order m = 1, 2, etc. as in Eq.(2.4).
The precise form of Eq.(2.4), the various strength parameters (k) and other constants therein will be specified with a simulation package. But Eq.(2.4) is highly oversimplified.

Molecular mechanics force fields predict structures and properties including many cross-terms (e.g. stretch-bend) like MM3 [98-100] and MM4 [101-103]. Some force fields, such as AMBER [104,105], CHARMM [106] and OPLS [107] are particularly used for larger molecules (proteins, polymers) in condensed phases. Their functional form is close to that of Eq.(2.4), and their parameters are determined by quantum chemical calculations.

2.7. Validation of Force Fields

The validity of the mathematical form of the energy expression and the accuracy of the parameters are two essential quantities, which can improve the quality of a force field calculation. If detailed forms for the individual interaction terms have been chosen, and a large body of experimental data is available to assign the parameters, the results of a calculation may be good enough as well.

Force field methods leads to mainly two properties: geometries and relative energies. In comparison with calculating energies, structural features are in general much easier to predict. Each structural feature depends only on a few parameters. For example, bond distances are essentially specified by R_0 and the corresponding force constant, bond angles by θ_0 (also a force constant and dihedral angle). The relative energies of different conformations are much more complicated while they are a consequence of many small contributions.

The non-bonded and torsional terms are the largest contribution to conformational energy differences. Therefore, it is crucial to have good representations of the whole torsional energy profile.

A given force field may be parameterized to reproduce rotational energy profiles for small molecules such as ethane and ethanol and contains a good description of hydrogen bonding between two ethanol molecules. But there is no guarantee that it would be completely successful in making the relative energies of different conformations of 1,2-dihydroxyethane [90].

It is inevitable that small inaccuracies in the functional forms for the energy terms and parameters will influence on the shape of the whole energy surface to the point where minima may disappear or become saddle points for large systems. Even for quite small systems, all force fields, no matter how the functional forms and parameterization are included, will have artificial minima and may fail to predict real minima.

2.8. The MD Algorithm

The most common molecular dynamics algorithm is the one of Verlet [108]. The principle is to integrate Newton's equation of motion. Nevertheless, in the last decade, a vast improvement in our understanding of numerical algorithms has been done. A review [109] and a book [110] summarize these attempts.

If a system composed of atoms with coordinates $r^N = (r_1, r_2, \dots r_N)$ and potential energy $U(r^N)$ is defined, the atomic momenta $p^N = (p_1, p_2, \dots, p_N)$ can be introduced in terms of the kinetic energy which may be written as: $K(p^N) = \frac{1}{2}\sum_{i=1}^{N}\frac{p_i^2}{m_i}$. So, the energy, or Hamiltonian, may be written as a sum of kinetic and potential terms H = K + U. The classical equations of motion are:

$$\dot{r}_i = \frac{p_i}{m_i} \quad \text{and} \quad \dot{p}_i = f_i \tag{2.7}$$

This is a system of coupled ordinary differential equations. Several methods can be used to carrying out their numerical integration, but these equations are not flexible. For example, the algorithm must manage both short and long timescales. Also, calculating the forces involves a summation over all pairs of atoms which is computationally expensive. It is better to perform them as infrequently as possible.

The time step should be as large as possible to ensure rapid sampling of the phase space. So, simulation algorithms have a tendency of being of low order allowing to increase the time step as much as possible without jeopardizing energy conservation.

2.9. The Velocity Verlet Algorithm

Different algorithms are available: Verlet [111], Leap-frog [112], velocity Verlet [113] and Beeman's [114]. It is important to determine which algorithm to apply and the following criteria can be used: The algorithm should conserve energy and momentum, it should be computationally efficient and it should enable a large time step for integration.

In next section, the Verlet and leap-frog algorithms are introduced. Here, the focus is on the "velocity Verlet" algorithm which may be written as [113]:

$$p_i\left(t+\frac{1}{2}\delta t\right) = p_i(t)+\frac{1}{2}\delta t f_i(t) \quad (2.8a)$$

$$r_i(t+\delta t) = r_i(t)+\frac{\delta t p_i(t+\frac{1}{2}\delta t)}{m_i} \quad (2.8b)$$

$$p_i(t+\delta t) = p_i\left(t+\frac{1}{2}\delta t\right)+\frac{1}{2}\delta t f_i(t+\delta t) \quad (2.8c)$$

After step (2.8b), a force evaluation is performed to give f_i $(t + \delta t)$ for step (2.8c). This scheme advances the coordinates and momenta over a time step δt.

2.10. Molecular Dynamics Methods

Nuclei are heavy enough that they act as classical particles and the dynamics can thus be simulated by solving Newton's second law of F = ma, which can be written in a differential form as:

$$-\frac{dV}{dr} = m\frac{d^2r}{dt^2} \quad (2.9)$$

where V is the potential energy at a position r. Force has a direction in space, so the vector r contains the coordinates for all the particles. In Cartesian coordinates, the vector is of length 3N atomic coordinates. The negative of the energy gradient on the left-hand side is the force (F) acting on the particle(s).

If there is a set of particles with positions r_i from Taylor expansion, the positions after small time step (Δt) are obtained as Eq.(2.10a,b). The velocities v_i are the first derivatives of the positions with respect to time (dr/dt) at time t_i, while the accelerations a_i are the second derivatives (d^2r/dt^2) at time t_i, and the hyper accelerations b_i are the third derivatives, etc. The previous positions of a small time step (Δt) are derived from Eq.(2.10b) by substituting (Δt) with (−Δt) and Eq.(2.10c) is obtained.

$$r_{i+1} = r_i + \frac{\partial r}{\partial t}(\Delta t) + \frac{1}{2}\frac{\partial^2 r}{\partial t^2}(\Delta t)^2 + \frac{1}{6}\frac{\partial^3 r}{\partial t^3}(\Delta t)^3 + ... \quad (2.10a)$$

$$r_{i+1} = r_i + v_i(\Delta t) + \frac{1}{2}a_i(\Delta t)^2 + \frac{1}{6}b_i(\Delta t)^3 + ... \quad (2.10b)$$

$$r_{i-1} = r_i - v_i (\Delta t) + \frac{1}{2} a_i (\Delta t)^2 - \frac{1}{6} b_i (\Delta t)^3 + \ldots \quad (2.10c)$$

Adding of Eqs.(2.10b) and (2.10c) leads to position prediction, a time step (Δt) later from the current and previous positions, and the current acceleration. The latter can be calculated from the force, or equivalently, the potential as:

$$r_{i+1} = (2r_i - r_{i-1}) + a_i (\Delta t)^2 + \ldots \quad (2.11a)$$

$$a_i = \frac{F_i}{m_i} = -\frac{1}{m_i}\frac{dV}{dr_i} \quad (2.11b)$$

Eq.(2.11a) is the Verlet algorithm for numerically solving Newton's equation and the term involving the change in acceleration (b) disappears. At the first point, the previous positions are not accessible, but can be predicted from a first-order approximation of Eq.(2.10b).

$$r_{-1} = r_0 - v_0 \Delta t \quad (2.11c)$$

At each time step, the acceleration must be calculated from the forces and Eq.(2.11b) allowing the atom positions to be followed in time and to get a trajectory.

The trajectory becomes a better approximation of the "true" trajectory by decreasing the step size (Δt) until the practical problems of finite numerical accuracy increases. Even though small time step means that more steps are needed to generate the system with a given total time, the computational effort inversely increases with the time step size.

But the Verlet algorithm has one numerical disadvantage. The new positions are obtained by adding a term proportional to Δt^2 to a difference in positions $(2r_i - r_{i-1})$. Since Δt is a small number and $(2r_i - r_{i-1})$ is a difference between two large numbers, this may result in some errors due to finite precision. For this reason, the leap-frog algorithm was developed because of the numerical aspect and the lack of explicit velocities in the Verlet algorithm [111]. Performing expansions analogous to Eqs.(2.10a,b and c) with a time step divided by two gives:

$$r_{i+1} = r_i + v_{i+1/2} \Delta t \quad (2.12a)$$

The velocity can be obtained by analogous expansions

$$v_{i+1/2} = v_{i-1/2} + a_i \Delta t \tag{2.12b}$$

Eqs.(2.12a) and (2.12b) represent the leap-frog algorithm. It is observed that the position and velocity updates are out of phase by half a time step. In terms of theoretical accuracy like the Verlet algorithm, it is also of third order, but the numerical accuracy is better. Moreover, the velocities appear directly which simplifies a coupling to an external heat bath.

2.11. Boundary Conditions

In a numerical simulation, a particular component of interest is selected for the simulation to limit the calculations size. The selected specific component is confined by a certain boundary with the surrounding environment (Figure 10). It is necessary to correctly choose the boundary conditions to prevent surface effect in a computational cell. This limitation involves smaller amounts of atoms in MD simulation systems in comparison with true systems. Different boundary conditions may result in different simulation results. Typically, boundary conditions can be decomposed in two groups: The Periodic Boundary Condition (PBC) and the Isolated Boundary Condition (IBC). However, it is possible to have mixed boundary conditions in which the system is characterized by PBC in some directions.

2.11.1. Periodic Boundary Condition

A realistic model of a solution has at least several hundred solvent molecules. To prevent the outer solvent molecules from dispersing and minimizing surface effects, periodic boundary conditions are normally used. The molecules are placed in a suitable box, often imposing a cubic geometry.

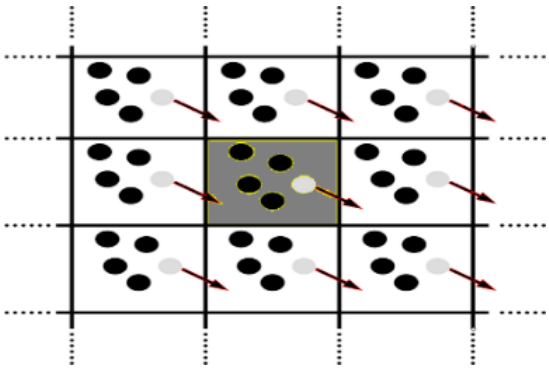

Figure 10. Schematic representation of a periodic boundary [115]

It has been reported that simulation results using any of the five types of space-filling polyhedra are equivalent (Figure 11) [115]. This box is then duplicated in all directions. For example, if the central box is surrounded by 26 identical cubes, it will be again be surrounded by 98 boxes, etc. If a molecule goes out from the central box through the right wall, its image will enter the box through the left wall from the neighboring box. This shows that the resulting solvent model becomes quasi-periodic, with a periodicity equal to the box dimensions.

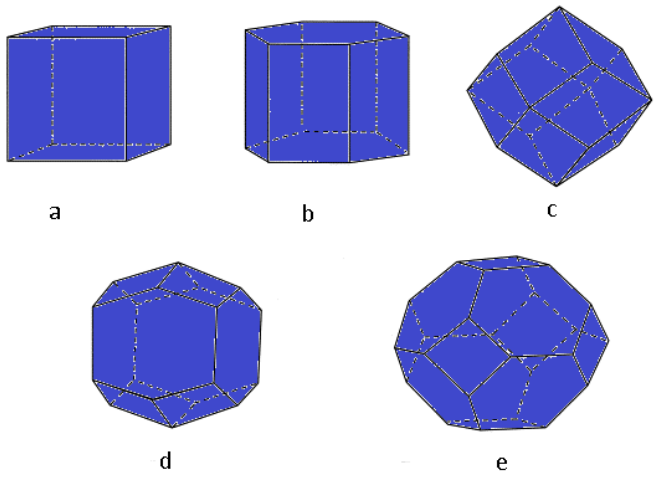

Figure 11. Five types of periodic boundary boxes: (a) the triclinic box, (b) the hexagonal prism, (c) the rhombic dodecahedron, (d) the elongated rhombic dodecahedron, and (e) the truncated octahedron [115]

2.11.2. Isolated Boundary Condition (IBC)

Occasionally, there is a problem to represent a virtually infinite system with a finite one. Simulating the melting of nanocrystals in a vacuum is complicated since the system surface cannot be represented by PBC. For these problems, IBC can be applied [116-119]. IBC is an appropriate method for systems such as clusters, crystals and molecules. The system is assumed to be surrounded by vacuum using this method. Furthermore, the interaction between the particles occurs just inside the system and particles cannot go out from this system. It is speculated that the particles inside the system have no interactions with those on the outside. It can be observed that these interactions may only apply to well-defined external forces.

2.12. Ewald Summation

The Ewald summation [120] is a technique used to compute the electrostatic interactions in systems with periodic boundary conditions. This method includes two parts: a short and long-range contributions. The short and long-range contributions are obtained from real (direct) space, and a reciprocal (Fourier transform) space, respectively. All point charges are naturally extended to Gaussian charge distributions, in Ewald summation [121]. The Gaussian distribution with an opposite sign, and with the same amplitude is added around each partial charge for short interactions. This method performs another Gaussian distribution eliminating the previous effect in the reciprocal space for the long-range contribution. So, it is used to cancel the background charge density. As shown in Figure 12, the original point charge distribution can be yielded by adding two spaces. This method leads to the rapid convergence of the energy compared to a direct summation.

2.13. Neighbor Lists

To calculate the non-bonded contribution to the interatomic forces in a MD simulation, a large number of pairwise calculations is involved. Each atom i is considered to loop over all other atoms j to calculate the minimum image separations r_{ij}. If the interaction potentials are assumed to be short range, $v(r_{ij}) = 0$ if $r_{ij} > r_{cut}$, as the potential cutoff, the program would skip the force calculation avoiding expensive calculations, and considers the next candidate j.

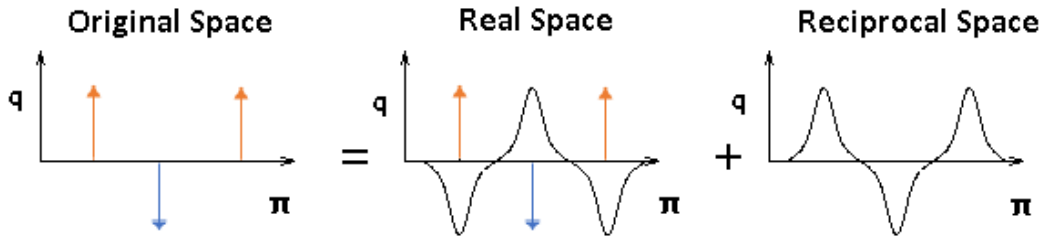

Figure 12. The method of Ewald summation for periodic potentials including the real, reciprocal and original spaces

Nevertheless, the time to examine all pair separations is proportional to the number of distinct pairs, $\frac{1}{2}$ N (N - 1) in a N-atom system, and for every pair one must compute at least r^2_{ij}. This still takes a lot of time.

Verlet [122] proposed a technique for improving the speed of a program by the use of lists of nearby pairs of atoms. Around a particular atom, the potential cutoff sphere of radius r_{cut} (full circle) is surrounded by a skin to give a larger sphere of radius r_{list} (dashed circle) as shown in Figure 13. To start the simulation, a list should be produced from all the atoms neighbors for which the pair separation is within r_{list}. Then, only pairs appearing in the list are included in the force routine.

2.14. Molecular Dynamics in Different Ensembles

In this section, a discussion about MD methods in the constant NVT ensemble (Nosé-Hoover algorithm) is made. However analogous approaches exist for other ensembles, particularly to simulate at constant pressure or stress. There are two main approaches to perform molecular dynamics at constant temperature rather than constant energy. The first one is to periodically reselect atomic velocities at random from the Maxwell-Boltzmann distribution [123]. It is like an occasional random coupling with a thermal bath.

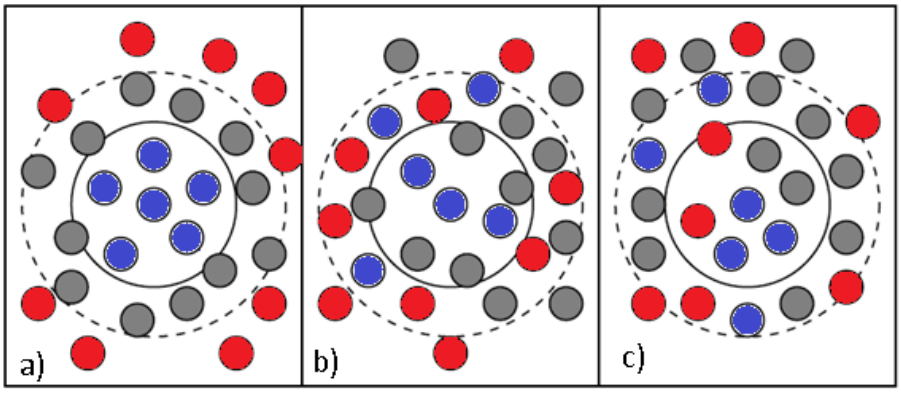

Figure 13. The potential cutoff range (solid circle) and the list range (dashed circle), are indicated (a). The list must be reconstructed before the particles originally outside the list range (red) have penetrated the potential cutoff range [89]

Introducing an extra thermal reservoir variable into the dynamical equations is the second approach [124,125]:

$$\dot{r}_i = \frac{p_i}{m} \tag{2.13a}$$

$$\dot{p}_i = f_i - \zeta p_i \tag{2.13b}$$

$$\dot{\zeta} = \frac{\sum_{i\alpha} p_{i\alpha}^2 - g k_B T}{Q} = \nu_T^2 \left[\frac{\sum_{i\alpha} p_{i\alpha}^2}{g k_B T} - 1\right] = \nu_T^2 \left[\frac{\Gamma}{T} - 1\right] \tag{2.13c}$$

where ζ is a friction coefficient which can vary with time, and Q is a thermal inertia parameter, which may be replaced by ν_T , a relaxation rate for thermal fluctuations. $g \approx 3N$ is the number of degrees of freedom. Γ represents the instantaneous temperature. The distribution function for the ensemble is proportional to $e^{-\beta W}$where $W = H + \frac{\frac{1}{2} 3 N k_B T \zeta^2}{\nu_T^2}$.

These equations follow in time variation of the system energy $H = \frac{\sum_{i\alpha} p_{i\alpha}^2}{2m} + u$ and for the variable w:

$$\dot{H} = \frac{\sum_{i\alpha} p_{i\alpha}^2 \dot{p}_{i\alpha}}{m} - \sum f_{i\alpha} \dot{r}_{i\alpha} = -\zeta \frac{\sum_{i\alpha} p_{i\alpha}^2}{m} \quad (2.14a)$$

$$\dot{W} = -3Nk_BT\zeta \quad (2.14b)$$

As a result, if Γ > T (the system is too hot), then the friction coefficient will increase and when it is positive, the system will begin to cool down. On the other hand, if the system is too cold, the friction coefficient may become negative leading to heat the system up again. In some conditions, this causes non-ergodic behavior, but this may be improved using chains of thermostat variables [126].

In NPT ensemble, where a constant pressure is kept, the Parrinello-Rahman dynamics [127] can be applied. According to this method, the simulation box can vary in shape as well as in size (volume) so that the internal pressure of the system can match the external pressure. The Hamiltonian function is extended by adding an external degree of freedom like Nosé-Hoover algorithm [128,129].

$$H = \frac{(P - P_{md})V(H^{-1})^T}{Q} \quad (2.15)$$

where P_{md} is the desired pressure, V is the volume, T presents the transpose, and Q is the fictitious cell mass. When Q is small, rapid box size oscillations occur, while a large Q imposes a slow volume adjustment.

2.15. Energy Minimization

After setting the MD simulation conditions, energy minimization should be carried out in our system. It can be performed using the steepest descent, conjugate gradients, or LBFGS (limited-memory Broyden-Fletcher-Goldfarb-Shanno quasi-Newtonian minimizer) [130].

2.15.1. Steepest Descent

Although the steepest descent is certainly not the best searching algorithm, it is strong and easy to implement. It is particularly adopted to the investigation of energetic optimization. The vector r can be specified by the vector of all 3N coordinates. At first a maximum displacement h_0 (e.g. 0.01 nm) must be given. So, the forces F and potential energy are calculated. New positions can be calculated by:

$$r_{n+1} = r_n + \frac{F_n}{\max(F_n)} h_n \qquad (2.16)$$

where h_n is the maximum displacement and F_n is the force, or the negative gradient of the potential V. The notation max ($|F_n|$) presents the largest of the absolute values of the force components. The forces and energy will be again computed for the new positions. When ($V_{n+1} < V_n$), the new positions are accepted and $h_{n+1} = 1.2h_n$. If ($V_{n+1} \geq V_n$), the new positions are rejected and $h_n = 0.2h_n$.

The algorithm stops when two conditions are met: if either a user-specified number of force evaluations has been performed (e.g. 100), or when the maximum of the absolute values of the force (gradient) components is smaller than a given value (ε). The stopping criterion should not be considered too tight to avoid endless iterations because force truncation produces some noise in the energy evaluation. A specified value for ε can be estimated from the root mean square force (f) which a harmonic oscillator would exhibit at a temperature T. This value is:

$$f = 2\pi\nu\sqrt{2m\kappa_B T} \qquad (2.17)$$

where ν is the oscillator frequency, m the (reduced) mass, and κ_B the Boltzmann's constant. As an example, for a weak oscillator with a wave number of 100 cm^{-1} and a mass of 10 atomic units, at a temperature of 1 K, f = 7.7 kJ mol^{-1} nm^{-1}. A value for ε between 1 and 10 kJ mol^{-1} nm^{-1} is acceptable. In SD method, the previous step is not taken in to account.

2.15.2. Conjugate Gradient

In the initial stages of the minimization, conjugate gradient is slower than the steepest descent, but becomes more practical closer to the energy minimum. The parameters and stop criterion are the same as the steepest descent. As an example, in the GROMACS package [131], conjugate gradient cannot be performed with constraints, including the SETTLE algorithm for water [132]. This is not really a restriction, because conjugate gradient is only used for minimization before normal mode analysis, which is performed without constraints. For the other purposes, the steepest descent is efficient enough to be performed.

2.15.3. L-BFGS

The original BFGS algorithm leads to better approximations of the inverse Hessian matrix and moves the system to the currently estimated minimum. So, it is proportional to the square of the number of particles, and not practical for large systems like biomolecules. Instead, the L-BFGS algorithm of Nocedal [130,133] is used which approximates the inverse Hessian by a fixed number of corrections from previous steps.

2.16. Cell Construction

Many efforts have been made to produce amorphous polymer cells in simple atomistic models. In 1985, Theodorou and Suter simulated the glassy polymer structure [134]. They modified the Rotational Isomeric States (RIS) model to generate the polymer chains [134], and the idea of this model stems from “Flory’s Hypothesis” [135]. This hypothesis states that a polymer chain in melt behaves like a random-walk model. This means that the backbone angles of one segment are not dependent of those of the previous or next segments. The random-walk model allows the chain to retrace its steps [Figure 14]. Hence, many of the pieces can have the same place in space which is impossible. According to the “principle of excluded volume”, two molecules cannot be in one place at the same time. If two molecules come close to each other, there is steric repulsion between them. The RIS model was introduced by Flory to solve the problem of the random-walk with excluded volume (also called the self-avoiding walk or SAW) [135]. According to the RIS method, we are able to describe the conformational behavior of macromolecules in accordance with the chemical structure of the chain configuration.

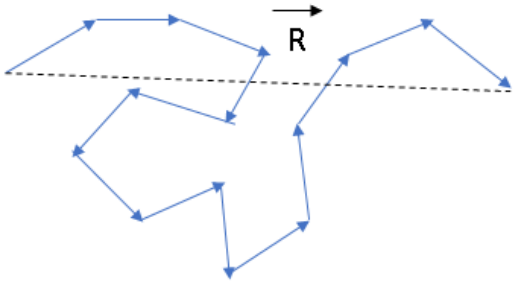

Figure14. Random-walk of a polymer chain.

The rotational isomeric state of each added monomer is selected with a probability involved in its conformational energy. If N+1 monomers in the chain are considered, then there will be N+1 position vectors: R_0, R_1, R_2, …, R_N and N-1 bond vectors: $r_0 = R_1 - R_0$, $r_1 = \cdots = R_N - R_{N-1}$, and N-2 dihedral angles: φ_0, φ_1, φ_2, …, φ_{N-1}

Then the energy of a polymer as a function of the angles φ is calculated as:

$$E = \sum_{i=2}^{N-1} \varepsilon_1(\varphi_i) \tag{2.18}$$

If one considers the sequence $\varphi_i = G^+$, then it can be shown that $\varphi_{i+1} = G^-$. This leads the monomers i-2 and i+2 to be in the same position. This phenomenon is termed as the "pentane effect''and brings a larger positive contribution to the energy. In order to consider the pentane effect, the corrected energy of a polymer as a function of the angles φ:

$$E = \sum_{i=2}^{N-1} \varepsilon_1(\varphi_i) + \sum_{i=3}^{N-1} \varepsilon_2(\varphi_{i-1}, \varphi_i) \tag{2.19}$$

The growing chain contour re-enters from the opposite side of the unit cell (in PBC) when it exits from a unit cell. The density of the system is determined by cell dimensions. The Amorphous Cell code, is the combination of the algorithm developed by Theodorou and Suter and the scanning method. Meirovitch [136] proposed the scanning method. Through this method, a self-avoiding walk is generated by step-by-step construction and each movement is specified by scanning all possible different chain continuations in future steps.

In Figure 15, the possibility of three more next segments after the last added segment will be four: one on the left side and the three others should be above. So, the probability to move segments in an upward direction would be 0.75, which is more accurate comparing to Monte-Carlo method. In Monte-Carlo method, the probability of the next segment to be placed upward or left is 0.5.

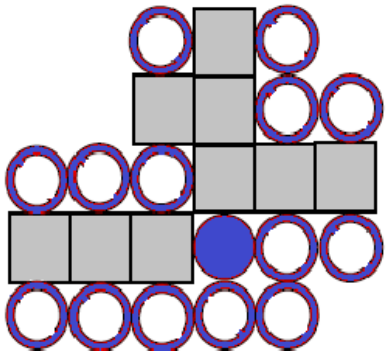

Figure 15. Simple example of a scanning procedure. A filled circle presents the last segment added, empty circles are occupied space, and a square represents the free space.

2.17. Making the Configuration (PE Nanocrystal embedded in Amorphous Phase)

Our system includes alkane chains nanocrystal embedded in an amorphous phase. Hence, at first, the alkane chains nanocrystal should be generated. X-ray diffraction technique enables us to get information about the dimensions of the polyethylene configuration cell. Through powder diffractometry and the Rietveld method, standard deviation of the fractional coordinates and refined hydrogen atom coordinates have been performed. According to Caminiti [137], through constant wavelength (CW) X-ray powder diffraction and the Rietveld method [138], a sample of commercial semi-crystalline polyethylene (PE), with a Mw of 300,000 g/mole and an estimated crystallinity of 73%, was structurally studied.

The space group for this structure is Pnam and the cell parameters are: a = 7.424 Å, b = 4.949 Å and c = 2.553 Å. The refinement shows a C−C bond distance of 1.53 Å.

The Materials Studio environment was first used to generate the orthorhombic cell of crystalline polyethylene. Each unit cell consists of 2 PE chain segments, each one includes 2 carbon atoms. This is next placed in a three-dimensional (3D) cell and considers a periodic box in which all

subsequent calculations are performed. The linear alkane chains are constituted of N carbon atoms with no connection between them. They are terminated by a methyl group to preserve the system neutrality. A nomenclature where the number of replica of crystals along the x and y directions are indicated: *nam*bN indicates that the lengths of the nanocrystal edges are *n* and *m* times a and b, respectively. As an example, to simulate a system including 12 chains with 8 carbon atoms on each chain, the unit cell should be displaced by 2*3*4 times in the x, y, and z directions, respectively. It thus indicates that this nanocrystal contains $\left[(n+1)(m+1)+nm\right]$ chains with 7.4241n and 4.9491m Å lateral edge lengths, while the chain length is 2.5534 (N/2) Å.

These nanocrystals are then set in an environment constituted of alkane chains. A total of 52 chains with 30 carbons length were considered as a good compromise to reveal an amorphous environment to the nanocrystals (Figure 16). Number of chain segments and carbon atoms in the amorphous phase were selected by specifying the density and acceptable energy of the system. Repulsion of alkane chains in the amorphous phase influences on this energy tolerated by the system. The dimension of the simulation box is 50∗50∗50 Å which was constant for all simulations varying only the nanocrystal dimensions. The simulations were carried out in the canonical statistical ensemble (constant number of particles, volume and temperature (NVT)). The Nosé-Hoover algorithm was used to keep the temperature constant [124, 125]. The cut-off radius for short-range intermolecular interactions was 10 Å. The cut-off of the non-bonded interactions has been done using the Ewald summation method [120]. The equation of motion was integrated using the velocity-Verlet algorithm with an integration time step of 1 fs [113]. MD simulations were performed using the open source LAMMPS package [139] with the second generation force field, *pcff* [140]. Prior to any simulation to determine the melting point, the amorphous environment surrounding the nanocrystals must be properly relaxed. Based on the established procedure from our lab, a protocol has been followed.

During all the relaxation procedure, the molecules in the crystal are fixed to prevent any deformation altering the final value of T_m. Once the disordered chains are placed around the crystals, a short molecular dynamics (MD) simulation is carried out to alleviate any endemic stress after the initial construction. It is followed by a classical energy minimization using the Polak-Ribiere version of the conjugate gradient algorithm [141].

Table 2. Configuration and nanocrystals chain numbers

Model	Number of chains
3a3bN	18
4a4bN	32
6a4bN	48
8a8bN	128
10a6bN	120

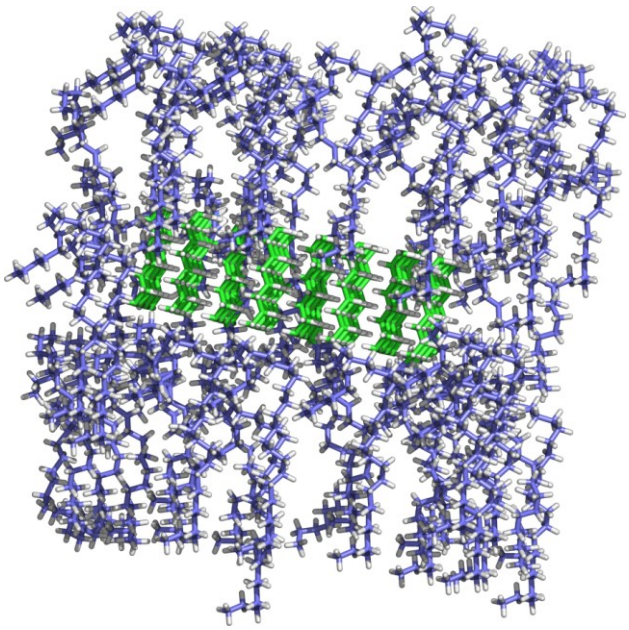

Figure 16. Representation of a polyethylene nanocrystal embedded in alkane chains (amorphous phase)

We can be sure that mechanical equilibrium is reached in the initial configuration. MD simulation can then be carried out to determine the value of the melting point: MD simulation of 500 ps at

temperatures ranging from 260 to 620 K with 5 K increments are performed. At each temperature, the same structure equilibrated configuration is used.

2.18. Hydrostatic Uniform Compression

Hydrostatic uniform compression makes a simple and appropriate tool to ascertain the structure with minimum energy and mechanical equilibrium in a polymer system. This process is applied after minimization and relaxation procedures and includes two stages. In the first step, the initial cell compression is performed uniformly with variation steps of the cell edge of 0.1 Å with the energetic convergence equal to 10 kcal/mol. After achieving the minimum energy, the optimization is refined and in the next stage, a step of 0.001 Å is then used with an energetic convergence of 0.1 kcal/mol.

2.19. Melting Simulation

To define the melting temperature (Tm), the midpoint temperature was found between the temperatures separating the jump in the potential energy as shown in Figure 17a. An abrupt variation of the intermolecular potential energy represents the crystal to the liquid state transition. To confirm this point, the occurrence of a peak in the heat capacity (stemmed from the graph of energy versus temperature) and change in the amount of the trans-rotameric state at the same transition temperature was verified as shown in Figure 17b,c for the 4a4b3c configuration. This procedure was then applied to the various cells (reported in Chapter V) to get all the Tm values.

2.20. Errors and Uncertainty in MD Simulation

After the creation of the cell, simulation can start. Nevertheless, like any experiments in a laboratory, MD simulation leads to statistical and systematic errors. The origins of statistical error are related to the values resulting from the simulation being averaged in time and space. When an irrational number is represented by using a finite number of decimal digits, statistical errors such as round-off error may happen. If higher-order terms in a functional series (such as Taylor series) are neglected, truncation errors happen [142]. Also, systematic errors associated with other factors like finite-size effects, interaction cutoff, etc. are present. These are some intrinsic parts of

computational experiments. Systematic errors are directly linked to the algorithms and the approximations which have been used to represent the system like the force field, the initial configurations, the Nosé-Hoover thermostat and the Parrinello-Rahman barostat. The best way to minimize errors in the laboratory is trying to use the best instruments and the most appropriate method for the type of measurement. In MD simulation, the most efficient algorithms must be used with proper approximations, as well as rigorous methods to select the variables during a simulation.

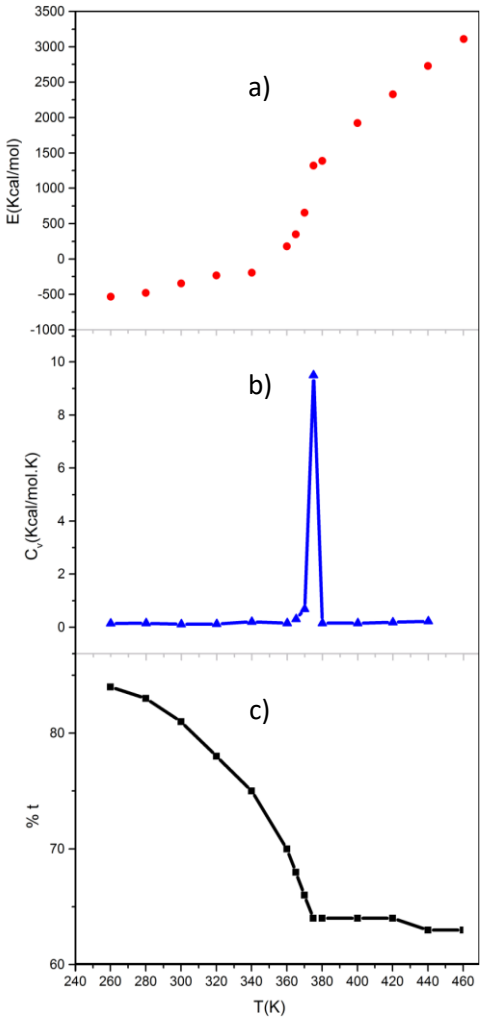

Figure17. Determination of the melting temperature by MD for the crystal 4a4b3c embedded in an amorphous phase (duration 500 ps). (a) Potential energies, (b) heat capacity at constant volume with respect to temperature, and (c) trans-rotameric state

CHAPTER III. Review of Molding Methods and Effect of Processing Conditions on the Thermal and Mechanical Properties of Polymers

3.1. Introduction

Injection and compression molding are two essential methods to produce molded materials. In this chapter, the mechanical and thermal properties of polymers are explained in relation with their molding conditions. In particular, the effect of pressure, temperature and cooling rate on the mechanical and thermal behavior of polymers are reviewed.

3.2. Types of Plastics

The physical properties of plastic materials are divided into different categories based on the macromolecular structure and the temperature dependence of these complex materials. Figure 18 presents an overview of these types of plastics. Thermoplastics are hard with limited elasticity depending on the energy input (mechanical, thermal or radiation energy) which can melt them. On the other hand, elastomers are soft and very elastic but usually cannot be melted. Thermosets are usually very hard with low elasticity and cannot be melted [143].

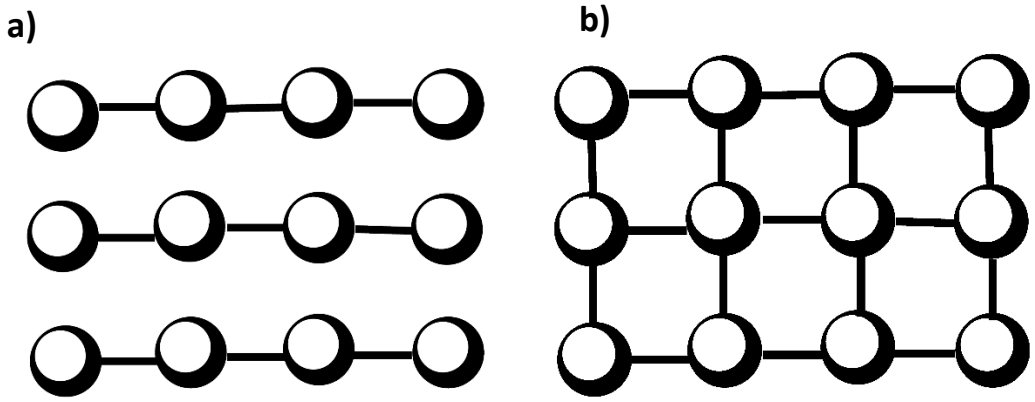

Figure 18. Schematic representation of: a) thermoplastic structure and b) thermoset structure

3.3. Molds

Molds are associated to the tools used to produce plastic parts in molding. They make the final shape of the part. Molds are used in mass production because they can be expensive to manufacture. Hardened steel, heat-treated steel, aluminum, and/or beryllium-copper alloy are used to build typical molds. It is important to choose the right material to build a mold as it is one of the main part controlling the economics of a production line. Steel molds are generally more costly to build but last longer. CNC (Computer numerical control) machining or electrical discharge machining are the main manufacturing processes [144].

3.3.1 Injection Molding

Thermoplastic and thermoset polymers can be produced via injection molding. For thermoplastics, the resin is melted in the injection molding machine barrel and then forced into the mold under high pressure. It is then cooled and solidified into the final part before being ejected. A similar process is used for thermosets, but the mold is usually preheated to form a solid part via curing/crosslinking [145]. To force the material into the mold cavity, a ram or screw type plunger is used.

A thermoplastic polymer when heated and subjected to excessive input of mechanical energy, such as external forces, degrades into a polymer having a lower molecular weight. This is more important when high shear is applied (high speed) in extrusion and injection molding. To produce the desired product with a molecular weight, correspond to a given set of properties for the polymer, the molding process must start with a higher molecular weight which can be more costly (raw material) and more difficult to process (higher viscosity and elasticity). Also, differences between the processing conditions make it difficult to accurately predict the resulting degradation level [146].

Some advantages of injection molding are [146]: A wide range of material are appropriate for this method, the processing cost per part is low, high tolerances can be obtained with repeatability and minimum scrap losses. Although the cost of processing samples is low, the equipment itself may be quite high (machine and mold).

3.3.2 Compression Molding

Compression molding is a simple method placing an accurately measured amount of the polymer resin into a mold cavity. It is then compressed under pressure into the mold shape specified by the cavity at a temperature (usually below injection molding) above the melting point of the thermoplastics being processed. Compression molding is the most used molding technology for highly viscous materials, especially for fiber reinforced composites [147].

Compression molding is also commonly performed on thermosetting resins placed into the mold in the form of powders or tablets. This process uses thermosetting resins in a partially cured stage, in the forms of granules, or paste-like masses [147]. It was observed that for thermoplastics materials, the same could be done, but leads to much higher costs due to the need to heat, shape and cool them. Nevertheless, much lower shear is applied than for injection molding leading to lower material degradation (less molecular weight reduction). Some advantages of compression molding are [148]: the ability to mold large and complex parts, lower molding costs, especially for thermoset materials in comparison with other methods like transfer molding and injection molding, and it is appropriate for ultra-large-size basic shape production. Some disadvantages are: poor product consistency (difficult to control flashing), has fewer knit lines and smaller amount of fiber-length degradation.

In this work, compression molding was used to manufacture polyethylene samples to study the effect of mold temperature, pressure and cooling rate on their properties. In this case, there is no minimum cost to heat, shape and cool the samples. It is also easy to mold polyethylene and control its final properties by careful selection of the processing conditions.

There are six important factors to be considered in compression molding:

1. Choosing the proper amount of raw material,
2. Finding the best method to have the minimum amount of energy required to heat the material,
3. Determining the minimum time required to heat the material,
4. Finding the appropriate heating technique,
5. Determining the required force to ensure to completely fill the mold,
6. Forming the part via rapid cooling after the material has been compressed into the mold [136].

3.4. Mechanical Properties of Polymers

Polymers are viscoelastic materials by having the possibility to flow like liquids (viscous) and be solid (elastic) in their behaviors. An ideal linear elastic solid obeys Hooke's law (stress being proportional to strain), while an ideal viscous liquid obeys Newton's law, (stress being proportional to the rate of strain) [149]. This duality is the materials increase their complexity as both properties must be determined for a complete understanding of their behavior.

3.4.1. Elasticity

The main differences can be seen by using stress-strain curves under controlled conditions (pressure, temperature, rates, etc.).

3.4.2. Strength

The strength is usually the stress needed to break the sample (strength at break). But other definitions are possible depending on the type of deformation applied: tension (stretching of the polymer), compression (compressing the polymer), flexion (bending of the polymer), torsion (twisting of the polymer), impact (hammering) and so on. The order of increasing strength for polymers is: linear < branched < crosslinked < network [150].

3.4.2.1. Factors Affecting the Strength of Polymers

Crystallinity: The crystallinity increases the strength because in the crystalline phase, the intermolecular bonding interaction is stronger. The density is also higher leading to lower free volume and higher amount of material to sustain the applies stresses. But polymers under deformation have a tendency to get more oriented chains leading to a phenomenon called stress/strain induced crystallization also improving the polymer mechanical properties [151].

Cross-linking: The motion of polymer chains can be restricted by crosslinking which increases the amount of stress/energy to deform the polymer.

Molecular Weight: The tensile strength of polymers increases with increasing molecular weight up to a "saturation level" or plateau is reached at some critical molecular weight.

3.4.3. Elongation to Break (Ultimate Elongation)

This property represents the strain necessary to break the sample as shown in Figure 19. It represents the relative length change in the material compare to its initial value and is a good measure of ductility. Ceramics have very low values (<1%), while metals have moderate ones (1–50%) and thermoplastics (>100%) and thermosets (<5%) have a wide range of elongation at break [151].

3.4.4. Young's Modulus (Modulus of Elasticity or Tensile Modulus)

Young's Modulus represents the ratio of stress over strain in the linear elastic region (low deformation) where the stress is proportional to strain (Figure 20). The elastic modulus is a direct measure of the material stiffness via:

$$E = \frac{Tensile\ stress\ (\sigma)}{Tensile\ strain(\varepsilon)} \tag{3.1}$$

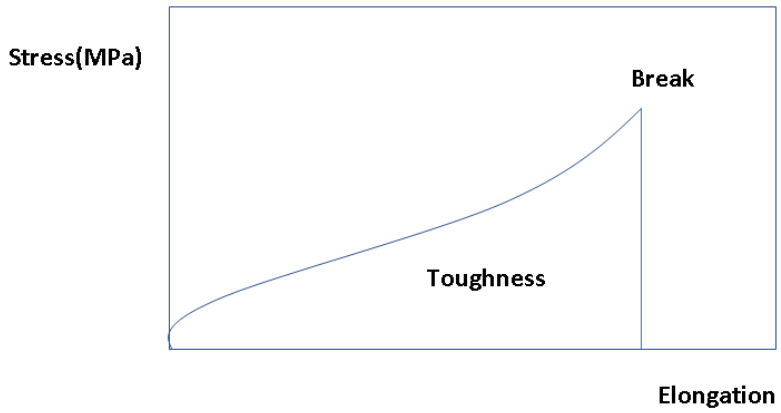

Figure 19. Representation of the elongation at break and toughness

3.4.5. Toughness

The toughness of a material is measured by the area under a stress-strain curve:

$$\text{Toughness} = \int \sigma d\varepsilon \tag{3.2}$$

The toughness represents the energy absorbed by the material before it breaks. A typical stress-strain curve is shown in Figure 21.

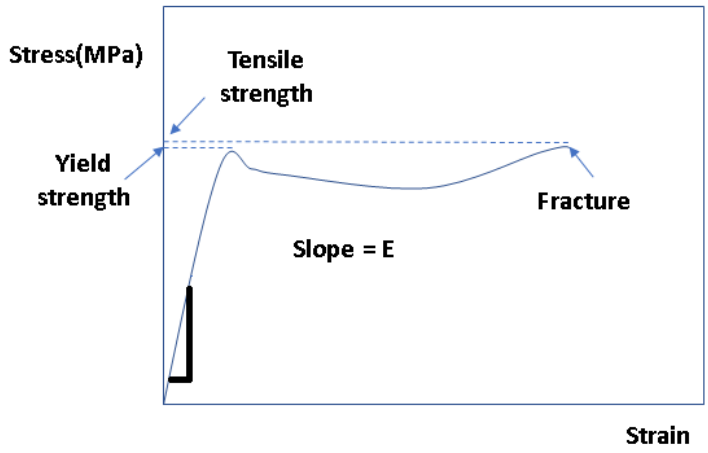

Figure 20. Typical stress-strain curve to calculate the mechanical properties

Even though rigid materials have high Young's modulus such as brittle polymers, ductile polymers have similar elastic modulus, but with higher fracture toughness due to their high deformation before rupture. On the other hand, elastomers have low Young's modulus, but have very high deformation due to their rubbery nature [152].

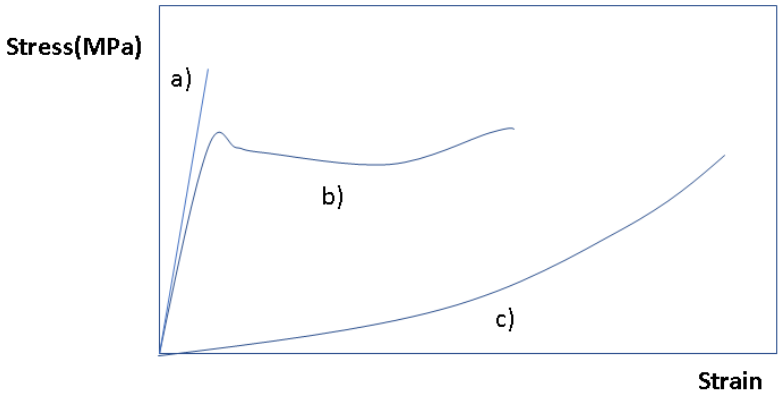

Figure 21. Stress-strain behavior of different materials: a) brittle polymer (glassy polymer/low temperature thermoset), b) ductile polymer (semi-crystalline polymer/plastic/elevated temperature thermoplastic), and c) highly elastic (elastomer)

Where the elastic region (linear portion of the curve) ends, this region is associated to the yield strength. Some materials have higher yield strength than strength at break (Figure 20).

3.5. Melting Point and Glass Transition Temperature of Polymers

Polymer molecules in the amorphous region at lower temperature are in a frozen state, but still vibrate. This state is named the glassy state where the polymer is brittle, hard and rigid as glass. The glassy state is metastable as a supercooled liquid where the molecular movement is in the frozen state (or a molecular disorder as a liquid).

When the polymer is annealed, the polymer chains are able to slide around each other and the polymer becomes soft and flexible similar to a rubber. This state is called the rubbery state [153]. The glass transition is the temperature where the transition from the glassy to the rubbery state occurs.

Although the glass transition temperature is the property of the amorphous region, the crystalline region is characterized by the melting point. In thermodynamics, transitions are classified as first and second order transitions. The glass transition temperature is a second order transition at extremely low cooling rate, while the melting point is a first order transition. The value of the glass transition temperature is not exclusive because the glassy state is not in equilibrium. It is determined by several factors such as molecular weight, measurement method, and rate of heating or cooling (Figure 22) [154].

Semi-crystalline polymers have both transitions corresponding to their crystalline and amorphous regions. Hence, they have precise melting temperatures (T_m) at which the ordered phase changes to a disordered one. However, as explained above, the amorphous regions soften at the glass transition (T_g). It should be mentioned that pure amorphous polymers do not have a melting point, but quite all polymers have a glass transition temperature. The polymer melting point (T_m) is higher if double bonds, aromatic groups, bulky or large side groups are present in the polymer structure because they decrease the chain flexibility. Since defects are created by branching (side chains), the melting point is decreased.

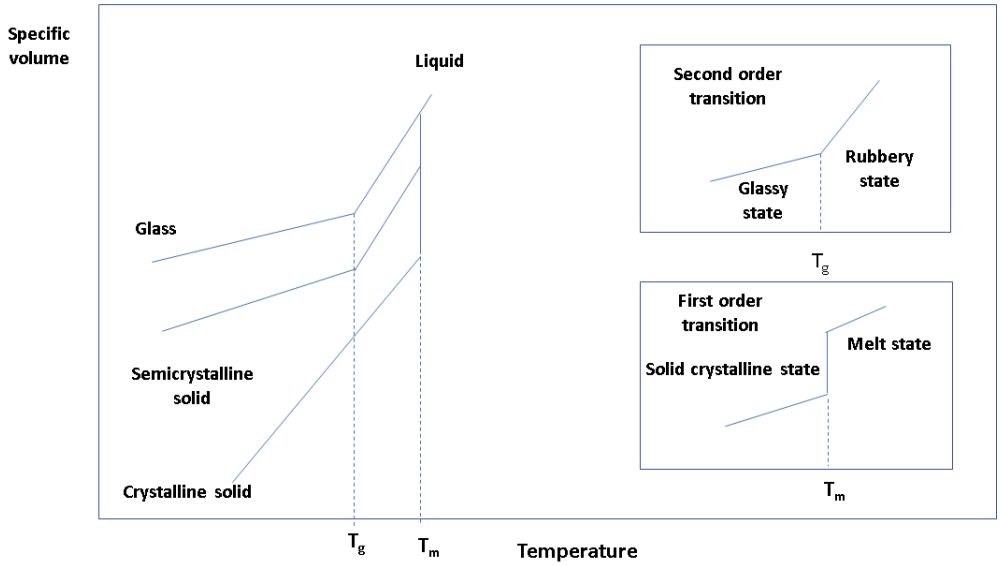

Figure 22. Melting point and glass transition of polymers

3.6. Polymer Crystallinity: Crystalline and Amorphous Polymers

As explained in chapter I, the very large polymeric chains found in polymers are in two forms: lamellar crystalline shape in which the chains fold and produce lamellar structure arranged in the regular manner (order), and amorphous shape in which the chains are in an irregular distribution (disorder). The amount of crystallinity is measured by [151, 152]:

$$\text{Crystallinity} = \frac{\rho_c\,(\rho_s - \rho_a)}{\rho_s\,(\rho_c - \rho_a)} \tag{3.3}$$

where

ρ_c = density of fully crystalline polymer

ρ_a = density of the fully amorphous polymer

ρ_s = density of the sample

A typical range of crystallinity can be specified by amorphous (0%) to highly crystalline (>90%). As linear chains, polymers have simple structural chains and slow cooling rate will lead to high crystallinity. When the cooling is slow, sufficient time is given for crystallization to take place.

Polymers with high degree of crystallinity are rigid and have high melting point. However, their impact resistance is low. Amorphous polymers are soft and have lower melting points. A solvent can penetrate the amorphous part more easily than the crystalline part.

3.7. Surface Tension of Polymers

Interfacial and surface tensions of polymers are essential in producing plastics, coatings, textiles, films, and adhesives through their roles in phenomenon like wetting, adsorption, and adhesion. Because of experimental difficulty, they are seldom studied [7].

In general, surface tension decreases with increasing pressure which can be explained by the decrease in the Gibbs free energy during crystallization at high pressure in comparison with ambient conditions [7]. Surface tension (γ) represents the change in Gibbs free energy (G) with respect to surface area (A) at constant temperature (T) and pressure (P) as:

$$\gamma = \left(\frac{\partial \mathrm{G}}{\partial \mathrm{A}}\right)_{T,P} \tag{3.4}$$

3.8. Experimental Work

LDPE Novapol LA-0224-A (Nova Chemicals, Canada) was used as the matrix. This polymer has a melting temperature of 111 °C, a density of 923 kg/m^3 and a melt flow index of 2.3 g/10 min. This polymer was selected to perform the experimental work and validate the simulation results.

The samples were produced via compression molding (Carver hot press). A specific amount (225.1 g) was placed inside an aluminum mold having dimensions of 255 x 225 x 3 mm^3. At first, the temperature was set at 135 °C, 150 °C and 165 °C, while a constant plate pressure (3 MPa) was applied (Table 3, samples 1-3). As a second step, samples at constant temperature (150 °C) were molded at different pressures (11, 17, 22 and 28 MPa) (Table 3, samples 4-7). To study the effect of cooling rate, samples were also produced at two temperatures (150 °C or 165 °C) and constant pressure (3 MPa) using 50%, 8.3 °C min^{-1}, (half of the cooling water flow rate) and 0%, 0.14 °C min^{-1}, (no water flow rate) cooling rate (Table 3, samples 8-11). The last step consisted in producing asymmetric samples by imposing a temperature gradient using different temperatures for the upper (T_u) and bottom (T_b) plates of the mold (Table 3, samples 12-17). These asymmetric samples were produced to compare and to determine the effect of molding temperature profile on

the mechanical and thermal properties. For symmetric samples, the temperature of the upper (T_u) and bottom (T_b) plates of the compression molding press were set at the same temperature, while different temperatures were imposed for asymmetric samples. The molding cycle was: 8 min of pre-heating without pressure, 6 min of applied pressure and 8 min of cooling by water circulation to 25 °C before demolding.

Table 3. Sample codes and molding conditions to produce the samples

Sample	Molding temperature (°C)	Pressure (MPa)	Cooling Rate (°C min^{-1})
1	135	3	15.6
2	150	3	15.6
3	165	3	15.6
4	150	11	15.6
5	150	17	15.6
6	150	22	15.6
7	150	28	15.6
8	150	3	8.3
9	150	3	0.14
10	165	3	8.3
11	165	3	0.14
12	T_u = 150 T_b = 165	3	15.6
13	T_u = 150 T_b = 135	3	15.6
14	T_u = 135 T_b = 165	3	15.6
15	T_u = 135 T_b = 150	3	15.6
16	T_u = 165 T_b = 135	3	15.6
17	T_u = 165 T_b = 150	3	15.6

From the sample produced, different characterizations have been carried out. Differential scanning calorimetry (DSC) measurements were used to determine the melting point and the melting enthalpy. Samples were prepared in order to avoid any surface defect. Nevertheless, the first two layers that are cut from the plates were not taken into account to remove edge effects. It is the third layer that has been considered as the core. For each condition, two measurements have been carried out to check for data reproducibility and get average values with standard deviations. For the asymmetric temperature profile, the samples prepared for DSC analysis were also cut from the

cores to remove the effect of temperature on the surfaces and focus on the temperature gradient in the cores. Around 10 mg was placed inside aluminum pans and calibration was performed using indium as a standard for the selected heating rate. The thermogrammes were acquired at a heating rate of 10 °C/min over a range of 25-150 °C under a nitrogen atmosphere using a Mettler DSC 7. Because of calibration performed, even the small trends observed are significant. The heats of melting (ΔH_m) have been measured by integrating the areas (J/g) under the peaks, while the crystallinity (χ) was calculated as:

$$\chi = \left(\frac{\Delta \mathrm{Hexp}}{\Delta \mathrm{H}^\circ}\right) * 100 \quad (3.5)$$

where ΔH_{exp} is the heat of fusion of the samples obtained from the DSC results and $\Delta H°$ is the heat of fusion for 100% crystalline LDPE which is 290 J/g [155].

XRD data were obtained under the following conditions. Samples 1 to 11 of approximately 0.4 mm diameter were glued with silicone on the goniometer head tip and mounted at room temperature on a Bruker APEX DUO X-Ray diffractometer. A total of 6 correlated runs with Phi Scan of 360 degrees and exposure times of 180 seconds were collected with the Cu micro-focus anode (1.54184 Å) and the CCD APEX II detector at 150 mm of distance. These runs, from -12 to -72 2-theta and 6 to 36 omega were then treated and integrated with the XRW2 Eval Bruker software to produce WAXD diffraction pattern from 3 to 82 degrees 2-theta. The pattern was treated with the Diffrac.Eva version 2.0 from Bruker.

The tensile modulus was determined according to ASTM D638 (type V). The samples were directly cut in the molded plates after 24 h. An Instron model 5565 mechanical tester was used to perform the measurements at a rate of 2 mm/min and room temperature (23 °C) with a 500 N load cell. The tensile modulus was extracted from the slope of the linear part in the stress-strain curve (low deformation). A total of 5 measurements was performed to get an average and standard deviation.

The flexural modulus was measured on a Zwick/Roell Proline Z050. Testing was performed according to ASTM D790 using a 30 N load cell. The samples (75 mm in length, 10.2 mm in width and 3.5 mm in thickness) were directly cut in the molded plates. A three point bending fixture (60 mm span) was used to do measurements at a rate of 1.5 mm/min and room temperature (24 °C). The load was applied on both sides of the sample to detect any significant difference in flexural behavior; i.e. the load was directed applied on the face that was in contact with the bottom (E_b) or

the upper (E_u) plate of the compression mold to detect any significant difference, especially for asymmetric samples.

Finally, surface tension of the samples produced under different molding pressure was measured according to the Wilhelmy plate method on a DCA-100 contact angle tensiometer [156]. The samples were cut by a microtome LEICA SM2500 with the same width and layer thickness: 3.2 and 2.5 mm. Surface tension was calculated according to the force, contact angle and wetted perimeter of the sample in one polar (water) and one nonpolar (n-hexane) liquid with 5 mm immersion depth and 0.2 mm/s approach speed.

In the following section, the effect of pressure, temperature and cooling rate on the mechanical and thermal behavior of polymers is reviewed.

3.9. The Effect of Hydrostatic Pressure on Mechanical Properties of Polymers

A number of recent publications focused on the mechanical properties of several polymers as a function of the hydrostatic component of stress [157-162]. Increases in stiffness and yield stress with increasing the pressure were reported in poly (methyl methacrylate) [157-159], polypropylene [160], polystyrene [161] and other polymer systems [157-162]. An increase in the stress and strain at break as a result of higher hydrostatic stress was observed for poly (methyl methacrylate) [157] and polystyrene [157,162,163] for uniaxial tension and compression. Differences in the fracture type was also reported at higher pressures. These evidences indicate that any general theory for yield or fracture must include a pressure dependence. However, studies on the mechanical behavior of polymers under high pressure are still at an early stage. According to Rabinowitz [164], there is a monotonic increase in the initial slope of the PMMA stress-strain curve with increasing pressure. Then, as pressure is further increased, a substantial increase in the yield stress and strain were observed. Furthermore, at elevated pressure, a transition in the failure mode was observed and a direct relation between fracture stress and pressure was noted. On the other hand, the strain at break was found to decrease.

Some data show that the resistance of polymers to deformation and failure is a function of hydrostatic pressure and this dependence is more important than for metals. An increase in Young's modulus with increasing hydrostatic pressure might apparently result from three effects:

1) a variation in interatomic distance, while the interaction forces between atoms become more nonlinear as the distance between them decreases.
2) a decrease in specific volume.
3) the finiteness of deformation: at the yield point the deformation is about 10-15% for thermoplastic, while it is 2-3% for thermosetting materials [165].

3.10. Melting of Polymers under high Pressure

Investigations on the melting and crystallization behavior of polymers under high pressure is very interesting because they improve our understanding of the polymer structure and there is practical applications for various industrial processes. The pressure dependence of the melting point is especially important for processes carried out under pressure above 500 MPa [166]. These processes involve the melting of polymers under high pressure in different processing conditions like high pressure injection molding, particle formation processes and extrusion [167–169].
It was observed that linear polyethylene (L-PE) forms as extended-chain crystal with a hexagonal structure at elevated pressure (P > 330 MPa), since crystal formed as folded chain with an orthorhombic structure below this pressure [170, 171]. Some studies were performed on the crystallization phenomena of linear polyethylene under high pressure by Hikosaka et al. [172] and Rastogi et al. [173]. It was found that the hexagonal phase is a metastable transient phase present in the orthorhombic phase region of the phase diagram. In their explanation, crystallization starts from the transient hexagonal structure and ends in a stable orthorhombic structure. The T_m - P curves for crystalline polymers were investigated by Basset and Turner [174], Takamizawa et al. [175], Yasuniwa et al. [176] and Hikosaka et al. [177] for linear polyethylene and by Nakafuku and Miyaki [178] for branched polyethylene, polypropylene and poly(1-butene).
Seeger et al. [166] studied the pressure dependence of the melting point of various polymers such as homo- and copolymers (HDPE, LDPE, PP and EVA) was studied under a nitrogen atmosphere up to 330 MPa using a high pressure differential thermal analysis cell. Several properties such as vinyl acetate content, melt flow index and molecular weight have been linked to the variation of the melting point under pressure (dT_m/dP). It was observed that the melting point linearly increased with pressure up to 330 MPa. The pressure dependence was in the range of 11-17 K/(100 MPa). Using the enthalpy of fusion at ambient pressure, it is possible to approximate dT_m/dP [179].

Moreover, the melting temperature (T_m) of branched polyethylene (B-PE) was measured up to 2 GPa using a high pressure X-ray diffraction apparatus [179]. The T_m-P curve for B-PE was proposed as:

$$(T_m/T_m^0)^c = (P + P_0)/a \quad (3.6)$$

where T_m^0 is T_m at atmospheric pressure, C = 4.78, P = 280.2 MPa and a = P_0+0.1 MPa.

3.11. Cooling Rate via Crystallinity and Melting Temperature

In order to show that modifying the cooling rate as well as the mold pressure are practical ways to control crystallization, an experiment must be developed showing the results from both slow and fast cooling rates. According to Cousineau [180], the experimental plan includes the application of an injection molding machine to produce parts out of polypropylene (PP). The temperature of the coolant was decreased leading to decrease cooling rate. Then, the same samples made using the faster cooling rate showed that by increasing the cooling rate during the crystallization process, the crystallinity decreased. This was associated with molecular kinetics as rapid cooling does not leave enough time for the polymer chains to reorganize and create crystals (freeze-in-place) [181]. As a consequence, the melting temperature increases with decreasing cooling rate. Usually, lower cooling rate or longer cooling time at any specific temperature (isothermal experiment) leads to polymer chains having more time to rearrange into a crystalline order and to produce larger crystalline structures of different thickness (lamellae and spherulites).
In chapter IV, a discussion of the results obtained from the compression molded polyethylene samples produced under different cooling rates will be presented.

3.12. Molding Temperature via Mechanical Properties, Crystallinity and Melting Point

Mold temperature may have a less apparent, but often more profound effect on the final properties. In amorphous polymers such as ABS (acrylonitrile butadiene styrene) and polycarbonate (PC), higher mold temperatures produce lower levels of molded in stress and consequently better impact resistance, stress-crack resistance, and fatigue performance.

But in semi-crystalline materials, the mold temperature is a key factor in controlling the degree of crystallinity in the polymer as it controls several performance parameters including creep, fatigue and wear resistance, as well as dimensional stability at elevated temperatures. Crystals can only be produced at temperatures below the melting point, but above the glass transition temperature (Tg) of the polymer [182].

Kunz et al [181] found that the enthalpy of fusion increases with increasing mold temperature. As a result, larger crystals can better form. This behavior is expected since at the microstructure level, the amount of nucleating sites increases with increasing mold temperature, which macroscopically leads to higher melting temperature, degree of crystallinity and modulus. It is also known that crystallization at higher mold temperatures produces thicker and more stable crystals with higher melting temperatures [181].

CHAPTER IV. Influence of Compression Molding Conditions on the Thermal and Mechanical Properties of LDPE (Low Density Polyethylene)

4.1. Introduction

Compression molding is a current technique in polymer processing. Despite numerous studies, the effect of molding pressure on the physical properties has surprisingly not been fully investigated. In this work, the thermal and mechanical behavior of compression-molded polyethylene was investigated to better understand the relationship between processing conditions and resulting properties. The effect of molding temperature, pressure, temperature profile and cooling rate on the tensile and flexural moduli, as well as the melting point of polyethylene was studied. Surface tension was also investigated as a physico-chemical property for samples produced under different molding pressures. It was observed that higher tensile and flexural moduli were obtained by increasing molding pressure and temperature, as well as decreasing the cooling rate. The samples were also analyzed via X-ray diffraction (XRD) and differential scanning calorimetry (DSC). The results show that the tensile and flexural moduli of asymmetric samples are improved compared to symmetric ones.

These ensuing results have been published in J. Appl. Polym. Sci., 135, pp. 46176, 2018.

4.2. Influence of Mold Temperature, Pressure and Cooling rate on the Thermal Properties of Symmetric and Asymmetric LDPE Samples

Figures 24 and 25 combined with Tables 4 to 7 present the results for the melting point, heat of fusion (ΔH_m), and crystallinity values for the samples produced (explained in Table 3). To test a hypothesis in statistics analysis, the p-value determines the significance of the results. Hypothesis tests are used to verify the validity of a claim made about a population. This claim is called the null hypothesis. A small p-value (typically ≤ 0.05) indicates strong evidence against the null hypothesis meaning that the differences between the analyzed values are negligible (Figure 23). In this case, the p-values were calculated by Excel software for data obtained as melting point and ΔH_{exp}. It can be seen that these values have high significance (p-value < 0.05) giving good accuracy for the results.

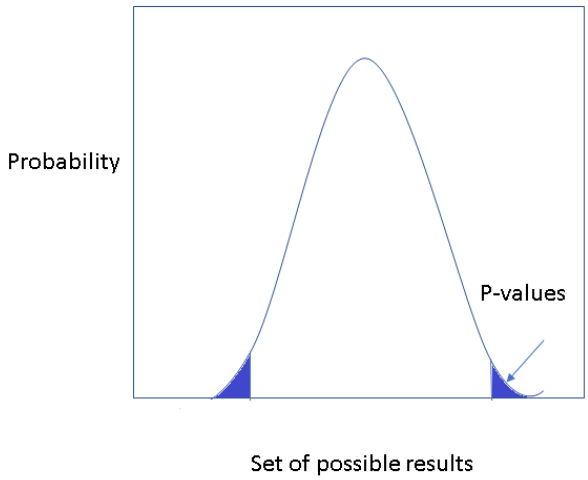

Figure 23. A p-value related to the probability of an observed result

According to Leyva-Porres [183], the data obtained from DSC experiment may show small difference. However, they can be confirmed by XRD measurements. It can then be observed here that increasing the molding temperature [34], and pressure [184], while decreasing the cooling rates [180], lead to higher melting points. As reported in the literature, crystallization at higher temperature produces thicker and more stable crystals having higher melting temperatures: T_m = 110.4, 110.6 and 111.5 °C at 135, 150 and 165 °C (Figure 24, Table 4), respectively [34]. The degree of crystallinity also confirms this increasing trend: 20.6, 22.0 and 23.2% at 135, 150 and 165 °C, respectively.

Table 4. Sample code, molding conditions, melting point, heat of fusion and degree of crystallinity of the samples produced at 3 MPa and different temperatures

Sample code	Molding temperature (°C)	Melting point (°C)	ΔH_{exp} (J/g)	χ (%)
1	135	110.4±0.1	59.9±0.3	20.6±0.1
2	150	110.6±0.1	63.7±0.3	22.0±0.1
3	165	111.5±0.1	67.3±0.3	23.2±0.1
p-value		0.027	0.012	

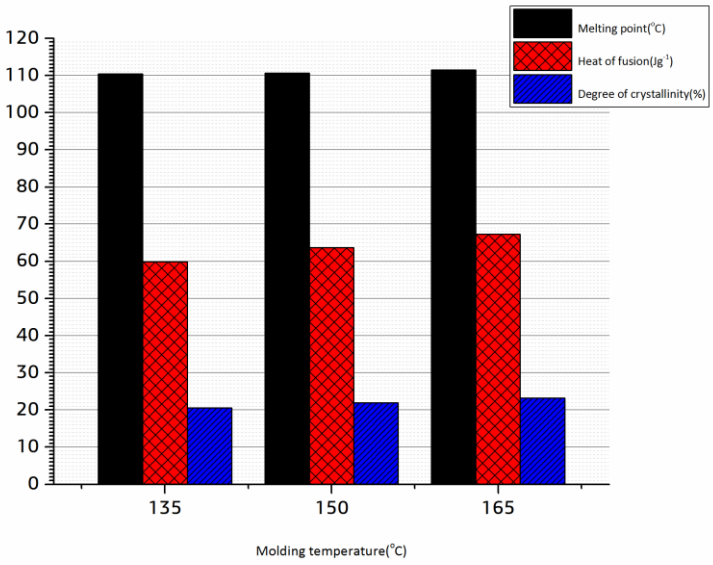

Figure 24. Melting point, heat of fusion and degree of crystallinity of the samples produced at 3 MPa and 135, 150 and 165 ºC

The compression of polymers produces lower molecular freedom and thus the entropy decreases with increasing pressure. Also, the compressibility of crystals is generally lower than that of the amorphous part, so the molar volume decrease in crystals is lower than for the amorphous region. Based on this information, it can be concluded that the decreasing Gibbs free energy during crystallization at high pressure could be more significant than at ambient conditions. When the difference in compressibility between the crystalline and amorphous regions is larger, the effect of pressure on polymer crystallization is more important [7]. Because of this decrease in total entropy of fusion, crystallization and melting occur at higher temperatures than they normally will under quiescent conditions. This fact is associated with crystal configuration. At low pressure, the main part of the orthorhombic lattice leads to hexagonal structure at high pressures [184]. Hence, higher melting temperature with increasing pressure are expected. The results presented in Figure 25 and Table 5 are in agreement with this analysis: T_m = 112.1, 113.7, 115.8 and 116.7 °C at 11, 17, 22 and 28 MPa, respectively. A similar increasing trend for the degree of crystallinity was observed with increasing pressure: 25.0, 25.8, 30.5 and 30.8% at 11, 17, 22 and 28 MPa, respectively.

Table 5. Sample code, molding conditions, melting point, heat of fusion and degree of crystallinity for the samples produced at 150 °C and different pressures

Sample code	Pressure (MPa)	Melting point (°C)	ΔH_{exp} (J/g)	χ (%)
4	11	112.1±0.1	72.5±0.8	25.0±0.3
5	17	113.7±0.1	74.9±0.5	25.8±0.2
6	22	115.8±0.2	88.4±0.3	30.5±0.1
7	28	116.7±0.2	89.4±0.5	30.8±0.2
p-value		0.017	0.009	

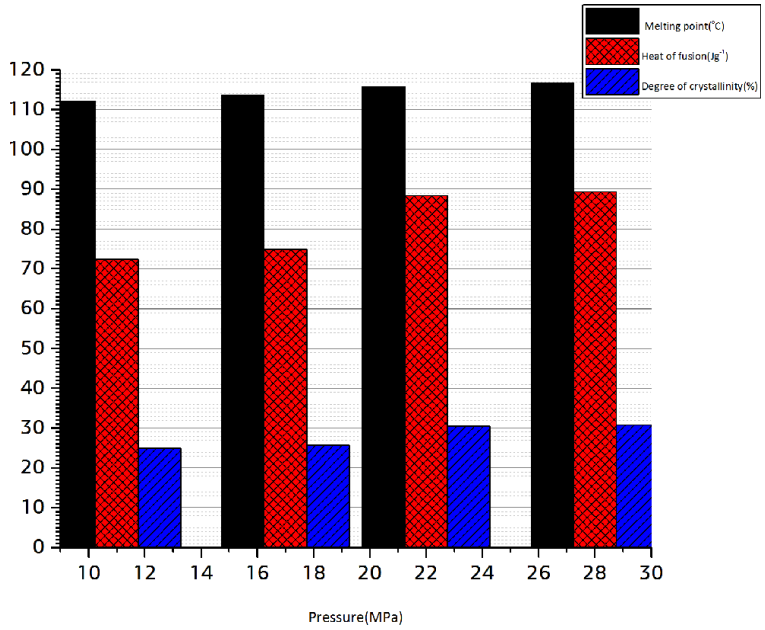

Figure 25. Melting point, heat of fusion and degree of crystallinity for the samples produced at 150 °C and 11, 17, 22 and 28 MPa

It was revealed that increasing the cooling rate during the crystallization process can decrease the crystallinity level. This is associated with the molecular kinetics as long polymer chains do not have enough time to reorganize because they are frozen in place due to short time [180]. Consequently, the melting temperature increases with decreasing cooling rate: T_m = 110.6, 111.2

and 111.8 °C at a constant mold temperature of 150 °C with a 15.6, 8.3 and 0.14 °C min^{-1}, cooling rate respectively, while T_m = 111.5, 113.6 and 115.0 °C at a constant mold temperature of 165 °C with a 15.6, 8.3 and 0.14 °C min^{-1}cooling rate, respectively (Table 6). Similar results have been observed for HDPE [185], polypropylene (PP) and poly (ethylene terephthalate) (PET) [186], Nylon 6 (PA6)-silicate nanocomposite [187], PA6 [188] and PA6 nanocomposites [189]. Moreover, the degree of crystallinity represents the expected behavior (similar to the melting temperature): 22.0, 24.6 and 26.0% at a constant mold temperature of 150 °C with a 15.6, 8.3 and 0.14 °C min^{-1} cooling rate, respectively, and 23.2, 24.9 and 29.6% at a constant mold temperature of 165 °C with a 15.6, 8.3 and 0.14 °C min^{-1}cooling rate, respectively.

Table 6. Molding conditions, melting point, heat of fusion and degree of crystallinity for the samples produced at 3 MPa and different cooling rates

Sample	Molding temperature (°C)	Cooling rate (°C min^{-1})	Melting Point (°C)	ΔH_{exp} (J/g)	χ (%)
8	150	8.3	111.2±0.2	71.4±0.6	24.6±0.2
9	150	0.14	111.8±0.2	75.6±0.5	26.0±0.2
10	165	8.3	113.6±0.2	72.7±0.9	24.9±0.3
11	165	0.14	115.0±0.2	85.7±1.0	29.6±0.3
P-value			0.042	0.046	

In general, there is no significant difference on the degree of crystallinity of the asymmetric samples produced (samples 12-17 in Table 7). This behavior clearly suggests a complex relation between structure and properties.

Table 7. Molding conditions, melting point, heat of fusion and degree of crystallinity for the samples produced at 3 MPa and different temperature profiles.

Sample	Molding Temperature (°C)	Melting point (°C)	ΔH_{exp} (J/g)	χ (%)
12	T_u = 150 T_b = 165	111.1±0.3	68.0±0.8	23.4±0.3
13	T_u = 150 T_b = 135	111.6±0.3	69.4±0.7	23.9±0.3
14	T_u = 135 T_b = 165	111.8±0.2	69.6±1.0	24.0±0.3
15	T_u = 135 T_b = 150	111.4±0.3	73.5±0.7	25.4±0.2
16	T_u = 165 T_b = 135	111.6±0.4	57.6±0.8	19.9±0.3
17	T_u = 165 T_b = 150	110.9±0.5	57.5±1.2	19.8±0.4
p-value		$9.0x10^{-7}$	$1x10^{-4}$	

XRD measurements were expected to reveal qualitatively the overall microstructure of the molded specimens. Figure 26 presents the patterns for LDPE molded under different processing conditions. The intensity of both characteristic peaks of crystalline PE, at $2\theta = 21.4°$ and 23.9° respectively [190], were changed. As the molding temperature and pressure increased, or the cooling rate decreased, the peak intensity increased. In this case, the degree of crystallinity can be calculated as [191]:

% Crystallinity = (total area of crystalline peaks) x 100 / (total area of all peaks) (4.1)

The degree of crystallinity increases as a result of higher area under the crystalline peaks [183]. These results are in agreement with the DSC data (Figure 26): more crystallization in higher molding pressure and temperature, despite lower cooling rate.

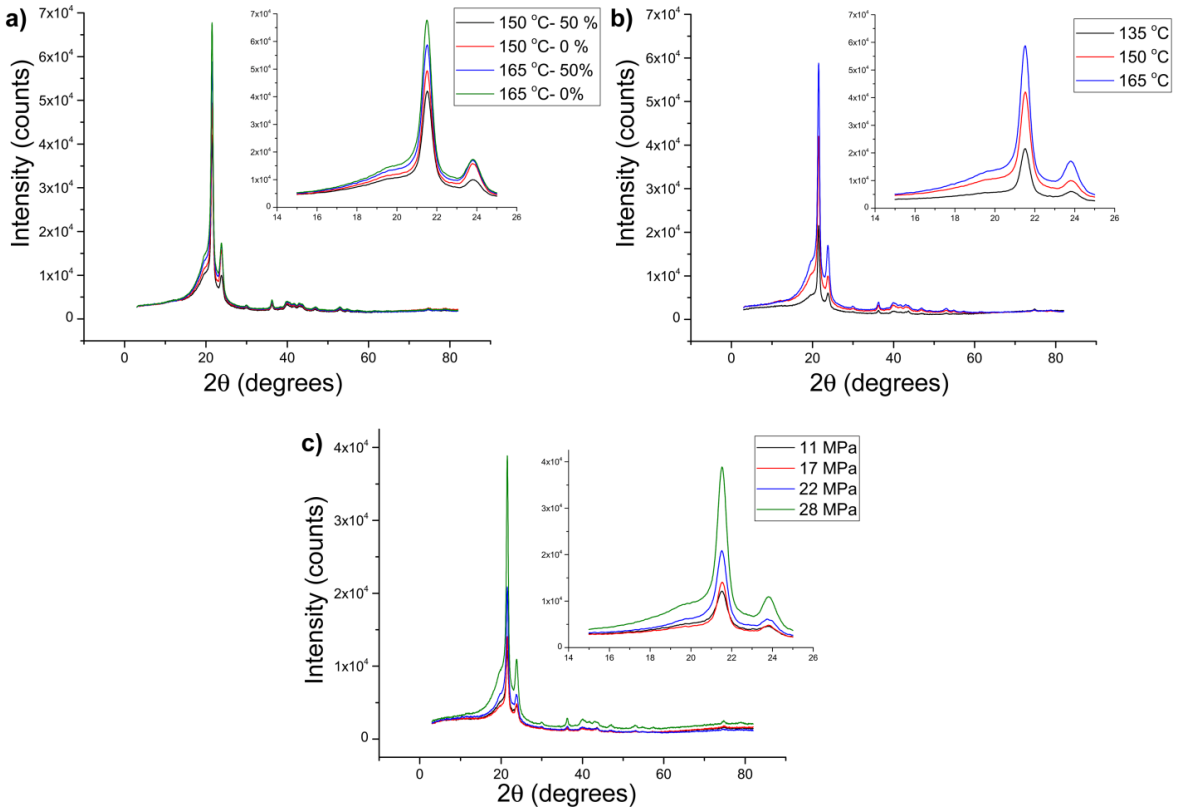

Figure 26. Diffractograms of LDPE for different molding conditions: (a) 3 MPa and different cooling rates, (b) 3 MPa and 135, 150 and 165 °C, and (c) 150 °C and 11, 17, 22 and 28 MPa

4.3. Mechanical Properties of Symmetric and Asymmetric LDPE Samples

The mechanical properties (tensile strength, elongation at break, flexural and Young's moduli) for symmetric and asymmetric samples are represented in Tables 8 to 10. The p-values were calculated for all the data obtained and the values are less than 0.05 showing significance and accuracy of the results. Table 8 presents the results for the samples produced under the same molding pressure (3 MPa), but at different molding temperatures. The elongation at break for the samples molded at 165 °C are the lowest: 404 % in comparison with 524 and 474% at 135 and 150 °C suggesting that an elevated temperature with a high pressure leads to lower strain at break [144]. There is limited improvement in tensile modulus with increasing mold temperature: 127.4, 132.0 and 134.2 MPa at 135, 150 and 165 °C. This increasing trend can be confirmed by flexural modulus measured on both sides of the samples. On the other hand, these symmetric samples have a modulus ratio (E_b/E_u) near unity. It is expected that the amount of nucleating sites is increasing as the mold temperature

increases [181]. As mentioned in section 3.12, it was observed that the enthalpy of fusion increases with increasing mold temperature. As a result, larger crystals can better form. This behavior is reasonable since at the microstructure level, the amount of nucleating sites is increasing with increasing mold temperature, which macroscopically leads to higher modulus [183].

Table 8. Molding conditions, tensile strength, elongation at break, flexural and Young's moduli for the samples produced at 3 MPa and different temperatures

Sample	Molding temperature (°C)	Tensile strength (MPa)	Elongation at break (%)	Tensile modulus (MPa)	Flexural modulus E_u (MPa)	Flexural modulus E_b (MPa)	E_b/E_u (-)
1	135	7.9±0.5	524±37	127.4±9.0	182.9±10.5	186.2±12.5	1.01±0.02
2	150	8.5±1.5	474±38	132.0±10.4	191.1±16.3	188.5±20.5	0.98±0.05
3	165	7.7±1.0	404±94	134.2±10.8	200.8±18.2	206.6±21.3	1.02±0.06
p-value		0.061	0.080	0.025	0.015	0.001	

The samples in Table 9 were produced using the same molding temperature (150 °C), but at different pressures (11, 17, 22 and 28 MPa). Increasing pressure also led to higher Young's modulus [165]. As discussed in section 3.9, a change in the interatomic distance and a decrease in the specific volume (lower free volume) may be responsible for this behavior [165]. It can be observed that the molding pressure has a significant effect on the elongation at break: 614, 641, 730 and 797% at 11, 17, 22 and 28 MPa, respectively, while the elastic modulus slightly increases: 115.1, 186.9, 203.5 and 203.8 MPa at 11, 17, 22 and 28 MPa and the tensile strength is almost constant: 11.5, 10.3, 10.8 and 10.8 MPa, respectively. Increasing flexural modulus with pressure and modulus ratio near unity can also be observed in Table 9 for these symmetric samples.

Table 9. Molding conditions, tensile strength, elongation at break, flexural and Young's moduli for the samples produced at 150 °C and different pressures

Sample	Pressure (MPa)	Tensile strength (MPa)	Elongation at break (%)	Tensile modulus (MPa)	Flexural modulus E_u (MPa)	Flexural modulus E_b (MPa)	E_b/E_u(-)
4	11	11.5±0.7	614±73	115.1±13.9	232.7±10.8	234.2±11.2	1.0±0.03
5	17	10.3±1.3	641±71	186.9±20.5	253.1±12.3	249.7±18.1	0.98±0.02
6	22	10.8±1.2	730±77	203.5±8.9	263.3±10.2	268.6±13.9	1.02±0.04
7	28	10.8±1.4	797±91	203.8±6.2	277.8±14.5	274.6±11.4	0.98±0.05
p-value		0.016	0.006	0.013	0.012	0.013	

The results also show that the Young's modulus increases with decreasing cooling rate for the samples in Table 10: 132.0, 132.9 and 147.3 MPa at a constant temperature of 150 °C with 15.6, 8.3 and 0.14 °C min^{-1}cooling rate respectively, while 134.2, 173.2 and 216.3 MPa at a constant temperature of 165 °C with a 15.6, 8.3 and 0.14 °C min^{-1}cooling rate, respectively. Moreover, several types of microstructures with different arrangements have been produced during the crystallization of semi-crystalline polymers, which is associated to the cooling rate [192].

As previously discussed, decreasing the cooling rate during the crystallization process can increase the degree of crystallinity because the polymer chains and microstructures have more time to relax and diffuse leading to more organized systems [184]. The flexural modulus on both sides has a similar trend with decreasing cooling rate.

Table 10. Molding conditions, tensile strength, elongation at break, flexural and Young's moduli for the samples produced at 3 MPa and different cooling rates

Sample	Molding temperature (°C)	Cooling rate (°C min^{-1})	Tensile strength (MPa)	Elongation at break (%)	Tensile modulus (MPa)	Flexural modulus E_u (MPa)	Flexural modulus E_b (MPa)	E_b/E_u (-)
8	150	8.3	8.9±0.8	586±66	132.9±4.2	197.5±16.5	196.2±15.4	0.99±0.02
9	150	0.14	9.2±1.4	511±85	147.3±9.3	232.0±10.3	236.6±10.9	1.01±0.04
10	165	8.3	9.9±0.8	731±91	173.2±6.5	231.6±14.5	230.4±14.3	0.99±0.02
11	165	0.14	10.7±1.7	622±82	216.3±7.5	283.1±15.6	284.3±12.1	1.00±0.02
p-value			0.042	0.032	0.044	0.046	0.047	

Finally, a temperature gradient was imposed while molding to get asymmetric samples and their properties are presented in Table 11. Based on the literature [193], molding with a temperature gradient has important effects on density profiles. In this case, the density continuously decreases from the cold side to the hot side of the mold [198]. It was observed that higher flexural strength was obtained when the load is applied on the side having the highest density [193]. In our case, the flexural modulus of all the samples (Table 11) is lower when the load is applied on the hot side. For example, sample 15 exhibits a modulus of 324.0 MPa for T_u = 135 °C, while it is only 294.9 MPa at 150 °C. Previous study from our lab confirms these behaviors [193].

Sample 15 molded at T_u=135 °C and T_b=150 °C displays the highest tensile and flexural modulus on both sides (15 °C difference and lowest average temperature between both plates). The lower tensile modulus was obtained for samples 16 and 17. Sample 16 was molded at T_u=135 °C and T_b = 165 °C (high temperature difference = 30 °C) and sample 17 was molded at T_u = 165 °C and T_b = 150 °C (15 °C difference and highest average temperature between both plates = 157.5 ºC). It can be concluded that the highest tensile and flexural modulus, besides having the highest crystallinity degree (25.4%), was obtained for the lowest temperature on both plates (sample 15). Higher average temperature and higher temperature difference between the plates both result in lower mechanical properties of the samples. This can be confirmed by using the flexural modulus ratio (E_b/E_u). Depending on the density distribution, the modulus ratio can be higher or lower than unity [194]. It was observed that the modulus ratio was higher than unity when the density profile decreases. In contrast, the ratio is below unity when the density profile increases with depth [194]. Thus, decreasing density profile and flexural modulus ratio above unity for samples 16 and 17 leads to lower tensile modulus. On the other hand, increasing density profile and flexural modulus ratio below unity, as observed in sample 15, leads to higher tensile modulus. It can be argued that the density profile has a very important role in asymmetric samples. To confirm its role, more investigation must be performed, but goes beyond the scope of this study. It must also be pointed out that while elongation at break increases, the tensile strength is almost constant for samples 15, 16 and 17.

A comparison between the tensile and flexural moduli of the samples with a reverse cold and hot side shows the same range of the values within the standard deviation, as it is the case for samples

13 and 15. It can be concluded that reversing the temperature of the bottom and upper sides does not affect our results significantly.

Surface tension of polymers is seldom studied, mostly because insufficient techniques are available [195]. The surface tension measured for the samples produced under different pressure at constant temperature (150 °C) is presented in Figure 27. It can be observed that by increasing the molding pressure, surface tension decreases. As previously described, decreasing the Gibbs free energy during crystallization at higher pressure should be more important than at ambient conditions [7]. According to Equation (3.4), there is a direct relation between surface tension and Gibbs free energy at constant temperature and pressure. The effect of pressure and sample density on polymer crystallization is more important when the compressibility difference between the crystalline and amorphous regions is larger.

Table 11. Molding conditions, tensile strength, elongation at break, flexural and Young's moduli for the samples produced at 3 MPa and different temperature profiles

Sample	Molding temperature (°C)	Tensile strength (MPa)	Elongation at break (%)	Tensile modulus (MPa)	Flexural modulus E_u (MPa)	Flexural modulus E_b (MPa)	E_b/E_u (-)
12	$T_u = 150$ $T_b = 165$	8.7±0.6	544±63	123.5±15.0	264.7±26.4	250.2±10.2	0.94±0.06
13	$T_u = 150$ $T_b = 135$	10.3±0.9	720±71	128.6±0.9	284.9±20.1	302.6±16.6	1.06±0.05
14	$T_u = 135$ $T_b = 165$	9.7±1.6	590±95	125.6±6.4	266.7±20.3	222.6±15.2	0.83±0.05
15	$T_u = 135$ $T_b = 150$	9.1±1.4	561±65	135.3±12.3	324.0±21.5	294.9±12.6	0.91±0.04
16	$T_u = 165$ $T_b = 135$	9.2±1.0	631±89	122.9±10.5	266.8±19.7	270.2±24.7	1.01±0.07
17	$T_u = 165$ $T_b = 150$	8.5±1.4	632±95	119.1±9.1	234.9±11.3	245.6±20.1	1.04±0.09
p-value		2.9×10^{-5}	3.33×10^{-5}	1.47×10^{-5}	1×10^{-4}	1×10^{-4}	

When the polymer has a lower surface tension, the activation energy barrier for crystallization will be reduced, and the nucleation rate will increase. It is obvious that changes in surface tension are crucial to polymer foaming processes, and it is essential to control such a property in order to optimize the polymer involved in industrial applications [196]. Furthermore, it was seen that when

intermolecular forces weaken, kinetic energy increases and molecular movements inside the crystal intensify, leads to increase of melting temperature [197]. Augmentation of melting temperature in higher molding pressure and lower surface tension was confirmed with our result, too. Besides, in the literature contradictory information can be found concerning surface tension relation with mechanical properties. In some cases the modulus increased [198-200], or even decreased [201] as a reduction of surface interactions. Jin He [202] observed that the Young's modulus is not influenced by the surface tension. As we discussed before, samples produced at using greater molding pressure have higher Young's modulus, though lower surface tension.

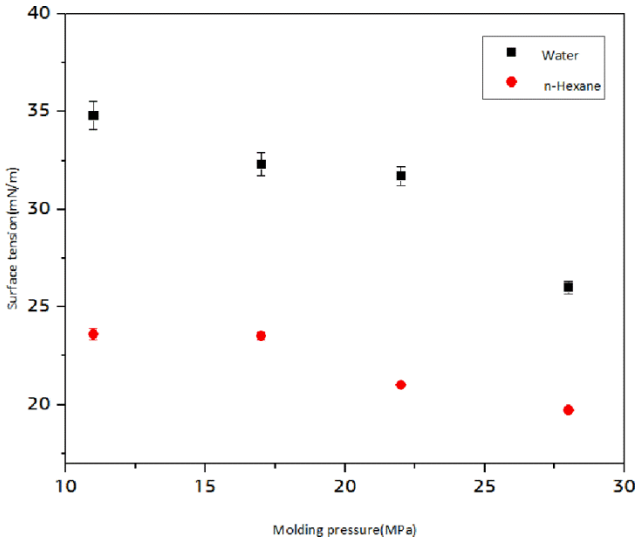

Figure 27. Surface tension of the samples produced under different molding pressure, as measured in water and n-hexane.

4.4. Conclusion

Considering the effect of processing conditions on polyethylene crystallization requests further knowledge regarding the impact of the parameters controlling the ultimate properties of the end products. In this study, the effect of mold temperature, mold pressure, cooling rate and temperature profile on the thermal and mechanical properties of the samples were investigated. Results confirmed that for symmetric samples (uniform molding temperature), higher melting temperature, flexural and tensile modulus stem from an increase in the molding pressure and molding temperature, while decreasing the cooling rate. These trends are in agreement with the behavior of the degree of crystallinity and WAXD diffraction pattern observed. On the other hand, for

asymmetric samples where temperature gradient is applied while molding, the tensile and flexural modulus not only depend on the temperature difference, but also on the average temperature between the upper (T_u) and bottom (T_b) plates of the compression molding press. It was observed that the highest tensile and flexural moduli were obtained for the lowest temperature on both plates. This behavior can be clearly revealed using the flexural modulus ratio which represents the value measured when the load is applied on the bottom or the upper sides (E_b/E_u). In all cases, it is clear that complex relations exist between the molding conditions and the final properties of semi-crystalline polymers and more work is still needed to fully understand the behavior of a part under different types of solicitation. Gibbs free energy decreases upon crystallization. Finally, it was shown that increasing the molding pressure (pressure induced-crystallization) results in lower surface tension which can be explained by a sharper depression of the Gibbs free energy during crystallization as result of lower molar volume. Thus, further study will be needed for better comprehension of the impact of other processing conditions (i.e. molding temperature and cooling rate) on surface tension. The relation of surface tension with thermal and mechanical properties will be thoroughly discussed and reported in the due time.

Chapter V: Melting of Alkane Nanocrystals: Towards a Representation of Polyethylene

5.1. Introduction

The properties of nanomaterials and their corresponding bulk materials are different as a result of presence of interface, especially for polyethylene nanocrystal which attracted considerable attention. This article is thus aimed at revealing the environment effect on the melting temperature of alkane chains nanocrystals using molecular dynamics (MD) simulation. It has been shown that the Gibbs-Thomson law can be reproduced using atomic simulation [1]. This law reveals the linear relationships between the melting temperature and the inverse of the crystal thickness. By varying the temperature, an energy jump is observed. It has been shown to be directly related to the melting point. The crystal edges and the alkane chain length have been varied to determine the effect of environmental conditions and interface on the melting behavior of a nanocrystal composed of alkane chains embedded in an amorphous phase. The effect of interactions with neighboring chains can thus be observed by comparing the MSD (mean square deviation) of one particle near the crystal surface stemming from the isolated crystal with alkane chains nanocrystal embedded in an amorphous phase. By using MD simulation, interfacial tension was calculated to be 37$\pm$5 dyne/cm, which is in good agreement with the experimental value of 30.7 dyne/cm for low density polyethylene.

In the following the pressure dependence of the melting point in our system was determined up to 3000 atm. Also, the surface tension was calculated to relate the effect of pressure. It was found that increasing pressure led to lower surface tension that can be explained by a decrease in the total entropy of fusion which follows increase of melting temperature and lower Gibbs free energy. This behavior was observed in experimental samples as well (Chapter 4, Figure 27).

5.2. Molecular Dynamic Simulation of Alkane Chains Nanocrystal embedded in an Amorphous phase: Melting Temperature and Surface Tension via the Gibbs-Thomson Equation

Based on studies represented in section 2.19., the melting temperature was determined for different crystal dimensions (explained in section 2.17.). To get T_m values for a specific lamellar thickness *l*, an infinite slab must first be obtained, making available the use of the GT equation. For this, the edges must be taken into account. So, the crystal melting point is obtained from a modified Gibbs-Thomson equation as discussed in chapter I (Eqn. (1.13)) [203].

Theses equations are repeated here to get a closer look. In Equation (1), $\frac{1}{\bar{x}} = \frac{1}{y} + \frac{1}{x}$ where $\bar{x}$ is the harmonic mean of the lateral dimensions (x and y), while T^0_m and Δh_m are the melting temperature for infinitely large crystal and melting enthalpy per unit volume of the bulk, respectively. respectively:

$$T_m = T_m^0[\,1 - \frac{2\sigma_c}{\Delta h_m}\frac{1}{l} - \frac{2\sigma}{\Delta h_m}\frac{1}{\bar{x}}] \tag{5.1}$$

where σ_c is the fold surface free energy and σ is the surface free energy of lateral edges. By assuming *l* to be constant while letting x and y to change one gets:

$$T_m = \alpha\frac{1}{\bar{x}} + \beta(l) \tag{5.2}$$

where

$$\beta(l) = T_m^0[1 - \frac{2\sigma_c}{\Delta h_m}\frac{1}{l}] \quad : \tag{5.3}$$

So, the Gibbs-Thomson equation can be approximated by:

$$T_m = T^{\infty}_m[1-\frac{2\sigma_c}{\Delta h_m l}] \tag{5.4}$$

Figure 28 reports the T_m values by letting x and y to change for different *l* values.

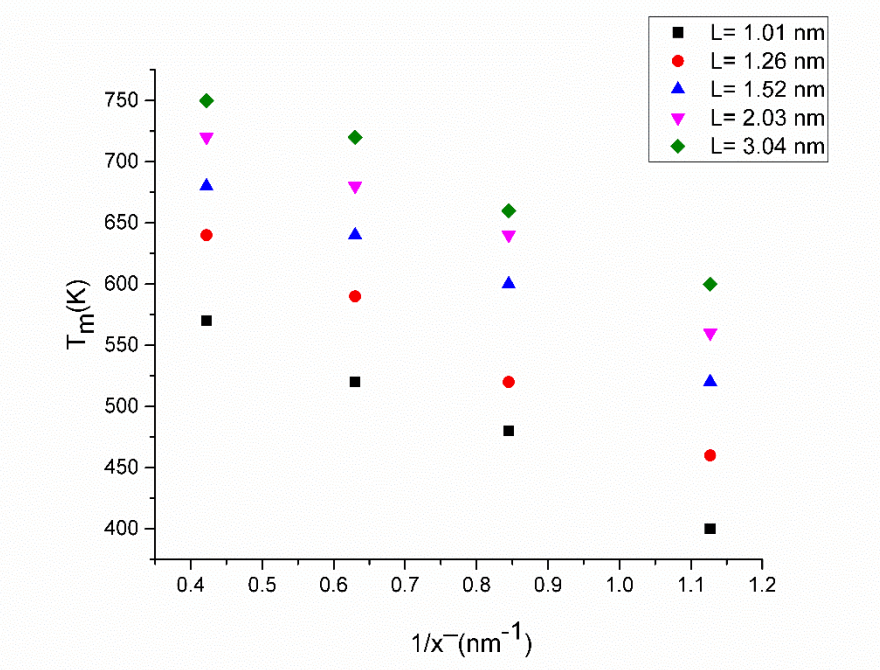

Figure 28. Simulated T_m from Eqn. (5.2) for *l*: 1.01, 1.26, 1.52, 2.03 and 3.04 nm (c = 2.5534 Å, explained in 2.17.) to $1/\bar{x}$.

Table 12: Slope (α) and the ordinate at the origin (β(l)) of Eqn.(5.2) for different *l* values.

l (nm)	α (-)	β(l) (K)
1.01	-297.5	738
1.26	-294.3	792
1.52	-251.0	814
2.03	-251.0	854
3.04	-254.0	890

From Figure 28, linear regression gives the α and β(*l*) values via Eqn. (5.2) as reported in Table 12. As expected, Figure 29 shows a linear relation between T_m and $1/l$ according to Eqn. (5.4).

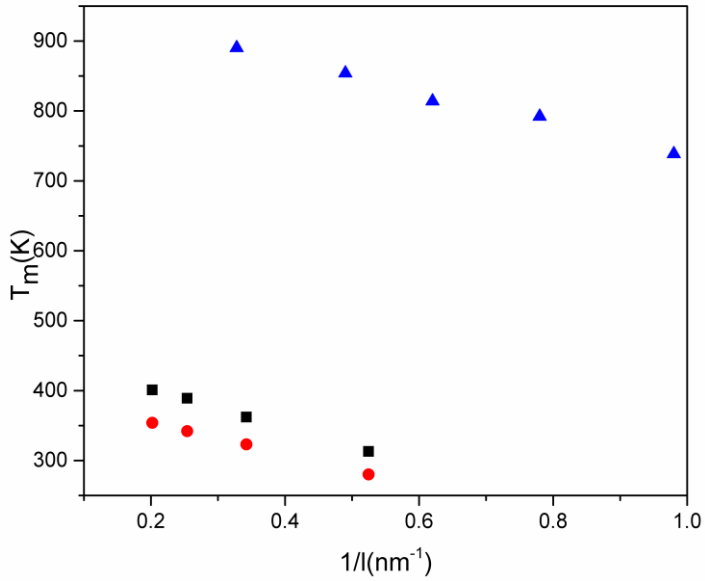

Figure 29. Gibbs-Thomson representation of the experimental (circle) and simulated (square) T_m as a function of 1/*l* for isolated alkane chains nanocrystal compared with the simulated (triangle) T_m for alkane chains nanocrystal in an amorphous phase

For chain molecules, the conformation entropy increases on melting. It can be concluded that the crystal conformation plays a very important role in the melting process (melting temperature) [204]. In polymer crystals, the main driving force ordering chains into the crystalline state is the attraction among the non-bonded monomers which are mainly van der Waals and polar in nature [205].

When an attractive interface is present, fixing the chains adjacent to the surface occurs. Covalent bonds between atoms in polymer chains are much stronger than crystal bonds in alkane chains nanocrystal. This factor increases the melting temperatures of polymers and can affect crystallization by changing both the entropic and enthalpic contributions [206]. As a result, the melting temperature increases in comparison with isolated crystalline system (Figure 29). For better understanding of this phenomenon, Figure 30 presents the mean square deviation (MSD) of one particle near the surface of the crystal phase in an isolated crystal and in our system: i.e. alkane

chains crystal embedded in an amorphous phase. MSD is a measure of the deviation time between the position of a particle and some reference position which can be calculated as [207]:

$$MSD \equiv \langle (x - x_0)^2 \rangle = \frac{1}{N} \sum_{n=1}^{N} (x_n(t) - x_n(0))^2 \quad (5.5)$$

The Lindemann criterion [208,209] explains that during the melting process of solid, the average amplitude of thermal vibrations increases with temperature. When melting occurs, the vibration amplitude becomes large enough for atoms displacements (motion) compared to their equilibrium lattice sites which should be in the range of one-half of the intermolecular distance [210]. So far, it is observed that melting occurs when the mean square displacement (MSD) of a particle of crystalline solid exceeds a threshold value [211]. Figure 30 confirms the MSD increase in two systems. However, it should be expected that because of pinning of the crystalline chains adjacent to the alkane chains for conformation embedded in amorphous phase, there is a decrease in atom mobility and displacements near the surface of crystal phase in comparison with isolated crystal during melting.

In this case, if we compare MSD of our system with isolated crystal (Configuration 4a4b5c) in (T= 440 K, $T>T_m$), it can be revealed that the presence of alkane chains around crystal develops the interaction between crystalline and alkane chains leading to reduction of atoms mobility placed near the surface of crystal phase (circle curve in comparison with square curve). The value of MSD for one particle in amorphous phase (triangle curve) is significantly higher than one particle near the surface of crystal (circle curve) in current configuration. This fact can be confirmed by other crystals with different dimension and thickness.

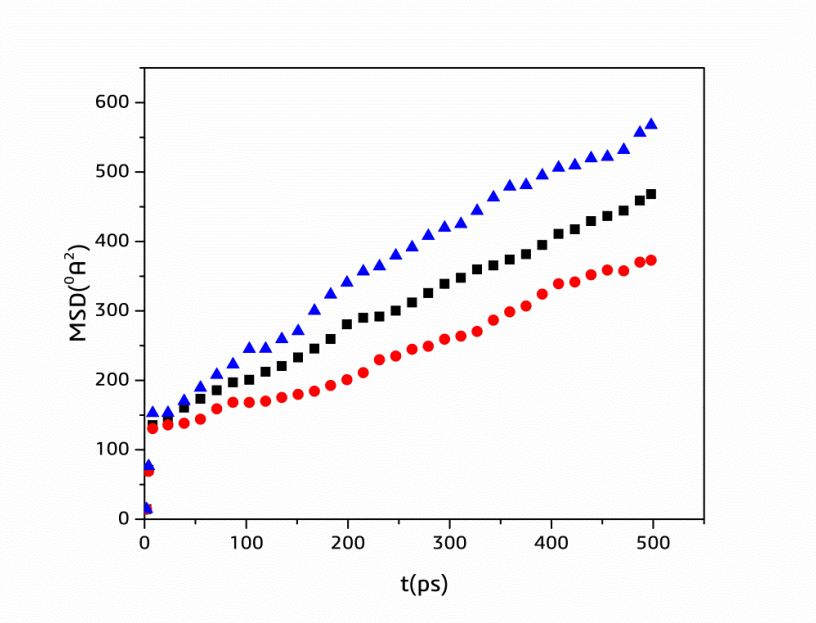

Figure 30. Mean square deviation of one particle on surface of alkane chains crystal at T=440 K $T>T_m$ by 4a4b5c, isolated alkane chains crystal (square), alkane chains crystal within amorphous phase (circle) and one particle in amorphous phase (triangle)

Zubova et al. [212] studied the molecular mechanism of the chain diffusion between crystalline and amorphous fractions in semi-crystalline polyethylene (PE). They obtained the diffusion coefficient in a simplified MD model of the PE crystal with united atoms: 4×10^{-2} cm^2/s [212]. Along with comparing the MSD curve behavior for different particles, we computed diffusion coefficient for one particle near the surface of nanocrystal for isolated alkane chains crystal (square), alkane chains crystal within amorphous phase (circle) and one particle in amorphous phase (triangle) from the slope of MSD after 50 ps [Figure 30] and D = 1.2×10^{-1}, 9×10^{-2} and 1.5×10^{-1} cm^2/s, respectively.

In an attempt to calculate surface tension using Gibbs-Thomson equation, the experimental and simulated variations of T_m/T^0_m as a function of $1/l$ are presented in Figure 31 for isolated alkane chains crystal and crystal with different lengths within amorphous phase to calculate the interfacial tension.

A linear regression can be made to the slope $\frac{\sigma}{\Delta hm}$ (Equ. (5.4)) from atomic simulation. (Δh) is calculated for alkane chains nanocrystal of infinite length. Interfacial chains in comparison to bulk

chains play important role to calculate the value of the melting enthalpy. (Δu_m) obtained as the jump in potential energy plot [213].

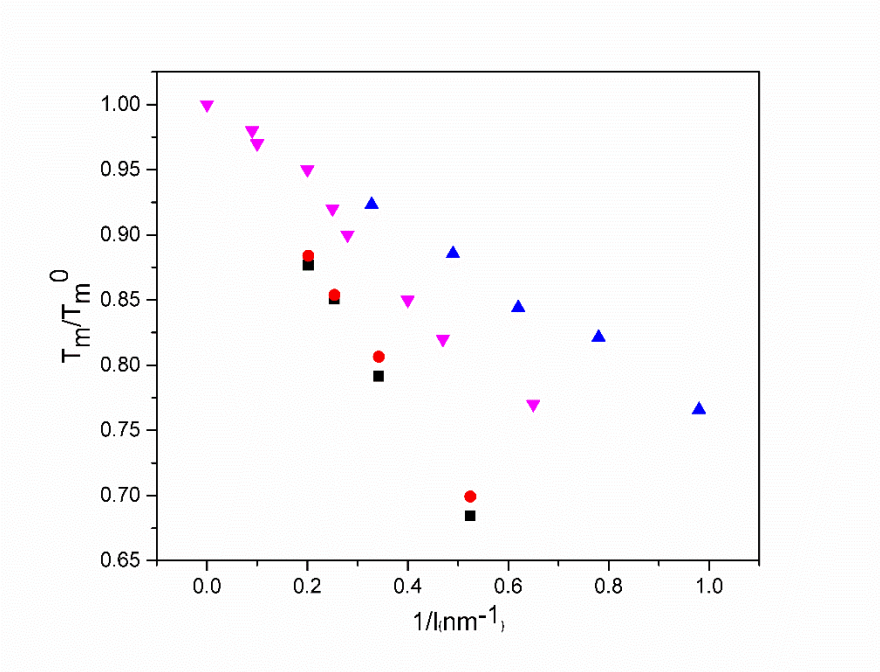

Figure 31. Modified Gibbs-Thomson equation representation reporting experimental (circle) and simulated (square) T_m/T^o_m for isolated alkane chains nanocrystal and experimental (inverted triangle) simulated (triangle) T_m for alkane chains nanocrystal in amorphous phase versus 1/*l*

We assumed (Δh_m) equal to (Δu_m) and neglected the Laplace pressure as a result of infinite edge distances x and y and infinite crystal thickness *l* in the bulk. In thermodynamics:

$$\Delta H = \Delta U + P\Delta V \tag{5.6}$$

The pressure in this equation is obtained from Laplace pressure. The Laplace pressure is determined from the Young–Laplace equation as:

$$P_1 - P_2 = \gamma_L \left(\frac{1}{R_x} + \frac{1}{R_y}\right) = P_L \tag{5.7}$$

where $P_1 - P_2$ is pressure difference, γ_L is the surface tension and Rx, Ry are radii of curvature. At infinite x, y and l, the surface becomes flat. For a flat surface, the $R \rightarrow \varphi$ and there is no pressure

difference across a planar boundary. So, imposing (Δh_m) equal to (Δu_m) by ignoring Laplace pressure as a result of infinite edge distances x and y and infinite crystal thickness *l*. (ΔE) can be computed by considering two lines leading the differences in energy (Chapter II- Figure 17).

$$\Delta E = E_2 - E_1 = (T_m * X_2 + Y_2) - (T_m * X_1 + Y_1) \quad (5.8)$$

where X_1, X_2 and Y_1, Y_2 are intercepts and slopes of two lines before and after melting point.

The actual energy extracted from the simulations carried out in the canonical ensemble corresponds to the internal energy (u). In addition, the entropy of melting obtained from equation 5.9 [214]:

$$\Delta S_m = \frac{\Delta H_m}{T_m} \quad (5.9)$$

Table 13 presents the values of ΔH, ΔS, σ, ΔE, T_m and volume for different alkane chains nanocrystals.

The mean values of (ΔH) and (ΔS) were computed as 276.8$\pm$44 J g^{-1}, 0.47$\pm$0.11 J/ (g K)$^{-1}$. They correlate well with the generally accepted experimental values of 280 J g^{-1} and 0.53 J/ (g K)$^{-1}$ for semi-crystalline polyethylene, respectively [215,216]. The interfacial tension can be calculated from Equation (5.4) using the triangle curve representing the alkane chains nanocrystal embedded in an amorphous phase (Figure 31). The ensuing result 37$\pm$5 dyne cm^{-1} is in agreement with results published in the literature 30.79 dyne cm^{-1} [217] for semi-crystalline polyethylene. In our previous article, the surface tension (84$\pm$14 dyne cm^{-1}) was calculated for isolated alkane chains nanocrystal and compares favorably with the experimental value (110 dyne cm^{-1}) [203]. So, this surface tension decreases in our system can be explained by higher melting temperature as discussed before. It is known that when the kinetic energy increases, molecular motion inside the crystal intensify and intermolecular force weakens with increasing temperature leading to lower surface tension [218]. On the other hand, when the crystal monomer chains are pinned by an attractive layer caused by presence of alkane chains within the amorphous phase, it facilitates the crystal melting process. This increases the tendency of crystal to have interaction with alkane chains [207]. If this is the case, then the surface tension depression would be a function of the interactions between the crystal

and the amorphous phase as well. The difference between simulated and experimental values may be due to the choice of the force field and to kinetic effects [219].

Table 13: Crystal dimensions, enthalpy, entropy, surface tension, difference of energy, melting temperature and volume of alkane chains nanocrystal while a = 7.424, b = 4.949 and c = 2.553 Å (explained in section 2.17.)

Crystal dimension	ΔH (J/g)	ΔS (J/g K)	σ (dyne/cm)	E_2 (kcal/mol)	E_1 (kcal/mol)	E_2-E_1 (kcal/mol)	T_m (K)	Volume (Å^3)
3a3b4c	203	0.50	28	140.7	40.99	99.75	400	3328.5
4a4b4c	341	0.71	47	794.6	497.0	297.5	480	5917.3
6a5b4c	338	0.65	46	1070.3	516.9	553.4	520	11095.0
8a8b4c	233	0.40	32	2373.4	1559.4	813.9	570	23669.4
3a3b5c	285	0.61	39	1102.4	928.3	174.1	460	4160.6
4a4b5c	286	0.55	39	1910.1	1598.9	311.21	520	7396.7
6a5b5c	237	0.40	32	3046.9	2564.3	482.66	590	13868.8
8a8b5c	256	0.37	35	5796.6	4462.1	1334.5	640	29586.8
3a3b6c	303	0.58	41	2412.5	2198.0	221.71	520	4992.7
4a4b6c	369	0.61	51	4005.1	3525.0	480.0	600	8876.0
6a5b6c	254	0.39	35	4821.0	4200.8	620.2	640	16642.5
8a8b6c	256	0.37	35	5796.6	4462.1	1334.5	680	35504.1
3a3b8c	315	0.56	43	3100.4	2793.6	306.7	560	6657.03
4a4b8c	342	0.53	47	4680.1	4087.8	592.2	640	11834.7
6a5b8c	254	0.37	35	5408.1	4584.0	823.3	680	22190.1
8a8b8c	244	0.34	33	6893.9	5201.0	1692.8	720	47338.9
3a3b12c	267	0.44	37	3852.9	3464.1	388.8	600	9985.5
4a4b12c	270	0.41	37	5052.7	4352.9	699.7	660	17752.1
6a5b12c	236	0.32	32	6882.9	5734.9	1147.9	720	33285.1
8a8b12c	242	0.32	33	9512.5	7003.9	2508.6	750	71008.3

Even though the melting point of the polyethylene bulk crystal is not changed by the environment, melting temperature of polyethylene nanocrystal is influenced by dimension, layer thickness and presence of amorphous phase around the crystal.

Hence, by simulating alkane chains nanocrystal embedded in an amorphous phase as a representation of semi-crystalline polyethylene and comparing with isolated alkane chains nanocrystal, higher melting temperature and lower surface tension were observed which can be explained by the reduction of atoms entropy placed on the crystal surface and this can be confirmed by experimental data.

5.3. Pressure Effect on the Melting Behavior of Alkane Chains Nanocrystals: Molecular Dynamic Simulation

In this part, system (explained in 2.17.) was constructed to study the effect of pressure on the Gibbs-Thomson equation. Each molecular dynamics simulation was performed for a total of 500 ps at temperatures ranging from 260 K to 800 K with 5 K increments for thickness of layer L = 7.5, 10 and 30 Å. The pressure was fixed by using a Berendsen barostat [220] at 0, 1000, 1500 and 2000 atm which rescales the system volume and the atoms coordinates within the simulation box every time step.

Figure 32 presents the different simulation result ($\frac{2\sigma_c}{\Delta h_m}$)of T_m/T_m^0 plots as a function of $1/l$ (Eqn. (5.4)) at 0, 1000, 1500, and 2000 atm. Enthalpy and surface tension at different pressures can be calculated to determine their effect on the Gibbs-Thomson equation.

The results obtained as interfacial tension in different pressure are 38±4, 12.8±1.2, 4.6±0.9 and 3.6±0.9 dyne/cm at 0, 1000, 1500 and 2000 atm, respectively. As expected, surface tension decreases with increasing pressure [7]. Accordingly, Eqn. (3.4) predicts a decrease of surface tension as a result of depression in Gibbs free energy and this trend is consistent with literature data [7]. This behavior was confirmed in experimental samples as well (Chapter IV, Figure 27). Figure 27 showed that increasing the molding pressure (pressure induced-crystallization) results

in lower surface tension which can be explained by a sharper depression of the Gibbs free energy during crystallization as a result of lower molar volume.

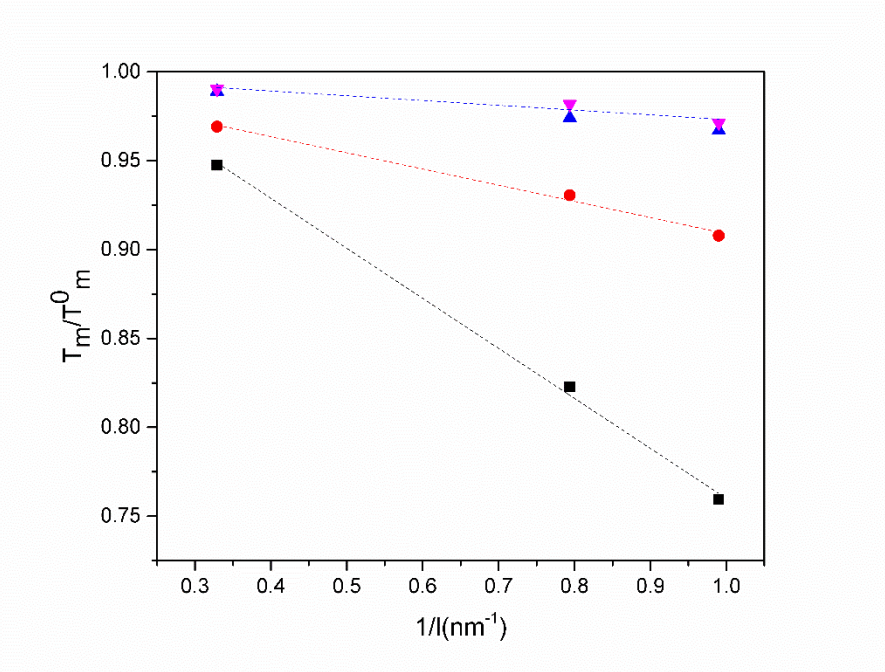

Figure 32. Gibbs-Thomson representation of the simulated T_m versus $1/l$ at 0 (square), 1000 (circle), 1500 (triangle), and 2000 (inverted triangle) atm

At 1500 and 2000 atm, there is a small difference between the values of surface tension. It can be confirmed with polystyrene and polypropylene experimental data that their surface tensions represent a slower decrease at higher pressures [221].

Figure 33 presents a comparison between the values of the melting temperature as a function of pressure. As described in section 3.10. and observed experimentally in Table 5, increasing pressure leads to an increase in melting temperature [184]. Seeger et al. [38] reported the melting temperature of LDPE under high pressure. In their experiment, it is reported that the $\frac{dT_m}{dP}$ is 0.021 K/atm. This value must be compared with 0.037 K/atm obtained from the simulation for one crystal dimension and thickness of layer [4a4b3c, L = 7.59 Å].

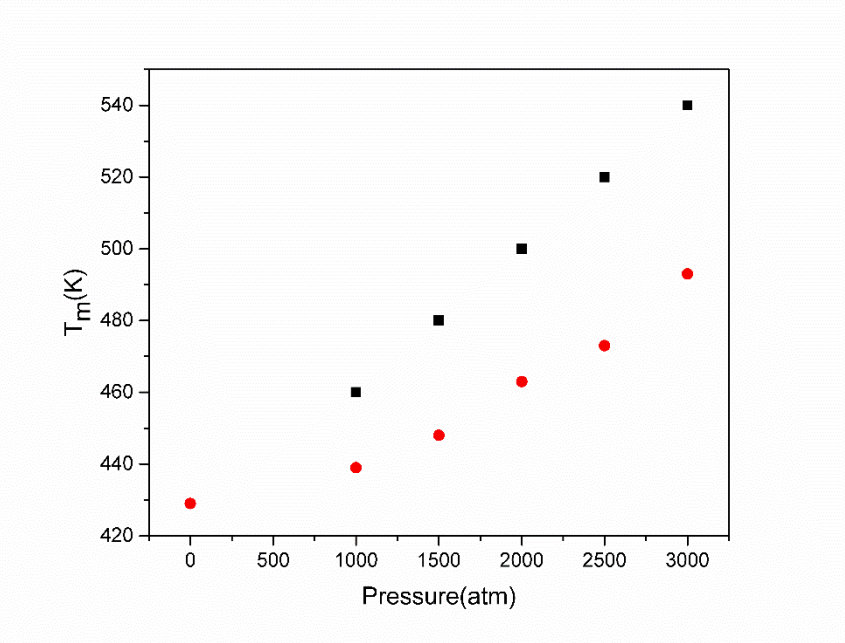

Figure 33. Effect of pressure on the melting temperature of polyethylene crystal: Comparison between experimental (circle) [7] and simulation (square) data by 4a4b3c alkane chains crystal within amorphous phase

5.4. Conclusion

In this study, we proposed a model that approach the true polyethylene by considering interfaces to evaluate the molecular characteristics of nanocrystals. To validate this model, we compared simulation results with experiments. Reporting the ratio of the melting temperature by calculating the melting temperature for an infinite chain length helped us to find a good match between simulated and experimental data. We simulated alkane chains nanocrystal embedded in the amorphous phase (52 chains, each chain with 30 carbons) in the canonical ensemble to compute the melting temperature of sheets of nanocrystals with different lengths. By focusing on melting temperature of different crystals with infinite chain length, we reported the heat of melting per CH_2 (units) in alkane chains nanocrystal. Interfacial tension was thus computed and compared well with experimental data. Thus, comparing the results from alkane chains nanocrystal embedded in an amorphous phase with isolated crystal, we observed melting temperature increase and surface tension decrease. To address this issue, MSD plots of one particle near the crystal surface in both systems were computed. Interactions between unbonded monomers in crystal and alkane chains in

the amorphous phase decreased the chains mobility in the crystal leading to higher melting temperature and lower surface tension.

The impact of pressure on melting temperature and surface tension was investigated as well. It was shown that increase of pressure and decrease of molar volume results in decrease of surface tension, which can be explained by sharper depression in Gibbs free energy. Furthermore, comparing experiments and simulation data gave us an accurate match that by increasing pressure, melting point of samples will increase too. It can be explained by a decrease in total entropy of fusion.

Conclusion

Compression molding, injection molding, blow molding and blow film extrusion are diverse polymer processing techniques to make end user plastics. These processing operations are performed at elevated temperatures and pressures [1, 2]. It is of fundamental and industrial interest to investigate the melting and crystallization behavior of polymers under such conditions in order to better understand and thus to improve these processes.

Over the past several decades, polyethylene (PE) was a commodity polymer that has become more used because of its good mechanical properties and low price. Low-density polyethylene (LDPE), high density polyethylene (HDPE) and polypropylene (PP) are very sensitive to the conditions in which they are produced. Geometry, pressure and cooling rates are known to influence their degree of crystallinity, which in turn strongly affects their mechanical, optical and barrier properties [3].

This work is thus aimed at revealing the environmental conditions on the melting temperature and surface tension of PE nanocrystals using molecular dynamics simulation. To efficiently approach the true polyethylene by considering interfaces and reveal the impact of environmental conditions, a nanocrystal composed of alkane chains was embedded in an amorphous phase. Based on previous work in our research group, the linear relationships between the melting temperature and the inverse of the crystal thickness was proved using the Gibbs-Thomson equation. By varying the temperature, a jump in the energy gives the melting point. Thus, comparing the results from alkane chains nanocrystal embedded in an amorphous phase with isolated crystal, we observed that melting temperature increases and surface tension decreases. This can be clarified by MSD behaviour of one particle near the crystal surface in both systems. Interactions between unbonded monomers in crystal and alkane chains in the amorphous phase decrease the chains mobility in the crystal following higher melting temperature and lower surface tension. Surface tension was obtained to be 37 ± 5 dyne/cm, which is in good agreement with the experimental value of 30.79 dyne/cm for low density polyethylene.

Ultimately, the investigation of the melting and crystallization behavior of polymers under high pressure has interest for the understanding of the polymer structure. Therefore, we calculated the value of surface tension at different pressures (0, 1000, 1500 and 2000 atm) to explore the effect of this parameter on melting temperature and surface tension of this material. Increase of pressure results in decrease of surface tension, which can be described by depression in Gibbs free energy. In addition, decrease in total entropy of fusion of a system under pressure leads to increase of melting point. This fact is associated with crystal configuration. At low pressure, the main part of the orthorhombic lattice goes to a less dense packing even at high pressures. These results are confirmed by experimental data in high pressure as well.

In the experimental part of this project, LDPE (low density polyethylene) was compression molded under different conditions. The effect of mold temperature, mold pressure, cooling rate and temperature profile on the thermal and mechanical properties of the samples were investigated. Higher melting temperature, flexural and tensile modulus were observed from an increase in the molding pressure and molding temperature, while decreasing the cooling rate for symmetric samples (uniform molding temperature). These trends are in agreement with the behavior of the degree of crystallinity and WAXD diffraction pattern. For asymmetric samples where temperature gradient was applied while molding, it was observed that the highest tensile and flexural moduli were obtained for the lowest temperature on both plates. This behavior can be clearly clarified using the flexural modulus ratio when the load was applied on the bottom or the upper sides (E_b/E_u). Finally, surface tension of the samples made at several pressures was measured by a tensiometer. Increasing the molding pressure (pressure induced crystallization) and decrease of molar volume resulted in lower surface tension which can be explained by a sharper depression of the Gibbs free energy during crystallization.

In conclusion, it is a preliminary work on one grade of LDPE to validate the experimental approach and the methodology. Focusing on the relationships between MW, MWD, branching or molecular architecture etc… on compression molding and properties using a reliable experimental approach, is recommended for future work.

Furthermore, simulation of semi-crystalline polymers is a very challenging task. Other simulation methods such as coarse-grained (CG) and united-atom (UA) models can be combined with MD methods to make reasonable resolution on an atomic length scale to simulate these polymers. MC (Monte Carlo) simulations on a lattice is recommended in order to obtain other mechanical properties of semi-crystalline polymers and compare with experiments as well.

APPENDIX I

The pcff force field has been used in this study. The potential energy is the sum of bond stretching, angle bending, torsional rotation, cross terms (describing the coupling between stretching, bending, and torsion energies), electrostatic and van der Waals interactions:

$$V = \sum_b [K_2 (b - b_0)^2 + K_3 (b - b_0)^3 + K_4 (b - b_0)^4] + \sum_\theta [H_2 (\theta - \theta_0)^2 + H_3 (\theta - \theta_0)^3 + H_4 (\theta - \theta_0)^4]$$
$$+ \sum_\varphi [V_1 [1 - \cos(\varphi - \varphi_1^0)] + V_2 [1 - \cos(2\varphi - \varphi_2^0)] + V_3 [1 - \cos(3\varphi - \varphi_2^0)]$$
$$+ \sum_b \sum_b F_{bb'} (b - b_0)(b' - b_0') + \sum_\theta \sum_{\theta'} F_{\theta\theta'} (\theta - \theta_0)(\theta' - \theta_0') + \sum_b \sum_\theta F_{b\theta} (b - b_0)(\theta - \theta_0)$$
$$+ \sum_b \sum_\varphi (b - b_0)[V_1' \cos\varphi + V_2' \cos 2\varphi + V_3' \cos 3\varphi] + \sum_{b'} \sum_\varphi (b - b_0)[V_1'' \cos\varphi + V_2'' \cos 2\varphi + V_3'' \cos 3\varphi]$$
$$+ \sum_\theta \sum_\varphi (\theta - \theta_0)[V_1''' \cos\varphi + V_2''' \cos 2\varphi + V_3''' \cos 3\varphi] + \sum_\varphi \sum_\theta \sum_{\theta'} K_{\varphi\theta\theta'} \cos(\theta - \theta_0)(\varphi' - \varphi_0')$$
$$+ \sum_{i>j} \frac{q_i q_j}{\varepsilon r_{ij}} + \sum_{i<j} \varepsilon r_{ij} \left[2\left(\frac{r_{ij}^*}{r_{ij}}\right)^9 - 3\left(\frac{r_{ij}^*}{r_{ij}}\right)^6\right]$$

K2, K3, K4, H2, H3, H4, V1, V2, V3, V'1,V'2, V'3, V"1, V"2, V"3, V'"1,V'"2, V'"3, b0, θ', φ'1; φ'2, φ'3, εij, r*ij, qi, qj, are potential parameters included into the force field. b, θ, φ, r_{ij}, are bond length, valence angle, dihedral angle, and non-bonding distance between two atoms i and j, respectively.

Table 14. Parameters for non-bonding energetic term

$$E_{\text{non-bonding}} = \sum_{i<j} \varepsilon r_{ij} \left[2\left(\frac{r_{ij}^*}{r_{ij}}\right)^9 - 3\left(\frac{r_{ij}^*}{r_{ij}}\right)^6\right]$$

With $r_{ij}^* = [(r_i^6 + r_j^6)/2]^{1/6}$ and $\varepsilon_{ij} = 2\sqrt{\varepsilon_i * \varepsilon_j} * \frac{r_i^3 * r_j^3}{[r_i^6 + r_j^6]}$

Atom	σ_i (Å)	E (kcal.mol^{-1})
C	4.0100	0.05400
H	2.9950	0.02000

Table 15. Partial charge for nonbonding energetic term

$E_{\text{Electrostatic}} = \sum_{i>j} \frac{q_i q_j}{\varepsilon r_{ij}}$

Atom		q_{ij}	q_{ji}
C	C	0.0000	0.0000
C	H	- 0.0530	0.0530

Table 16. Parameters for bonding energetic term

$E_{\text{bond}} = \sum_b [K_2 (b - b_0)^2 + K_3 (b - b_0)^3 + K_4 (b - b_0)^4]$

Atom		b0	K_2 (kcal mol^{-1} Å^{-2})	K_3 (kcal mol^{-1} Å^{-3})	K_4 (kcal mol^{-1} Å^{-4})
C	C	1.5300	299.6700	-501.7700	679.8100
C	H	1.1010	345.0000	-691.8900	844.6000

Table 17. Parameters for valence energetic term

$E_{\text{Angle bending}} = \sum_\theta [H_2(\theta - \theta_0)^2 + H_3(\theta - \theta_0)^3 + H_4(\theta - \theta_0)^4]$

Atom			θ_0(deg)	H_2 (kcalmol^{-1} deg^{-2})	H_3 (kcalmol^{-1} deg^{-2})	H_4 (kcalmol^{-1} deg^{-2})
C	C	C	112.6700	39.5160	-7.4430	-9.5583
C	C	H	110.7700	41.4530	-10.6040	0.0000
H	C	H	107.6600	39.6410	-12.9210	-2.4318

Table 18. Parameters for dihedral angle energetic term

$E_{\text{Torsional rotation}} = \sum_{\varphi}[V_1[1 - \cos(\varphi - \varphi_1^0)] + V_2[1 - \cos(2\varphi - \varphi_2^0) + V_3[1 - \cos(3\varphi - \varphi_2^0)$

				V_1 (kcal.mol^{-1})	φ_1^0(deg)	V_2 (kcal.mol^{-1})	φ_2^0(deg)	V_3 (kcal.mol^{-1})	φ_3^0(deg)
C	C	C	C	0.0000	0.0	0.0514	0.0	-0.1430	0.0
C	C	C	H	0.0000	0.0	0.0316	0.0	-0.1681	0.0
H	C	C	H	-0.1432	0.0	0.0617	0.0	-0.1083	0.0

Table 19. Parameters for cross terms (bond-bond, bond-angle)

$E_{\text{bond-bond}} = \sum_b \sum_b F_{bb'} (b - b_0)(b' - b_0')$, $E_{\text{bond-angle}} = \sum_b \sum_\theta F_{b\theta} (b - b_0)(\theta - \theta_0)$

Atom			$F_{bb'}$(kcalmol^{-1} Å^{-2})	$F_{b\theta}$ (kcalmol^{-1} Å^{-1}deg^{-1})
C	C	C	0.0000	8.0160
C	C	H	3.3872	20.7540
H	C	H	5.3316	18.1030

Table 20. Parameters for cross terms (angle-angle)

$E_{\text{angle-angle}} = \sum_\theta \sum_{\theta'} F_{\theta\theta'}(\theta - \theta_0)(\theta' - \theta_0')$

Atom				$F_{\theta\theta'}$(kcalmol^{-1}deg^{-2})
C	C	C	C	-0.1729
C	C	C	H	-1.3199
H	C	C	H	-0.4825

Table 21. Parameters for cross terms (End_bond-torsion, middle_bond-torsion); (kcalmol^{-1}Å^{-1})

$E_{\text{end\_bond-torsion}} = \sum_b \sum_\varphi (b - b_0)[V_1' \cos\varphi + V_2' \cos 2\varphi + V_3' \cos 3\varphi]$

$E_{\text{middle\_bond-torsion}} = \sum_{b'} \sum_\varphi (b - b_0)[V_1'' \cos\varphi + V_2'' \cos 2\varphi + V_3'' \cos 3\varphi]$

				Left	(kcalmol^{-1} Å^{-1})		Right			(kcalmol^{-1} Å^{-1})		
I	J	K	L	V_1'	V_2'	V_3'	V_1'	V_2'	V_3'	V_1''	V_2''	V_3''
C	C	C	C	-0.0732						-17.7870	-7.1877	0.0000
C	C	C	H	0.2486	0.2422	-0.0925	0.0814	0.0591	0.2219			
H	C	C	H	0.2130	0.3120	0.0777				-14.2610	-0.5322	-0.4864

Table 22. Parameters for cross terms (angle-angle, Angle-angle-torsion); (kcalmol^{-1}deg^{-1})

$E_{\text{angle-torsion}} = \sum_\theta \sum_\varphi (\theta - \theta_0)\,[V_1''' \cos\varphi + V_2''' \cos 2\varphi + V_3''' \cos 3\varphi]$

$E_{\text{angle-angle-torsion}} = \sum_\varphi \sum_\theta \sum_{\theta'} K_{\varphi\theta\theta'} \cos(\theta - \theta_0)(\varphi' - \varphi_0')$

				left	(kcalmol^{-1}deg^{-1})		Right			
				V_1'''	V_2'''	V_3'''	V_1'''	V_2'''	V_3'''	$K_{\varphi\theta\theta'}$(kcalmol^{-1}deg^{-2})
C	C	C	C	0.3886	-0.3139	0.1389				-22.0450
C	C	C	H	-0.2454	0.0000	-0.1136	0.3113	0.4516	-0.1988	-16.1640
H	C	C	H	-0.8085	0.5569	-0.2466				-12.5640

Bibliography

1. N. Metatla, S. Palato, B. Commarieu, J.P. Claverie, A. Soldera. Soft Matter. 8 , 347-35 (**2012**).

2. S. T. Milner. Soft Matter. 7, 2909-2917 (**2011**).

3. A. Steinchen. Colloids Surf. A. 323, 163–166 (**2008**).

4. J.M. Salazar, O. Politano, S. Garruchet, A. Sanfeld and A. Steinchen. Philos. Mag. 84, 3397–3409 (**2004**).

5. C. N. R. Rao, P. J. Thomas and G. U. Kulkarni. Nanocrystals: Synthesis, Properties and Applications, Springer, Berlin Heidelberg, 1st edn (**2007**).

6. M.J. Chaudhury. Materials Science and Engineering. 97, 159 (**1996**).

7. L. Li, S. Hong, R. Huang.. J. Phys.: Condens. Matter. 14, 11195 (**2002**).

8. H. Park, R.B. Thompson, N. Lanson, C. Tzoganakis, C.B. Park, P. Chen. J. Phys. Chem. B. 111, 3859-3868 (**2007)**.

9. G. Gompper, M. Schick, Wiley-VCH: Weinheim. 1, 87-178 (**2005**).

10. M.W. Matsen. J. Phys.: Condens. Matter. 14, R21-R47 (**2002**).

11. G.H. Fredrickson, V. Ganesan, F. Drolet. Macromolecules. 35, 16-39 (**2002**).

12. F. Schmid. J. Phys.: Condens. Matter. 10, 8105-8138 (**1998**).

13. L. Fontana, D.Q. Vinh, M. Santoro, S. Scandolo, F.A. Gorelli, R. Bini, M. Hanfland. Phys. Rev. B. 75, 174112 (**2007**).

14. V.F. Puntes, K.M. Krishnan and A.P. Alivisatos. Science. 291, 2115–2117 (**2001**).

15. C.Y. Chiu, Y. Li, L. Ruan, X. Ye, C.B. Murray and Y. Huang. Nat. Chem. 3, 393–399 (**2011**).

16. K. Baba, H. Kasai, K. Nishida and H. Nakanishi, in Nanocrsytals, ed. Y. Masuda, InTech, (**2010**).

17. S.Z.D. Cheng. Nature. 448, 1006–1007 (**2007**).

18. Y. Tsuchiya, H. Hasegawa and T. Iwatsubo. J. Chem. Phys. 114, 2484–2488 (**2001**).

19. N.A. Romanos and D.N. Theodorou. Macromolecules. 43, 5455–5469 (**2010**).

20. V.A. Kriuchkov, J.C. Daigle, K.M. Skupov, J.P. Claverie and F.M. Winnik. J. Am. Chem. Soc. 132, 15573–15579 (**2010**).

21. G.C. Schatz, PNAS. 17, 6885–6892 (**2007**).

22. D.M. Sadler, Nature. 326, 174 (**1987**).

23. L. Toma, S. Toma, and J. A. Subriana. Macromolecules.31, 2328 (**1998**).

24. C. Liu and M. Muthukumar, J. Chem. Phys. 109, 2536 (**1998**).

25. T. Yamamoto, M. Hikosaka, and N. Takahashi. Macromolecules. 27, 1466 (**1994**).

26. T. Yamamoto. J. Chem. Phys.107, 2653 (**1997**).

27. H. Takeuchi. J. Chem. Phys. 109, 5614 (**1998**).

28. X.Guo, A.I. Isayev, L. Guo. Polym. Eng. Sci. 39, 2096-2114 (**1999**).

29. J. A. Parker, D.C. Bassett, R.H. Olley, P. Jaaskelainen. *Polymer* 35, 4140-4145 (**1994**).

30. J. Lu, F. Gao. Ind. Eng. Chem. Res. 47, 1967-1974 (**2008**).

31. L. Capt, The Pressure-Volume-Temperature behavior and the effect of pressure on crystallization kinetics of polyethylene resins. McGill University (**1999**).

32. D.M. Lincoln, R.A. Vaia, Z.G. Wang, B.S. Hsiao, R. Krishnamoorti. *Polymer.* 42, 09975-09985 (**2001**).

33. H.Wei, Surface Tension Measurement of High Density Polyethylene and Its Clay. University of Waterloo (**2009**).

34. C.Subramaniam, Morphology, Crystallization and Melting Behaviors of Random Copolymers of Ethylene with 1-Butene, 1-Pentene and 1-Hexene. University of Virgina Tech (**1999**).

35. L.Fontana, D.Q. Vinh, M. Santoro, S. Scandolo, F.A. Gorelli, R. Bini, M. Hanfland. Phys. Rev. B. 75, 174112 (**2007**).

36. D.C. Bassett, B.Turner. Nature (London), Phys. Sci.240, 146 (**1972**).

37. Q.Yuan, R. Gudavalli, R.D.K. Misra. Mater. Sci. Eng. A. 492, 434-442 (**2008**).

38. A. Seeger, D. Freitag, F. Freidel, G. Luft. Thermochim. Acta. 424, 175-181 (**2004**).

39. H.Masamichi, M. Shigeru, S. Tsuneo. J. Appl. Phys.19, 1763 (**1980**).

40. C. Nakafuku. *Polymer.* 15, 641-647 (**1983**).

41. C. Nakafuku. *Polymer.* 22, 1673-1676 (**1981**).

42. M. Hikosaka, S. Rastogi, A. Keller, H. Kawabata, Journal of macromolecule science,part B. Physics.31,87-131 (**1992**).

43. H. Nathani, A. Dasari, R.D.K. Misra. Acta Mater.54, 3217–3227 (**2004**).

44. J.A. Sauer. Polym. Eng. Sci.17, 150-164 (**1997**).

45. P,B. Bowden, J.A. Jukes. J. Mater. Sci. 7, 52-63 (**1972**).

46. I.M. Ward. J. Mater. Sci. 6, 1397-1417 (**1971**).

47. S.B. Ainbinder, M.G. Laka, I.Y. Maiors. Polym. Mech.1, 50-55 (**1965**).

48. J. sugi, H. Kimihiko,N. Hirai, H. Junichi. Proc. Int. Conf. High Pressure, 4th. 34, 59-64 (**1964**).

49. B. Kieback, A. Neubrand, H. Riedel. Mater. Sci. Eng., A.362, 81-106 (**2003**).

50. S. Koide, N. Asakawa, Y. Inoue, K. Yazawa. Macromol. Chem. Phys. 209, 499-507 (**2008**).

51. C. Tovar-Cisneros, R. González-Núñez, D. Rodrigue. J. Cell. Plast. 44, 223-237 (**2008**).

52. A. Peacoc. Handbook of Polyethylene: Structures: Properties, and Applications, Marcel Dekker Inc., Newyork (**2000**).

53. H. weiguo, Dynamics and structure of semicrystalline polymers as characterized by NMR, and their relationship to macroscopic properties. University of Massachusetts Amherst(**2014**).

54. B. Viswanathan, Catalysis: Principles and Applications, Narosa publishing house, New Delhi(**2002**).

55. O. Gerngross, K. Herrmann, W. Abitz. Biochem. Z. 228, 409-425 (**1930**).

56. A. Peterlin, Crystalline character in polymers, Journal of Polymer Science: Polymer Symposia .9,61-89 (**1965**).

57. A. Keller. Philosophical Magazine. 2, 1171-1175 (**1972**).

58. A. Keller. Rep. Prog. Phys. 31, 623 (**1998**).

59. D.T. J. Hurle ,Bulk Crystal Growth: Part B. Bulk Crystal Growth, North-Holand, Amsterdam (**1994**).

60. F. Khoury , E. Passaglia, Treatise on Solid State Chemistry, Plenum Press, NewYork, 3, 335-496 (**1976**).

61. K. Storks. JACS. 60, 1753-1761 (**1936**).

62. B.S. Hsiao, R.S. Stein, K. Deutscher, H.H. Winter. J. Polym. Sci., Part B: Polym. Phys.28, 1571-1588 (**1990**).

63. M. Herbst. Z ELEKTROCHEM . 54, 318-320 (**1950**).

64. P.J. Flory, J. Chem. Phys.17, 3, 223 (**1949**).

65. R. Chiang and P.J. Flory, J. Am. Chem. Soc.83, 2857 (**1961**).

66. J.I. Lauritzen Jr, J.D. Hoffman, J. Res. Natl. Bur. Std. 64A, 73 (**1960**).

67. J.I. Lauritzen Jr., J.D. Hoffman, J. Appl. Phys. 44, 4340 (**1973**).

68. J.I. Lauritzen Jr., J. Appl. Phys. 44, 4353 (**1973**).

69. J.D. Hoffman, Polymer. 24, 3 (**1983**).

70. J.D. Hoffman, R.L. Miller, H. Marand, D.B. Roitman, Macromolecules.25, 2221 (**1992**).

71. J.H. Gibbs, Collected Works, Longman Green & Company, Essex, U. K. (**1928**).

72. J.D. Hoffman, Soc. Plast. Eng. Trans. 4, 315 (**1964**).

73. A. Keller, G. Goldbeck-Wood, M. Hikosaka. Faraday Discuss.95, 109-128 (**1993**).

74. B. Heck, S. Siegenführ, G. Strobl, R. Thomann. Polym.48, 1352-1359 (**2007**).

75. G.Strobl, Eur. Phys. J. E. 3, 165–183 (**2000**).

76. Y.Takashio.Polymer.50,1975-1985 (**2009**).

77. W.Hu, D. Frenkel . Adv Polym Sci.191,1 (**2005**).

78. M. Muthukumar. Adv Polym Sci.191,241 (**2005**).

79. T.Yamamoto. Adv Polym Sci.191,37 (**2005**).

80. J.U. Sommer , C. Luo. Journal of Polymer Science Part B: Polymer Physics. 48, 21 (**2010**)

81. L. Brandon, K. Peters, M. Salerno, A. Agrawal, D. Perahia, G.S. Grest.J. Chem. Theory Comput. 13, 2890–2896 (**2017**).

82. B. Pallavi Banerjee , S. Roy, N. Nair. J. Phys. Chem. B.122, 1516–1524 (**2018**).

83. D. Reith, H. Meyer, F. Müller-Plathe. Macromolecules.34, 2335–2345 (**2001**).

84. G. Jaeger. Arch. Hist. Exact Sci. 53, 51-81 (**1998**).

85. D. Young. Computational Chemistry: A Practical Guide for Applying Techniques to Real world problems, John Wiley & Sons, Inc(**2001**).

86. P. Ahlrichs, B. Dünweg. J. Mod. Phys. 9, 1429 (**1998**).

87. V.T. Le, C. Epa, F.R. Burden, D. A. Winkler, Chem. Rev.112, 2889–2919 (**2012**).

88. P.J. Flory, M. Volkenstein, Biopolymers.8,5 (**1969**).

89. M.P. Allen.Introduction to Molecular Dynamics Simulation, John von Neumann Institute for Computing(**2004**).

90. F. Jensen. Introduction to Computational Chemistry, John Wiley & Sons Ltd (**2007**).

91. G.C. Maitland, M. Rigby, E.B. Smith, W.A. Wakeham. Intermolecular forces: their origin and determination, Clarendon Press, Oxford (**1981**).

92. C.G. Gray and K.E. Gubbins. Theory of molecular _uids. 1. Fundamentals,Clarendon Press, Oxford (**1984**).

93. M. Sprik. Effective pair potentials and beyond,Dordrecht, Kluwer Academic Publishers (**1993**).

94. A.J. Stone. The Theory of Intermolecular Forces. Clarendon Press, Oxford (**1996**).

95. A. Rahman. Phys. Rev. A.136,405-411 (**1964**).

96. L. Verlet. Phys. Rev. 159,98-103 (**1967**).

97. S.L. Price. Rev. Comput. Chem. 14,225-289 (**2000**).

98. N.L. Allinger, Y.H. Yuh, and J.H. Lii. J. Am. Chem. Soc. 111,8551-8566 (**1989**).

99. J.H. Lii, N.L. Allinger. J. Am. Chem. Soc.111,8566-8575 (**1989**).

100. J.H. Lii ,N.L. Allinger. J. Am. Chem. Soc. 111,8576-8582 (**1989**).

101. N.L. Allinger, K.S. Chen, and J.H. Lii. J. Comput. Chem.17,642-668 (**1996**).

102. N. Nevins, K.S. Chen, N.L. Allinger. J. Comput. Chem.17,669-694 (**1996**).

103. N. Nevins, J.H. Lii, and N.L. Allinger. J. Comput. Chem.17,695-729 (**1996**).

104. S. J.Weiner, P. A. Kollman, D. A. Case, U.C. Singh, C. Ghio, G. Alagona, S. Profeta, P.Weiner. J. Am. Chem. Soc. 106,765-784 (**1984**).

105. W.D. Cornell, P. Cieplak, C.I. Bayly, I.R. Gould, K.M. Merz, D.M. Ferguson, D.C. Spellmeyer, T. Fox, J.W. Caldwell, and P.A. Kollman.. J. Am. Chem. Soc. 117,5179-5197 (**1995**).

106. B.R. Brooks, R.E. Bruccoleri, B.D. Olafson, D.J. States, S. Swaminathan, M. Karplus. J. Comput. Chem.4,187-217 (**1983**).

107. W.L. Jorgensen, D.S. Maxwell, J. TiradoRives . J. Am. Chem. Soc. 118,11225-11236 (**1996**).

108. E. Hairer, C. Lubich, and G.Wanner. Acta Numerica.12,399-450 (**2003**).

109. C.J. Cotter and S. Reich. Computational Nanotechnology. American Scienti_c Publishers, Newyork (**2004**).

110. B. Leimkuhler , S. Reich. Geometric Numerical methods for Hamiltonian Mechanics.Cambridge University Press, Cambridge (**2004**).

111. L. Verlet. Phys. Rev.165,201-214 (**1968**).

112. R.W. Hockney , J.W. Eastwood. Computer simulations using particles, Adam Hilger, Bristol (**1988**).

113. W.C. Swope, H.C. Andersen, P.H. Berens, K.R.Wilson. J. Chem. Phys. 76,637-649 (**1982**).

114. D. Beeman, J. Comput. Phys. 20, 130 (**1976**).

115. M.P. Allen, D.J. Tildesley. Computer simulation of liquids, Oxford university press (**1989**).

116. D. Beglov, B. Roux. J. Chem. Phys.100, 9050-9063 (**1994**).

117. A. Juffer, H. Berendsen. Mol. Phys. 79, 623-644 (**1993**).

118. G. King, A. Warshel. J. Chem. Phys. 91, 3647-3661 (**1989**).

119. G. Petraglio, M. Ceccarelli, M. Parrinello. J. Chem. Phys. 123, 44-103 (**2005**).

120. P.P. Ewald. Ann. Phys. 64, 253-287 (**1921**).

121. T.R. Gingrich, M. Wilson. Chem. Phys. Lett.500, 178-183 (**2010**).

122. L. Verlet. Phys. Rev. 159, 98 (**1967**).

123. H.C. Andersen. J. Chem. Phys. 72,2384-2393 (**1980**).

124. S. Nos´e.Molec. Phys. 52,255-268 (**1984**).

125. W.G. Hoover. Phys. Rev. A. 31,1695-1697 (**1985**).

126. G.J. Martyna, M.L. Klein, and M. Tuckerman. J. Chem. Phys.97,2635-2643 (**1992**).

127. M. Parrinello, A. Rahman. J. Appl. Phys. 52, 7182-7190 (**1981**).

128. W.G. Hoover. Phys. Rev. A .31, 1695 (**1985**).

129. S. Nosé. J. Chem. Phys.81, 511-519 (**1984**).

130. R.H. Byrd, P. Lu, J. Nocedal. J. Scientif. Statistic. Comput.16,1190–1208 (**1995**).

131. S. Pronk, S. Pall, R. Schulz , P. Larsson , P. Bjelkmar , R. Apostolov . Bioinf. 29,845–54 (**2013**).

132. S. Miyamoto, P.A. Kollman, .J. Comp. Chem.13,952–962 (**1992**).

133. C. Zhu, R.H. Byrd, J. Nocedal .ACM Trans. Math. Softw.23,550– 560 (**1997**).

134. D.N. Theodorou, U.W. Suter. Macromolecules.18, 1467-1478 (**1985**).

135. P. Flory, M. Volkenstein. Wiley Online Library (**1969**).

136. H. Meirovitch. Phys. Rev. A. 32, 3709 (**1985**).

137. R. Caminiti, L. Pandolfi , P. Ballinaro. Science, Part B: Physics. 39, 481-492 (**2000**).

138. H.M. Rietveld, J. Appl. Cryst. 2, 65 (**1969**).

139. S. Plimpton, J. Comput. Phys.117, 1 (**1995**).

140. H. Sun, S.J. Mumby, J.R. Maple , A. T. Hagler, J. Phys. Chem. 99, 5873 (**1995**).

141. G. Yuan, Z. Wei, G. Li, Journal of Computational and Applied Mathematics. 4,32 (**2013**).

142. R. Burden, J.D. Faires. Prindle, Weber and Schmidt, Boston (**1981**).

143. L.A. Utracki, Polymer composit. 8, 6 (**1987**).

144. D.Yao, Effects of processing techniques on mechanical properties of selected polymers. M.Sc. Thesis University of North Texas (**2013**).

145. A.R. Agrawal, I.O. Pandelidis , M. Pecht, Polymer engineering and science. 27,18 (**1987**).

146. D.V. Rosato, Marlene G. Rosato ,Injection Molding Handbook, Springer Science+Bussiness Media, Newyork (**2000**).

147. T. Robert, D.K. Allen, L. Alting. Manufacturing Processes Reference Guide. New York: Industrial P, Incorporated, Newyork (**1993**).

148. R. Creese, Introduction to Manufacturing Processes and Materials, Taylor and Francis Group(**1999**).

149. A.K. Bhowmick,Material science and engineering. 5, 23 (**1998**).

150. A.A. Askadski, Physical Properties of Polymers Prediction and Control, G & B publishers, Moskow (**1996**).

151. O.E. Robert. polymer science and technology, CRC Press, USA (**2000**).

152. L.H. Sperling. Introduction to physical polymer science, John Wiley & Sons, Inc. USA, 4th Ed.(**1932**).

153. K. Balani ,V. Verma ,A. Agarwal, R. Narayan.Physical, Thermal, and Mechanical Properties of Polymers, John Wiley & Sons, Inc. USA (**2015**).

154. J.E. Mark, Physical Properties of Polymers Handbook, , Springer, New York (**2007**).

155. H. Zhu, Y.Wang, X. Zhang, Y. Su, X. Dong, Q. Chen, Y. Zhao, C. Geng, S. Zhu, C.C. Han, D.Wang. Polymer. 48, 5098-5106 (**2007**).

156. Wu, N., Dai, J., Micale, F.J., Dynamic Surface Tension Measurement with a Dynamic Wilhelmy Plate Technique. J. Colloid Interface Sci. 215, 258-269 (**1999**).

157. S.B. ainbinder, M.G. Laka and I.Yu. Maiors.Meckanica Polymer. 1, 65 (**1965**).

158. W.Whiteny , R.D. Andrews, J.Polymer Sci. C16, 2981 (**1967**).

159. P.B. Bowden and J.A. Jukes, J. Mater.Sci. 3, 183 (**1968**).

160. K.D. Pae, D.R. Meras, J.A . Sauer, Polymer Lett. 6,773 (**1986**).

161. G. Biglion, E. Baer and S.V. Radcliffe, Paper presented on at Brighton conference on Fracture(**1969**).

162. K.D. Pae, D.R. Mears, J. Polymer Sci. B6,269 (**1986**).

163. L. Holiday, J. Mann, G. Pogany, H.D. Puge and D.A. Green , Nature. 202,381 (**1964**).

164. S. Rabinowitz, I. M.Ward, Journal of Materials Science. 5, 29-39 (**1970**).

165. A. Shamloo, B. Fathi, S. Elkoun, D. Rodrigue, A. Soldera. Journal of Applied Polymer Science.135,46176 (**2017**)

166. G. Upper, W. Zhang, D.Beckel, S. Sohn, K. Liu, E. Kiran, Ind. Eng. Chem. Res. 45, 1478–1492 (**2006**)

167. E. Weidner, J. Knez, Z. Novak, European Patent EP 0744 992, WO 95/21688 (**1995**).

168. R. Droegemeier, C. Meister, A. Schottstedt, E. Schweers, U. Bauer, H. Mueller, O. Mientkewitz, WO 03/027170, DE 101 45 663.8 (**2003**).

169. H. Käufer, Arbeiten mit Kunststoffen, Springer-Verlag, Berlin (**1981**).

170. B.Wunderlich, L. Melillo, Makromol Chem.118,250 (**1968**).

171. S. Basset, S. Block, G.J. Piermarini, J.Appl Phys. 45,4146 (**1974**).

172. M.Hikosaka, S. Rastogi, A. Keller, H. Kawabata. J. Macromol. Sci.Phys. B31,87 (**1992**).

173. S.Rastogi, M.Hikosaka, H. Kavabata. J.Makromol Chem , Makromol. Symp. 48, 103 (**1991**).

174. D.C.Basset, B. Turner. Philos. Mag. 29,925 (**1974**).

175. K.Takamizawa, A. Ohno, Y. Urabe. Polyme.J.7,342 (**1975**).

176. M.Yasuniva, R. Enoshita,T. Takemura, Jpn. J. Appl. Phycs .15,1421 (**1976**).

177. M. Hikosaka, S. Minomura, T. Seto . Jpn. J. Appl. Phycs. 19, 1763 (**1980**).

178. C. Nakafuka, T. Miyaki, Polymer. 24,141 (**1983**).

179. S. Saeki, S. Takei, Y. Ooukubo. Polymer. 39,18 (**1998**).

180. J.S. Cousineau, Effect of cooling rate and mold counter pressure on the crystallinity and foaming control in microcellular injection molded polypropylene parts. M.Sc. Thesis, Wright State University (**2012**).

181. W. Kunze, H. Möhler. Thermochim. Acta. 83, 47-58 (**1985**).

182. M. Yoshioka, B. Hancocks, G. Zograf, Journal of Pharmaceutical Sciences. 83, 12 (**1994**).

183. C. Leyva-Porras, M.A. Esneider-Alcala, A. Toxqui-Teran Marquez-Lucero, J.A. Aguilar-Martinez. Ind. Eng. Chem. Res. 52, 5666−5671 (**2013**).

184. G. Reiter, G. Strobl.Progress in Understanding Polymer *Crystallization*, Springer:,New York (**2007**).

185. H. Wei, R.B. Thompson, C.B. Park, P. Chen. Colloids Surf., A. 354, 347-352 (**2010**).

186. V. Brucato, S. Piccarolo, V. La Carrubba. Chem. Eng. Sci. 57, 4129-4143 (**2002**).

187. S. Avlar, Y. Qiao. Composites, Part A. 36, 624-630 (**2005**).

188. D. Cavallo, L. Gardella, G.C. Alfonso, G. Portale, L. Balzano, R. Androsch. Colloid Polym. Sci. 289, 1073-1079 (**2011**).

189. M.Yuan, L.S. Turng. *Polymer.* 46, 7273-7292 (**2005**).

190. W.T.J. Winter. Chem. Educ. 58*,* A378 (**1981**).

191. Y.l. Hiseh, Z.S. Mo.J.Appl. Polym. Sci. 33,1479 (**1987**).

192. S.Wu. Polymer Interface and Adhesion. Marcel Dekker Inc, New York (**1982**).

193. J.Yao, D. Rodrigue, .Cell. Polym.31, 189-206 (**2012**).

194. M.R. Barzegari, Y. Jialolian,D. Rodrigue.Cell. Polym. 28, 237-237 (**2009**).

195. L.Li, S. Hong, R. Huang. J. Phys.: Condens. Matter. 14, 11195 (**2002**).

196. J.S.Colton, N.P. Suh. Polym. Eng. Sci.27, 500-503 (**1987**).

197. X.D. Feng,Y.F. Ma. Adv Mat Res. 399,113-116 (**2010**).

198. V.P. Juskey, C.E. Chaffey, Canadian J.Chem.Enq. 334 , 78 (**1982**).

199. M.S. Boaira, C.E. Chaffey. Polym.Enq.Sci.17, 715 (**1977**) .

200. K.Okuno, R.T. Woodhams. Polym.Eng.Sci.15, 308 (**1975**).

201. B.M.Badran, A. Galeski, M. Kryszewski. J.Appl.Polym.Sci.21,3669 (**1982**).

202. J.He. AIP Adv. 5, 117206 (**2015**).

203. Y. Wang, M. Rafailovich, J. Sokolov, D. Gersappe, T. Araki, Y. Zou, A. D. L. Kilcoyne, H. Ade, G. Marom and A. Lustiger, Phys. Rev. Lett.96, 028303 (**2006**).

204. G.W.H. Höhne. Polymer. 43, 4689-4698 (**2002**).

205. P. Welch, M. Muthukumar. Physical Review Letters. 87, 218302 (**2001**).

206. Y. Wang, M. Rafailovich, J. Sokolov, D. Gersappe,T. Araki, Y. Zou, A.D.L. Kilcoyne, H. Ade, G. Marom, A.Lustiger. Physical Review Letters. 96, 028303 (**2006**).

207. F. Daan, S.B., Understanding molecular simulation: From algorithms to applications. 2nd ed.; Academic Press (**2001**).

208. C. Chakravarty,P.G. Debenedetti, F.H. Stillinger. The Journal of Chemical Physics. 126 , 204508 (**2007**).

209. B. Bagchi. Molecular Relaxation in Liquids Oxford University Press: New York (**2012**).

210. C. Alba-Simionesco, B. Coasne, G. Dosseh, G. Dudziak,K.E. Gubbins,R. Radhakrishnan, M. Sliwinska-Bartkowiak. Journal of Physics: Condensed Matter. 18, R15 (**2006**).

211. C.K. Das , J.K. S. Theor. Chem Acc. 132, 1351 (**2013**).

212. E.A. Zubova, N.K. Balabaev, L.I.Manevitch. Polymer. 48, 1802-1813 (**2007**).

213. T.Yamamoto. The Journal of Chemical Physics. 107, 2653-2663 (**1997**).

214. E.Yu. Tonkov, E. G. P. Phase Transformations of Elements Under High Pressure. CRC Press. Boca Raton, London New York Washington, D.C. (**2005**).

215. F.A. Quinn, L. Mandelkern. Thermodynamics of Crystallization in High Polymers: Poly-(ethylene)1. Journal of the American Chemical Society. 80, 3178-3182 (**1958**).

216. R.E. Robertson. Macromolecules.2, 4 (**1969**).

217. H.W. Starkweather. Polymer Engineering & Science. 5, 5-6 (**1965**).

218. X.D. Fa, Y.F. Ma. Advanced Materials Research. 113, 3 (**2010**).

219. A. Soldera and N. Metatla, Composites, Part A. 36, 521–530 (**2005**).

220. H.J.C. Berendsen, J.P.M. Postma, W.F. van Gunsteren, A. DiNola and J.R. Haak, J. Chem. Phys. 81, 3684 (**1984**).

221. H. Li, L.J. Lee, D.L. Tomasko, Ind. Eng. Chem. Res. 43, 509-514 (**2004**).